Petrography and geochemistry of hydrothermal breccias hosted in the Schrikkloof Formation (Rooiberg Group), north of Modimolle, South Africa

UNIVERSITEIT VAN PRETORIA
UNIVERSITY OF PRETORIA
YUNIBESITHI YA PRETORIA
Denkleiers • Leading Minds • Dikgopolo tša Dihlalefi

Submitted by: **Mr Luzuko Chiya**

Student number: 27387072

Supervisor: Prof. Nils Lenhardt

Co-supervisor: Prof. Laurence Robb

Submitted as partial requirement for the degree

MSc Geology

in the Faculty of Natural and Agricultural Sciences

University of Pretoria

Date of Final Version: 26 May 2023

Declaration:

I, the undersigned, declare that the **thesis**, which I hereby submit for the degree **MSc** at the University of Pretoria, is my own work and has not previously been submitted by me for a degree at this or any other tertiary institution. I, the undersigned, furthermore declare that:

- I understand what plagiarism is and am aware of the University's policy in this regard.
- I declare that this assignment (e.g. essay, report, project, assignment, dissertation, thesis, etc.) is my own original work. Where other people's work has been used (either from a printed source, Internet or any other source), this has been properly acknowledged and referenced in accordance with Departmental requirements.
- I have not used work previously produced by another student or any other person to hand in as my own.
- I have not allowed, and will not allow, anyone to copy my work with the intention of passing it off as his or her own work.
- I understand the Department of Geology's policy on plagiarism and the criteria set for using Turnitin by the Department.
- I acknowledge that I am allowed to use Turnitin to evaluate my own work prior to submission.

Full names:	Mr Luzuko Chiya
Student number:	27387072
Date submitted:	26 May 2023
Degree:	MSc Geology
Topic of work:	*Petrography and geochemistry of hydrothermal breccias hosted in the Schrikkloof Formation (Rooiberg Group), north of Modimolle, South Africa*
Supervisor(s):	Prof Nils Lenhardt, Department of Geology
Co-supervisor(s):	Prof Laurence Robb, University of the Witwatersrand
Signature:	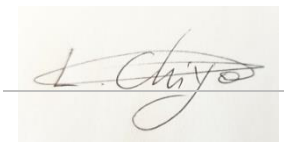

Abstract

The Schrikkloof Formation, composed of rhyolites, tuffs and hydrothermal breccias, is the youngest rhyolitic volcanic sequence of the Rooiberg Group of the Bushveld Igneous Complex and is known to host polymetallic Sn-F-REE. The aim and objective of this research is to understand whether the hydrothermal brecciation in the upper Schrikkloof Formation is associated with ore forming processes or not. The study area is located approximately 20 km north of Modimolle and a total of 30 rock samples (7 rhyolites, 10 tuffs, 12 hydrothermal breccias and 1 vein) was collected from outcrops. These samples were sent for petrography, XRF (major element analysis), ICPMS (trace element analysis), SEM-EDX analysis (ore mineralogy).

Geochemical results (REE diagram and Rb vs Nb+Y) suggest that the Schrikkloof Formation was derived from melting of the continental crust and was emplaced in an intra-cratonic (within-plate) tectonic setting. The sparsely porphyritic and glassy textures of both rhyolites and tuffs, respectively, in the Schrikkloof Formation indicate a subaerial environment.

The hydrothermal breccias are particularly hosted within tuffs rather than in rhyolites, perhaps because of competency contrast. Hand-specimen and petrography observations suggested that both tuffs and rhyolites underwent varying degrees of hematitisation and sericitisation alterations.

In addition, results also indicated that hydrothermal breccias are predominantly characterised by silica-rich (SiO_2 > 70%) clasts cemented by Fe-rich veins (Fe_2O_3 > 80%). The clasts are mainly composed of quartz and K-feldspar, whereas the

cement consists of hematite associated with anglesite ($PbSO_4$) and monazite ($(Ce,Nd,La)PO_4$). The Gresens' and Grant's mass balance approach results suggest that the hematitisation process is associated with the overall gain of Pb-Zn-Ce-Nd-La in hydrothermal breccia and hematitised tuffs. In conclusion, hydrothermal breccias are associated with Pb-Zn mineralisation and this may suggest that there is a concealed Pb deposit.

Keywords

Rooiberg Group; Schrikkloof Formation; hydrothermal breccias; hematitised tuffs; Pb-Zn mineralisation.

Acknowledgements

The Council for Geoscience is acknowledged for funding and providing required resources to complete this project. Thank you to Prof Nils Lenhardt for supervising this thesis. Prof Laurence Robb is acknowledged for co-supervising this thesis. Mr Litshedzani Mutele is acknowledged for constructive discussions, scientific inputs and assisting with field work. Dr Alazar Billay is acknowledged for scientific inputs and support. Thank you to Mr Rames Chauke for constructive discussions. Thank you to Mr Sazi Cele for assisting with field work and sample preparation. Lastly, I would like to thank my late mother, Ms Bulelani Victoria Chiya, for encouraging me to continue with my studies.

Table of contents

List of Figures

List of Tables

List of abbreviations

Abbreviation	Meaning
4A/MS	See ICP-MS
4A/OE	See ICP-OES
Ang	Anglesite
BSE	Backscattered electron
ca.	Circa
CGS	Council for Geoscience
Chl	Chlorite
Fm	Formation
Ga	Giga annum
GPS	Global positioning system
Hem	Hematite
HREE	Heavy rare earth elements
ICP-MS	Inductively coupled plasma mass spectrometry
ICP-OES	Inductively coupled plasma-optical emission spectroscopy
Kfs	K-feldspar
LOI	Loss on ignition
LREE	Light rare earth elements
Ma	Mega annum
Mnz	Monazite
PPL	Plane polarised light
ppm	Parts per million
Qtz	Quartz
REE	Rare earth elements

SEM-EDX	Scanning electron microscopy – energy dispersive X-ray
TML	Thabazimbi-Murchison lineament
XPL	Cross polarised light
XRF	X-ray fluorescence
wt.%	Weight percent

1 Introduction

The Rooiberg Group (dated 2061 ± 2 Ma; Walraven, 1997) is the oldest volcanic sequence of the Bushveld Magmatic Province, a Palaeoproterozoic magmatic suite which includes (from oldest to youngest) the Rustenburg Layered Suite (2055.91 ± 0.26 Ma; Zeh et al., 2015), Rashoop Granophyre Suite (2053 ± 12 Ma; Coertze et al., 1978) and Lebowa Granite Suite (2054 ± 2 Ma; Walraven and Hattingh, 1993). The current preserved outcrop of the Rooiberg Group covers an area of approximately ~65 000 km^2 with an original volume (before erosion) estimated at 300 000 km^3 (Twist and French, 1983).

The Rooiberg Group volcanic sequence is well preserved in the south-eastern portion of the Bushveld Igneous Complex (Figure 1.1) and predominantly occurs in areas underlain by the Rustenburg Layered Suite (Schweitzer et al., 1997; Mathez et al., 2013). This volcanic unit typically has basaltic-andesitic composition at the base and becomes more rhyolitic towards the top; these units are interlayered with siliciclastic and volcaniclastic sediments throughout the stratigraphy (Twist and French, 1983; Schweitzer et al., 1995a; Buchanan, 2006; Lenhardt and Eriksson, 2012). The Rooiberg Group is subdivided into (from oldest to youngest) the Dullstroom, Damwal, Kwaggasnek and Schrikkloof Formations (Figure 1.1; Schweitzer et al., 1995a; Buchanan, 2006).

The Rooiberg Group is known to host polymetallic, exogranitic Sn-F-REE mineralisation, within the Kwaggasnek and Schrikkloof Formations, linked to the intrusion of the Lebowa Granite Suite (Schweitzer et al., 1995b; Crocker et al., 2001). The style of mineralisation includes an exogranitic Fe-F-REE breccia pipe hosted within the upper Schrikkloof Formation ignimbrite at Vergenoeg Mine near Rust de

Winter (Schweitzer et al., 1995b; Crocker et al., 2001). Another style of mineralisation includes exogranitic tin (Sn) in stratabound irregular chloritised veins hosted in ignimbrites (Union Tin Member) of the upper Kwaggasnek Formation, approximately 20 km west of Mookgophong (Schweitzer et al., 1995b; Crocker et al., 2001). Within the Schrikkloof Formation, north of Modimolle, there has been no recorded economic or sub-economic mineral deposits associated with hydrothermal brecciation.

1.1 Aims and objectives

The aims and objectives of this thesis are:

- To understand whether the hydrothermal brecciation process in the upper Schrikkloof Formation of the Modimolle area is a potential ore forming process or not. The study area is located approximately 20 km north of Modimolle (Figure 1.1).
- To better understand the geochemical processes associated with these hydrothermal breccias.

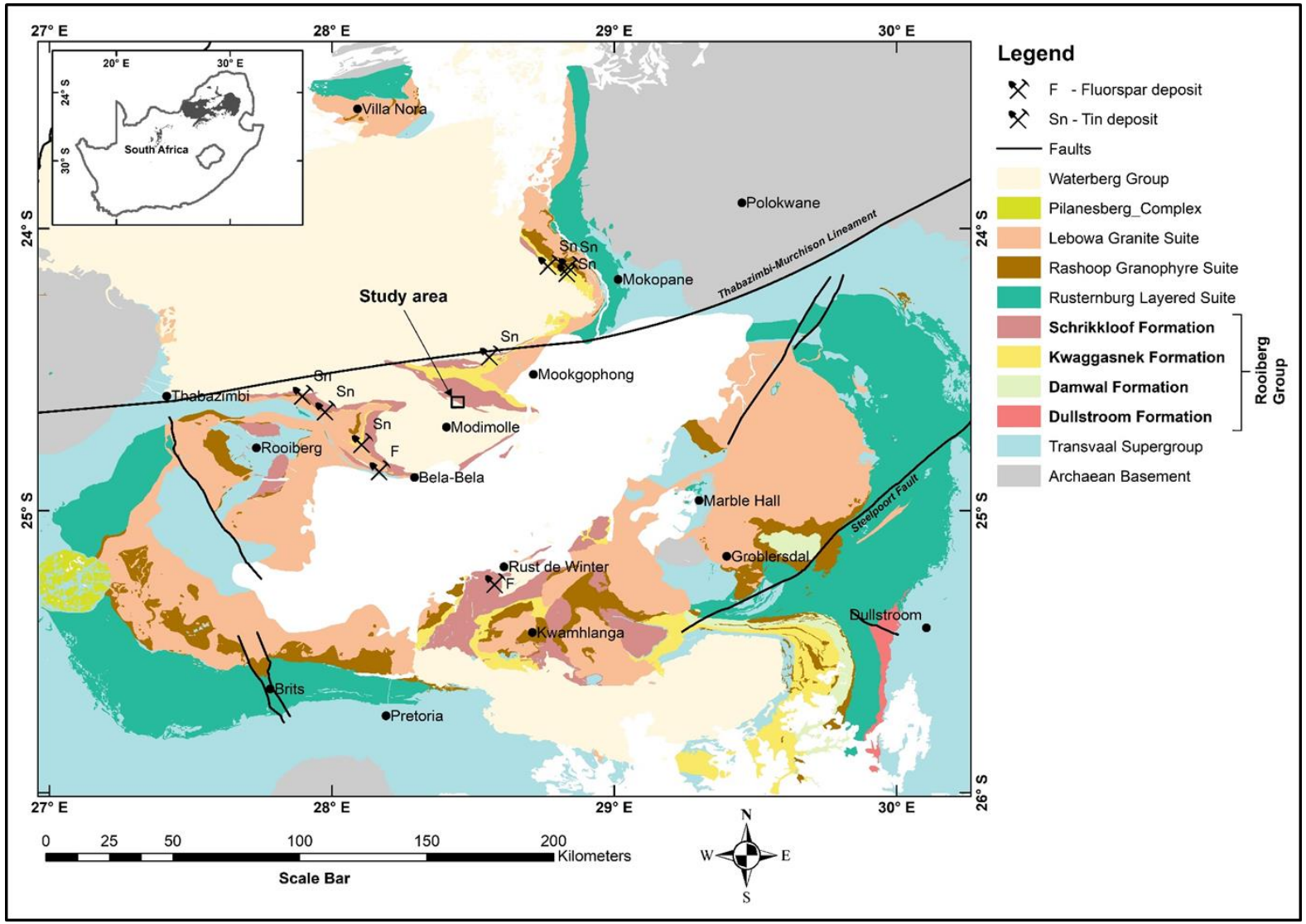

Figure 1.1: Regional geological map of the Rooiberg Group and Bushveld Igneous Complex. The study area (black square) is at the uppermost part of the Schrikkloof Formation approximately 20 km north of Modimolle.

1.2 Literature review

1.2.1 Geology

Previous geological research on the Rooiberg Group began in the early 1900s. Early research by Mellor (1905) aimed to understand and characterise the Rooiberg Group volcanics as well as its surrounding sedimentary units near Waterberg and Modimolle (Nylstroom).

Willemse (1969) noted that the Rooiberg Group covers an area of approximately 67 000 km^2 mainly roofing the Bushveld Igneous Complex. Twist and French (1983) estimated the initial erupted volume of Rooiberg volcanics to be more than 300 000 km^3 and further stated that this voluminous acid phase terminated deposition of the Transvaal Supergroup and thereby signalled the emplacement of the Bushveld Igneous Complex.

Martini (1988) indicated As-Zn vein type mineralisation in the Damwal Formation of the Rooiberg Group, approximately 5 km west of Stoffberg. Harmer and Farrow (1995) suggested that Rb-Sr and Pb-Pb isotopes in the Rooiberg Group are a potential exploration tool for Lebowa Granite Suite related hydrothermal mineralisation. The currently accepted subdivision of the Rooiberg Group, from oldest to youngest, into Dullstroom, Damwal, Kwaggasnek and Schrikkloof Formations was proposed by Schweitzer et al. (1995a). Hatton and Schweitzer (1995) proposed that the extrusive Rooiberg Group and intrusive granophyres were simultaneously emplaced, then subsequently intruded by the Rustenburg Layered Suite and Lebowa Granite Suite (which concluded Bushveld Igneous Complex magmatism).

Schweitzer et al. (1995b) summarised mineralisation of the Rooiberg Group into 4 phases: (1) hydrothermal Cu mineralisation in the Damwal Formation linked to the intrusion of the Rustenburg Layered Suite; (2) As-Zn mineralisation in the Damwal Formation linked to the intrusion of granophyres; (3) Pb-Zn mineralisation similarly linked to the intrusion of the Rustenburg Layered Suite; and (4) Lebowa Granite Suite related Sn and F deposits hosted in the Kwaggasnek and Schrikkloof Formations of the Rooiberg Group. Hou et al. (2017) confirmed that the fluorite enrichment of the Vergenoeg Fluorspar pipe deposit, which is hosted in the Schrikkloof Formation, is due to hydrothermal fluids with the pipe enhancing fluid migration in the system.

1.2.2 Petrogenesis

Daly and Molengraaff (1924) and Hall (1932) proposed that the Rooiberg Group and Lebowa Granite Suite were formed by differentiation of magma that led to the emplacement of the Rustenburg Layered Suite. However, Rhodes (1975) suggested that the source of this voluminous volcanic group and the Bushveld Igneous Complex was of an impact meteorite origin.

Walraven (1997) estimated the isotopic age of the Rooiberg Group at 2061 ± 2 Ma using the single-grain zircon Pb-evaporation technique. Schweitzer et al. (1997) suggested that the Rooiberg Group, Rashoop Granophyre Suite and Lebowa Granite Suite were sourced from melting of upper continental crust by mantle plume magmas. According to Buchanan et al. (1999), volcanic rocks of the Dullstroom Formation were derived from assimilation of continental crust by a mantle plume and that the evidence does not support the meteorite impact hypothesis of Rhodes (1975) for the source of the Bushveld Igneous Complex.

Buchanan et al. (2002) used both major and trace elements geochemistry to suggest that the dacites and rhyolites of the Damwal and Kwaggasnek Formations are petrogenetically related to the low-Ti volcanic rocks of the Dullstroom Formation. Isotopic compositions of the Rooiberg Group, studied by Buchanan et al. (2004), indicate that these volcanic rocks and the Rustenburg Layered Suite were derived from the same or similar magma source. VanTongeren et al. (2010, 2016), Mathez et al. (2013) proposed that felsic rocks (Rooiberg Group and Rashoop Granophyre Suite) were derived by fractional crystallisation of ultramafic to mafic magmas (Rustenburg Layered Suite) of the Bushveld Igneous Complex. Van Tongeren and Mathez (2015) proposed that the mafic magmas in the Eastern Limb of the Bushveld Igneous Complex were emplaced at deeper stratigraphic levels towards the northern segment and become shallower to the southern segment.

Lithofacies studies by Lenhardt and Eriksson (2012) indicated that the depositional environment of the Rooiberg Group was intracontinental and subaerial within active Transvaal Supergroup clastic sedimentation. Field observations by Lenhardt et al. (2017) suggested that the Rooiberg Group units can be interpreted as ‘lava-like’, rheomorphic ignimbrites, which were deposited in by explosive, subaerial volcanism.

1.3 Hydrothermal breccias

The term hydrothermal breccia refers to rocks formed by hydrothermal fluids where hydraulic pressure exceeds lithostatic pressure within a continental epithermal environment at depths typically less than 1500 m and temperatures ranging from 50-200°C (Jébrak, 1997; Robb, 2005). The formation of hydrothermal breccias was described by Jébrak (1997) as occurring in three stages, namely - propagation, wear and dilation (Figure 1.2).

- Fracture propagation (initial fluid-rock interaction) develops when fluid pressure is much greater than lithostatic pressure; this process is also referred to as hydrofracturing. This process is associated with minor volume expansion and corrosive wear (linked to stress corrosion caused by fluids). This process is predominantly a physical or mechanical process, there is minor chemical alteration.
- The wear abrasion stage occurs after fracture propagation and this process is caused by suspended (floating) particles in solution whereby friction is caused by hard particles such as quartz. This process has less fluid assisted brecciation compared to fracture propagation. Other processes associated with wear abrasion are fluid assisted brecciation, corrosive wear and volume expansion (Figure 1.2).
- The dilation stage occurs when fluid fractures are interconnected, which subsequently leads to fluid percolation, corrosive wear (chemical alteration), and collapse. This is accompanied by minor volume reduction, which might be caused by collapse.

As the fluid brecciation process evolves, a network of interconnected veins and veinlets will develop and form various textures. Ore fluids may form in any of the fluid brecciation phases mentioned above (Jébrak, 1997; Robb, 2005). During stage 1, fracture propagation, fluids may precipitate metals because of decreasing pressure (also referred to as first boiling). In stage 2, wear abrasion, metals can be precipitated in multi-phase processes whereby there is overprinting of alteration processes. During the final stage, dilation, metals can be precipitated due to fluid cooling or mixing (i.e. hydrothermal fluid and groundwater) and this process is independent of pressure (Jébrak, 1997; Robb, 2005).

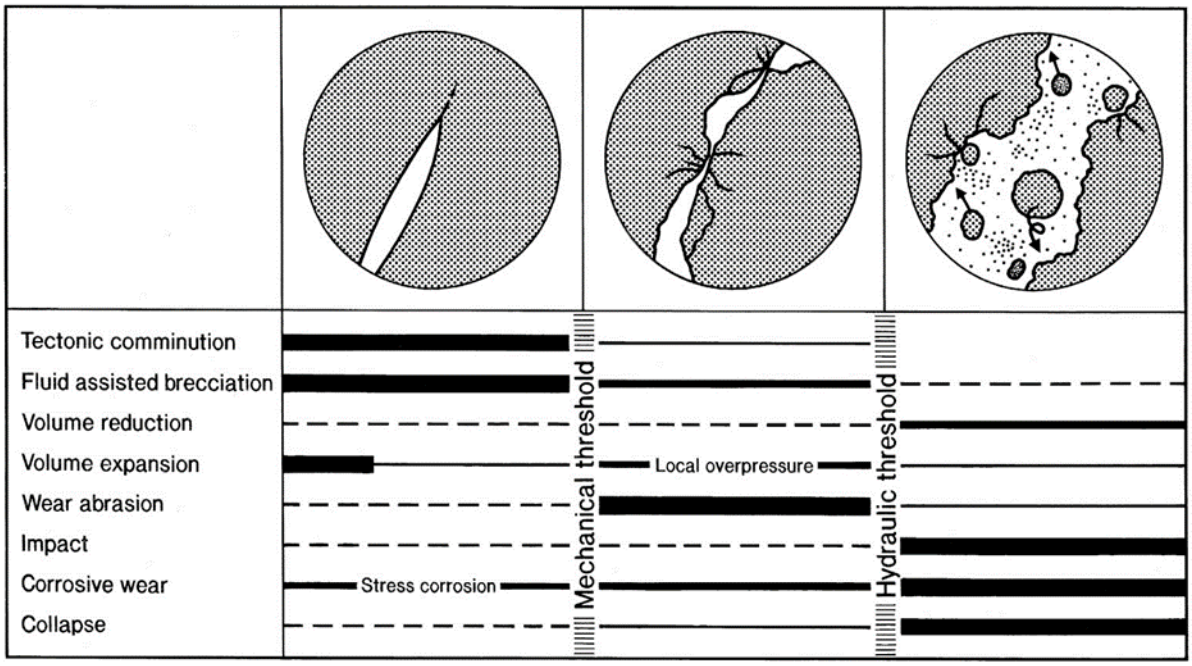

Figure 1.2: The three stages (propagation, wear and dilation) of hydrothermal breccia formation. These stages are separated by a mechanical discontinuity (between propagation and wear stages) as well as a hydraulic discontinuity (between wear and dilation); adopted from Jébrak (1997).

2 Regional geology and stratigraphy

The Bushveld Igneous Complex, a large voluminous layered mafic to felsic igneous province, intruded to some extent discordantly into the Transvaal Supergroup between approximately 2061 ± 2 Ma to 2054 ± 2 Ma; a period of approximate 6 million years or less (Walraven and Hattingh, 1993; Walraven, 1997; Cawthorn et al., 2006; Clarke et al., 2009; Van Tongeren and Mathez, 2015). This event produced regional contact aureoles along proximal margins of the country rock, predominantly the Transvaal Supergroup (Schweitzer and Hatton, 1995; Cawthorn et al., 2006; Clarke et al., 2009; VanTongeren and Mathez, 2015).

The proposed subdivision of the Bushveld Igneous Complex, from oldest to youngest, into the Rooiberg Group, Rustenburg Layered Suite, Rashoop Granophyre Suite and Lebowa Granite Suite, based on age and spatial relationship (Cawthorn et al., 2006). Furthermore, the Rooiberg sequence is subdivided into the Dullstroom, Damwal, Kwaggasnek and Schrikkloof Formations (Figure 2.1; Schweitzer et al., 1995a; Buchanan, 2006). This thesis focuses on the upper Schrikkloof Formation as indicated on the stratigraphic column (Figure 2.1). In the Modimolle area, the upper Schrikkloof Formation is overlain by clastic sediments of the Swaershoek Formation (Nylstroom Subgroup) which is the lowermost part of the Waterberg Group.

2.1 Rooiberg Group

The Rooiberg Group was emplaced as a volcanic sequence of basaltic-andesitic lavas at the base to more dominant rhyolitic lavas at the top (Schweitzer et al., 1995a; Buchanan, 2006; Lenhardt and Eriksson, 2012). This sequence of predominantly rhyolitic lavas cooled rapidly and was later intruded by the Rustenburg Layered Suite,

Rashoop Granophyre Suite and Lebowa Granite Suite (Schweitzer et al., 1995a, 1995b; Hatton and Schweitzer, 1995; Buchanan, 2006; Lenhardt and Eriksson, 2012; Lenhardt et al., 2017).

Widespread contact metamorphism of the Rooiberg Group is supported by contact aureoles in the east and southeast portion of the Bushveld Igneous Complex, where the Rustenburg Layered Suite and Rashoop Granophyre Suite are in direct contact with the Rooiberg Group (Figure 1.1; Schweitzer and Hatton, 1995).

The intrusion of the Lebowa Granite Suite into the Rooiberg Group is strongly linked with exogranitic hydrothermal mineralisation, hosted within this volcanic sequence (Schweitzer et al., 1995b; Crocker et al., 2001). The age of the Lebowa Granite Suite related hydrothermal fluids, dated 1957 ±15 Ma, as well as exhumation events of these granites at 1790 ± 114 Ma to 1604 ± 70 Ma suggest that mineralisation was periodic (Robb et al., 2000). Exogranitic ore deposits hosted in the Rooiberg Group typically consist of polymetallic Sn-Fe-F-REE mineralisation (Robb et al., 2000; Crocker et al., 2001). The styles of mineralisation are typically stratabound irregular veins (i.e. Union Tin Mine), breccia pipes (e.g., Vergenoeg Fluorspar-Hematite pipe) and contact breccia porphyry (e.g., Zwartkloof Fluorspar Mine; Robb et al., 2000; Crocker et al., 2001). These styles of mineralisation are hosted mainly in the Kwaggasnek and Schrikkloof Formations (Schweitzer et al., 1995b; Crocker et al., 2001).

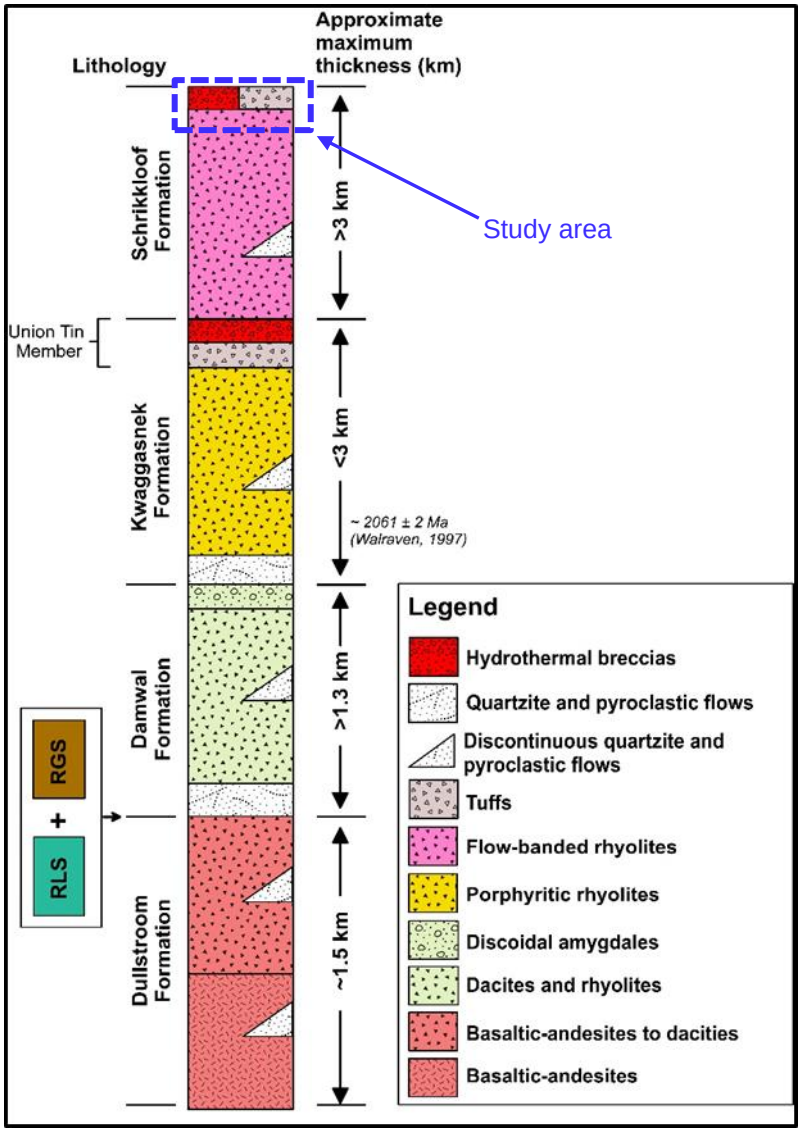

Figure 2.1: General stratigraphy of the Rooiberg Group. The stratigraphic unit of interest for the current study is marked by the blue dashed rectangle. Modified from Schweitzer et al., (1995a) and Buchanan (2006).

2.1.1 Dullstroom Formation

The Dullstroom Formation outcrops mainly in the south-eastern fragment of the Rooiberg Group (Figure 1.1) and is predominantly composed of basaltic-andesites, capped by rhyolites (Schweitzer et al., 1995a; Buchanan, 2006). This volcanic unit is approximately 1500 m thick (Figure 2.1) and interlayered with discontinuous clastic sedimentary rocks, mainly sandstone, as well as pyroclastic rocks (Schweitzer et al., 1995a; Buchanan, 2006). TiO_2 and SiO_2 contents in the Dullstroom Formation

generally increase with stratigraphic height (Schweitzer et al., 1995a and 1995b). MgO content is high (greater than 0.1 wt.%) throughout out the unit, but decreases towards the top (less than 0.1 wt.%; Schweitzer et al., 1995a). A thin but regionally preserved layer of pyroclastic flow deposit-quartzite marks the contact between the Dullstroom and the overlying Damwal Formations (Schweitzer et al., 1995a; Buchanan, 2006).

2.1.2 Damwal Formation

The Damwal Formation overlies the Dullstroom Formation in the south-eastern portion of the Bushveld Igneous Complex (Figure 1.1). In places, the Damwal and Dullstroom Formations are separated by the Rustenburg Layered Suite (Schweitzer et al., 1995a; Buchanan, 2006; VanTongeren and Mathez, 2015). The Damwal Formation outcrops 40 km east as well as south of Groblersdal (Figure 1.1) and is characterised by porphyritic dacites and rhyolites; this unit becomes more siliceous towards the top (Schweitzer et al., 1995a; Buchanan, 2006).

The rhyolites and dacites are interbedded with discontinuous clastic sediments, mainly sandstone, and pyroclastic deposits (Twist and French, 1983; Schweitzer et al., 1995a; Buchanan, 2006). The Damwal Formation is predominantly porphyritic in texture with a geochemical signature characterised by high Fe-Ti-P content at the base and predominantly low-magnesium (Mg < 0.1 wt.%) at the top (Schweitzer et al., 1995a; Lenhardt et al., 2017).

The thickness of this entire volcanic unit is estimated at approximately 1300 m (Figure 2.1; Twist and French, 1983; Schweitzer et al., 1995a; Buchanan, 2006). The uppermost portion of the Damwal Formation is marked by a thin layer of disc shaped amygdales which is overlain by a thin regional quartzite layer of the Kwaggasnek

Formation (Twist and French, 1983; Schweitzer et al., 1995a; Crocker et al., 2001; Buchanan, 2006).

2.1.3 Kwaggasnek Formation

A thin quartzite layer which caps the Damwal Formation marks the base of the Kwaggasnek Formation (Twist and French, 1983; Schweitzer et al., 1995a; Crocker et al., 2001; Buchanan, 2006). This unit is predominantly characterised by flow-banded porphyritic rhyolites, interlayered with discontinuous siliciclastic sedimentary (mainly sandstone) and pyroclastic rocks (Twist and French, 1983; Schweitzer et al., 1995a; Crocker et al., 2001; Buchanan, 2006). The SiO_2 content of these rhyolites is in excess of 72 wt.% (Buchanan et al., 1999, 2002, 2004). This ca. ~3000m thick unit is flow-banded at the top with quartzite xenoliths (up to 10 m in diameter) overlain by agglomerates and tuffs of the Union Tin Member, which caps the Kwaggasnek Formation (Figure 2.1; Twist and French, 1983; Schweitzer et al., 1995a; Crocker et al., 2001; Buchanan, 2006).

2.1.4 Schrikkloof Formation

The Schrikkloof Formation consists of sparsely porphyritic and strongly flow-banded rhyolites, which overlie the Union Tin Member of the Kwaggasnek Formation (Schweitzer et al., 1995a; Crocker et al., 2001; Buchanan, 2006; Lenhardt et al., 2017). These rhyolites are more than 3000m thick, commonly characterised by quartzite xenoliths (up to 10 m in diameter) at the base and are interlayered with thin discontinuous tuffs and sandstone lenses (Schweitzer et al., 1995a; Crocker et al., 2001; Buchanan, 2006). The Schrikkloof Formation is capped by an ash-flow tuff, also referred to as an ignimbrite (Schweitzer et al., 1995a; Crocker et al., 2001; Buchanan, 2006). This thin layer of ignimbrites is known to host Sn and fluorspar mineralisation

commonly associated with chloritisation alteration, linked to the former, hematitisation and fluorspar replacement alteration linked to the latter (Schweitzer et al., 1995b; Robb et al., 2000; Crocker et al., 2001). Details on the types of deposits hosted in the Schrikkloof and Kwaggasnek Formations are discussed below in section 2.1.5.

2.1.5 Sn-F-REE deposits in the Rooiberg Group

There are two types of mineralisation which have been mined in the Rooiberg Group, namely fluorspar (CaF_2) and tin (Sn) deposits; the main examples include the Vergenoeg Fluorspar deposit and Union Tin Mine, respectively (Schweitzer et al., 1995b; Robb et al., 2000; Crocker et al., 2001; Goff et al., 2004; Kinnaird et al., 2004; Graupner et al., 2015). These two ore deposit types have similar but yet distinguishable characteristics listed below on Table 2.1. The characteristics are used as illustrations to summarize similar mineralisation in the Rooiberg Group.

The similarities between fluorspar and tin deposits of the Rooiberg Group include tectonic setting (central margin of craton) and their relationship to the Lebowa Granite Suite, as exogranitic styles of mineralisation (Schweitzer et al., 1995b; Robb et al., 2000; Crocker et al., 2001; Goff et al., 2004; Kinnaird et al., 2004; Graupner et al., 2015).

Union Tin Deposit

The Union Tin Member of the Upper Kwaggasnek Formation hosts exogranitic Sn deposit of the Bushveld Igneous Complex (Schweitzer et al., 1995b; Crocker et al., 2001). The term “Union Tin Member” was coined after one of the mining groups, the “Union Tin Mines Ltd” (Crocker et al., 2001). This tin deposit produced approximately

10.3 Kt Sn metal at an average of 9.1 wt.% cassiterite (SnO_2) which is the dominant ore mineral for Sn extraction (Crocker et al., 2001).

Table 2.1: Characteristics of the Union Tin Deposit and Vergenoeg Fluorspar Deposit.

	Union Tin (Sn)	**Vergenoeg (Fe-F-REE)**
Age	-	2040 ± 46 Ma (Graupner et al., 2015)
Tectonic setting	Central margin of Craton	Central margin of Craton
Granite relationship	Exogranitic	Exogranitic
Deposit Size	10.3 Kt at 9.1% SnO_2 *	174 Mt at 28.1% CaF_2
Formation	Kwaggasnek Formation	Schrikkloof Formation
Host rock	Ash flow tuff or ignimbrite	Ash flow tuff or ignimbrite
Orebody morphology	Stratabound irregular veins	Vertical pipe
Ore host	Chlorite veins	Fluorite-hematite breccia
Ore minerals	Cassiterite (SnO_2)	Fluorite (CaF_2)
Ore assemblage	Sn	F-Fe-REE
Fe bearing minerals	Hematite, magnetite, chalcopyrite, pyrite	Hematite; magnetite
REE bearing minerals	Apatite	Fluorite, monazite, xenotime
Alteration style	Chloritisation, sericitisation, silicification	Fluorite replacement, hematitisation, K-metasomatism

*Historic production

Cassiterite in this deposit is associated with stratabound irregular chloritised veins (Schweitzer et al., 1995b; Robb et al., 2000; Crocker et al., 2001). The common alteration associated with this deposit includes chloritisation, sericitisation as well as silicification (Robb et al., 2000; Crocker et al., 2001). The iron bearing minerals include hematite, magnetite, chalcopyrite and pyrite (Robb et al., 2000; Crocker et al., 2001).

Vergenoeg Fluorspar Deposit

The Vergenoeg Fluorspar Deposit is hosted within a tuff or ignimbrite of the upper Schrikkloof Formation and is one of the largest producers of fluorite in the world (Figure 2.2; Schweitzer et al., 1995b; Robb et al., 2000; Crocker et al., 2001; Goff et al., 2004; Kinnaird et al., 2004; Graupner et al., 2015). This deposit has to date been estimated at 174 Mt at 28.1 wt.% fluorite (CaF_2) (Fourie, 2000; Graupner et al., 2015). This fluorspar deposit is hosted in the Vergenoeg Igneous Complex which is a sub-vertical breccia pipe with a 900 m diameter and commonly more than 600 m deep (Figure 2.2; Crocker et al., 2001; Goff et al., 2004; Kinnaird et al., 2004; Graupner et al., 2015). The breccias have a jigsaw-like texture (crackle breccia?) and are cemented by a fluorite-hematite mineral assemblage (Crocker et al., 2001; Goff et al., 2004; Graupner et al., 2015).

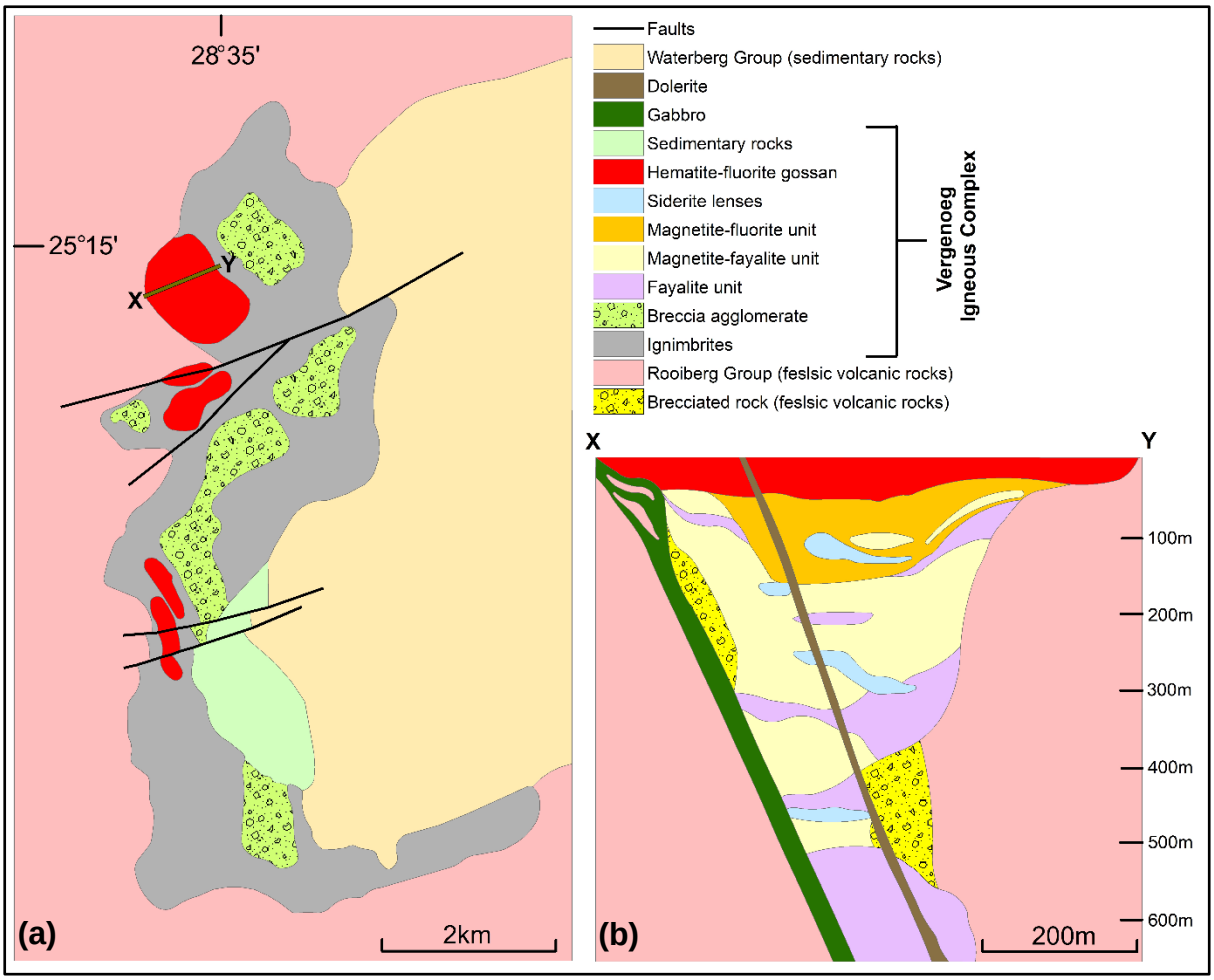

Figure 2.2 (a) A geological map indicating the lateral extent of the Vergenoeg Igneous Complex relative to the Rooiberg Group. (b) Cross section X-Y of the Vergenoeg pipe and the associated units. Modified from Goff et al., (2004) and Graupner et al., (2015).

Fluorite is the main ore mineral with iron (Fe) and rare earth elements (REE) extracted as by-products, hence the F-Fe-REE notation (Crocker et al., 2001; Graupner et al., 2015). The Fe-bearing minerals are mainly hematite and magnetite, whereas the REE-bearing minerals include fluorite, monazite and xenotime (Robb et al., 2000; Crocker et al., 2001; Goff et al., 2004; Kinnaird et al., 2004; Graupner et al., 2015). The common alteration styles include fluorite replacement, hematitisation and K-metasomatism as sericitisation (Robb et al., 2000; Crocker et al., 2001; Goff et al., 2004; Kinnaird et al., 2004; Graupner et al., 2015).

2.2 Waterberg Group in the Modimolle area

Within the Nylstroom Basin, the Waterberg Group unconformably overlies the felsic rocks of the Rooiberg Group (Jansen, 1982; Callaghan et al., 1991; Callaghan, 1993; Barker et al., 2006). The Waterberg Group is predominantly an arenite (sandstone and quartzite) sequence, interbedded with mudrocks, siltstones, conglomerates, and grits (Jansen, 1982; Callaghan et al., 1991; Callaghan, 1993; Barker et al., 2006). This sequence is subdivided into three subgroups, namely (from oldest to youngest) the Nylstroom, Matlabas and Kransberg Subgroups (Figure 2.3; Jansen, 1982; Callaghan et al., 1991; Callaghan, 1993; Barker et al., 2006). Each of these three clastic sedimentary subgroups are generally characterised by upward-fining sequences, defined by medium- to coarse-grained sandstones at the base to mudrocks and siltstones at the top (Jansen, 1982; Callaghan et al., 1991; Callaghan, 1993; Hanson et al., 2004; Barker et al., 2006).

2.2.1 Nylstroom Subgroup

The Nylstroom Subgroup is subdivided into the Swaershoek and Alma Formations (Figure 2.3; Jansen, 1982; Callaghan et al., 1991; Callaghan, 1993; Hanson et al., 2004; Barker et al., 2006). The Swaershoek Formation is approximately ~2500 m thick (Figure 2.3) and characterised by conglomerates, siltstones and mudrocks at the base, overlain by massive pebbly (conglomeratic) arenites, which are intruded by dolerites (Jansen, 1982; Callaghan et al., 1991; Callaghan, 1993; Hanson et al., 2004; Barker et al., 2006). The dolerites have U-Pb isotope crystallisation ages of ~1879 to ~1872 Ma, confining the deposition of the Swaershoek Formation to a minimum age of ~1872 Ma (Jansen, 1982; Callaghan et al., 1991; Callaghan, 1993; Hanson et al., 2004; Barker et al., 2006). The depositional environment of the Swaershoek Formation is

thought to have been fan-deltas to tidal flats (Jansen, 1982; Callaghan et al., 1991; Callaghan, 1993; Hanson et al., 2004; Barker et al., 2006).

The younger, ~2500 m thick Alma Formation overlies the Swaershoek Formation (Figure 2.3) and is characterised by medium- to coarse-grained, greenish grey feldspathic sandstones that are interbedded with mudrocks, siltstones and conglomerates (Jansen, 1982; Callaghan et al., 1991; Callaghan, 1993; Hanson et al., 2004; Barker et al., 2006). Deposition of the Alma Formation took place by a sequence of alluvial fans, forming a “bajada”, or a series of alluvial fans forming a concentric river pattern along a mountain range (Jansen, 1982; Callaghan et al., 1991; Callaghan, 1993; Hanson et al., 2004; Barker et al., 2006).

The study area covers a contact between the upper Schrikkloof Formation of the Rooiberg Group and the younger lower Swaershoek Formation of the Nylstroom Subgroup, which forms the lower portion of the Waterberg Group. The younger sedimentary sequences of the Waterberg Group (Alma Formation, Matlabas and Kransberg Subgroups) are excluded because beyond the scope of this study.

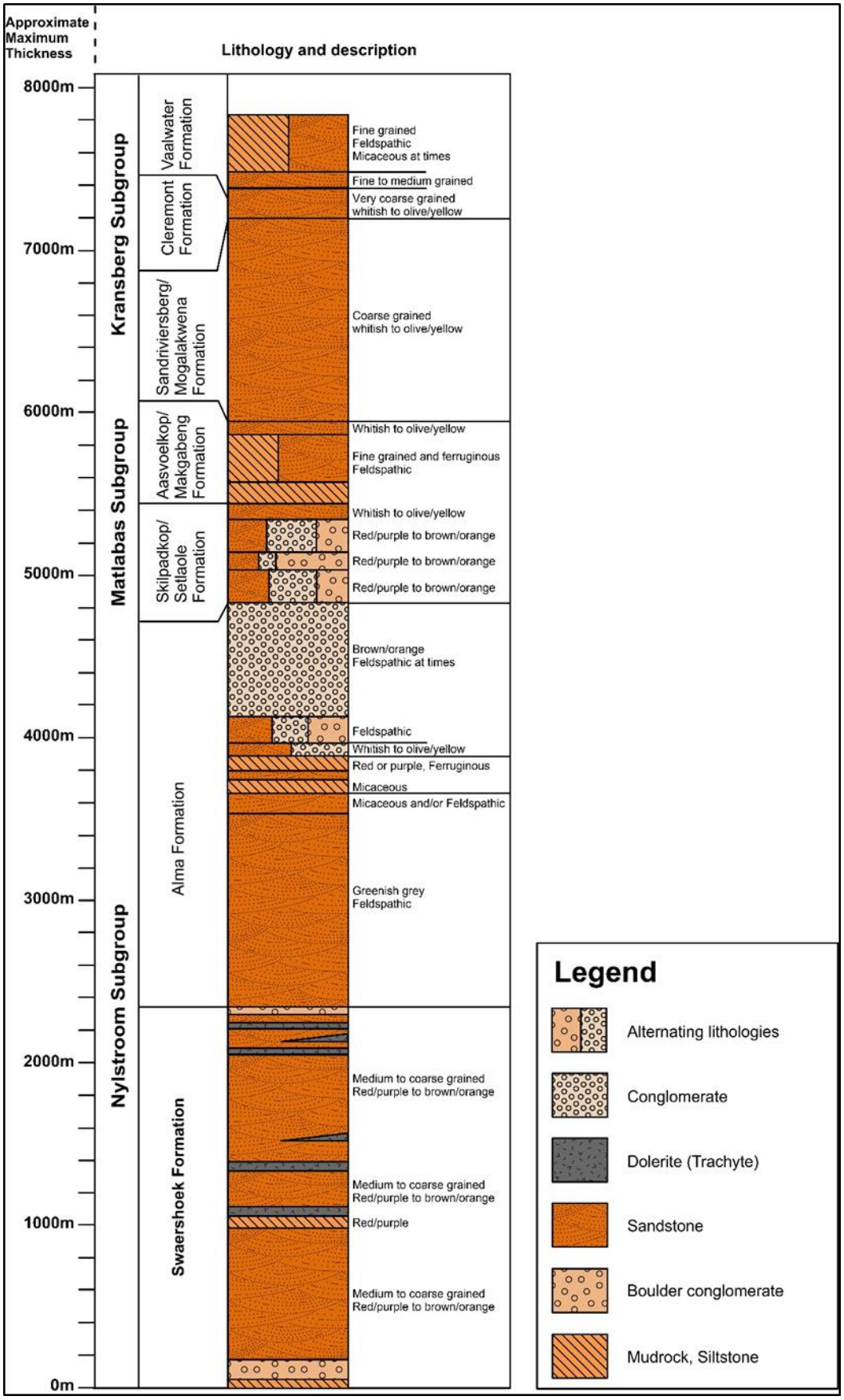

Figure 2.3: Simplified regional stratigraphy of the Waterberg Group. The lowermost portion of this sequence, the Swaershoek Formation, is part of the study area and overlies the Rooiberg Group. Modified from Jansen (1982) and Barker et al., (2006).

3 Methodology

A field excursion was undertaken to primarily map the local geology of the study area as well as document field observations and collect rock samples from the upper Schrikkloof. The main output of this field exercise was the geological map shown in chapter 4 (Figure 4.1). A total of 30 rock samples was collected on outcrops in the field from the Schrikkloof Formation. The sample locations were marked with a handheld Garmin 650 GPS.

All samples were separated for geochemical analysis and petrography with some of the original rock material preserved and stored. Fifteen selected rocks were prepared for polished thin section at the Council for Geoscience (CGS) Laboratory. Rocks were crushed, milled and pulverised to 75µm and submitted for major element and trace element analysis. Major elements were analysed at the CGS X-ray fluorescence (XRF) laboratory and trace elements were analysed by the Intertek Laboratory in Perth, Australia.

3.1 Petrography and SEM-EDX

A total of 15 rock samples was prepared for polished thin sections. These samples were cut to 30x20x10 cm blocks using the Discoplan TS cutter and grinder. These blocks are flattened for approximately 10 minutes using lubricant and lapping in the Logitech LP50 instrument. Once the blocks are flat, they are mounted and glued into glass slides using a resin hardener, and left overnight. These mounted rock blocks are grinded (using the Discoplan TS) to approximately 1mm thickness; the thickness of each mounted block was measured using a micrometre.

The ~1 mm mounted blocks are then grinded to the desired thickness (~30 µm) using a grit and water slurry in the Logitech LP50; this process takes approximately 10 minutes. Each ~30µm thin section is inspected using a transmitted light microscope to ensure that the correct thickness has been achieved. After thin sections are examined, a 3-micron diamond paste is used to polish each samples evenly. Subsequently, a 1-micron diamond paste used until the desired polishing is completed.

The polished thin sections were analysed and processed using an Olympus BX41 microscope equipped with the Olympus SC100 camera. Photomicrographs were taken using this microscope and camera with the aid of the "*analysis getIT*" software.

Two polished thin section were selected for SEM-EDX analysis at the University of Pretoria; These polished samples were carbon coated before they were inserted into the chamber room.

3.2 Major and trace element analysis

Sample preparation for XRF major element analysis included mixing approximately 12 g of each pulverised sample (grain size <75µm) with 3g of Hoechst wax in a homogeniser for roughly 10 minutes. This mixture was poured into aluminium cups and pressed (at ~400 MPa) into pellets using a hydraulic press. A "PANanalytical MagicX Fast" instrument (equipped with a Rh tube operated at 60 kV and 66 mA) was used for XRF analysis of pressed pellets at CGS. Contents of SiO_2, TiO_2, Al_2O_3, Fe_2O_3 (t), MnO, MgO, CaO, Na_2O, K_2O, P_2O_5 and Cr_2O_3 were measured The standard measuring time for each pressed pellet was 5 minutes. The 12/76 secondary amphibolite reference material (developed by the CGS) was used for instrument drift correction as well as quality assurance and quality control.

The major elements were reported as oxides in weight percent (wt.%). Loss on Ignition (LOI) was obtained by igniting 3 grams per sample in fused glass beads at 1000 °C in the furnace for 3 hours.

Trace elements were analysed at the Intertek Genalysis Perth Laboratory (in Australia) via Inductively Coupled Plasma Mass Spectrometry (ICP-MS) and Inductively Coupled Plasma Optical Emission Spectroscopy (ICP-OES) trace element analysis. Approximately 50 grams of each pulverised (<75µm) rock sample was sent to lab. Samples were dissolved using hydrofluoric (HF), nitric (HNO_3), perchloric ($HClO_4$) and hydrochloric (HCl) acids in Teflon tubes; this process is also referred to as 4 acid digestion.

3.3 Mass Balance

In any hydrothermal environment, there are elemental gains and/or losses in the rock associated with fluids circulating through the rock. These elemental gains and/or losses can be quantified by the isocon graphical method which is essentially based on the comparison of the least altered rock with the most altered rock (Grant, 1986; 2005). The isocon method provides an evaluation of the degree of element mass or loss and avoids the effect of a simultaneous increase or decrease in volume happening during alteration.

The slope of the isocon, in the graph, is defined as a straight line passing through the origin in a Cartesian plane and elements plotting above this line are considered gains but elements plotting below this line are considered losses (Grant, 2005). The isocon slope indicates the overall change in mass relative to the original mass ($\boldsymbol{M^O}$) (Grant, 2005). This slope can be determined using several methods mentioned below (Grant, 2005):

- Assuming certain elements are immobile in the system
- Clustering of slopes or best fit of data in a linear array
- Assuming constant mass
- Alternatively, assuming constant volume

On this study, the first approach (utilizing immobile elements during hydrothermal alteration) was the preferred method and the lithogeochemical data was used to examine possible elemental gains and losses.

The Gresens' (1967) equations, later modified by Grant (1986, 2005), can be used to quantify elemental gains and losses in hydrothermal alteration systems. The composition-volume equation by Gresens (1967) and Grant (1986, 2005) can be expressed as:

$$\boldsymbol{C_i^{\mathbf{A}} = \frac{M^{\mathbf{O}}}{M^{\mathbf{A}}} \left(C_i^{O} + \Delta C_i \right)} \qquad \textbf{[3.1]}$$

Where $\boldsymbol{C_i^{\mathbf{A}}}$ = concentration of chemical element "$\boldsymbol{i}$" in the altered (**A**) rock

$\boldsymbol{\frac{M^{\mathbf{O}}}{M^{\mathbf{A}}}}$ = slope of the isocon. $\boldsymbol{M^{\mathbf{O}}}$ and $\boldsymbol{M^{\mathbf{A}}}$ refer to the masses before and after hydrothermal alteration, respectively.

$\boldsymbol{C_i^{O}}$ = concentration of chemical element "$\boldsymbol{i}$" in the original (**O**) rock

$\boldsymbol{\Delta C_i}$ = is the change in concentration (gain or loss) of chemical element "$\boldsymbol{i}$"

When an immobile element is identified, whereby $\boldsymbol{\Delta C_i}$ = 0, the slope of the isocon $(\boldsymbol{M^O/M^A})$ can be estimated graphically by plotting $\boldsymbol{C_i^A}$ (on the Y-axis) against $\boldsymbol{C_i^O}$ (on the X-axis). The equation defining the slope of the isocon using immobile elements can be re-arranged and expressed as:

$$\frac{\boldsymbol{M^O}}{\boldsymbol{M^A}} = \frac{\boldsymbol{C_i^A}}{\boldsymbol{C_i^O}} \qquad \textbf{[3.2]}$$

Chemical elements plotting above this slope are considered gains whereas elements plotting below this line are losses. Equation 3.1 can be adjusted to estimate the mass gains/losses relative to the least altered rock $\boldsymbol{(\Delta C_i/C_i^O)}$. The mass gain/loss in a hydrothermal system for an element can be calculated using the equation below:

$$\frac{\boldsymbol{\Delta C_i}}{\boldsymbol{C_i^O}} = \left(\frac{\boldsymbol{M^A}}{\boldsymbol{M^O}}\right)\left(\frac{\boldsymbol{C_i^A}}{\boldsymbol{C_i^O}}\right) - \boldsymbol{1} \qquad \textbf{[3.3]}$$

Where $\frac{\boldsymbol{\Delta C_i}}{\boldsymbol{C_i^O}}$ = gains/loss relative to the original (least altered) rock,

$\frac{\boldsymbol{M^A}}{\boldsymbol{M^O}}$ = inverse to the isocon slope

$\frac{\boldsymbol{C_i^A}}{\boldsymbol{C_i^O}}$ = slope from the origin to the data point of element "$\boldsymbol{i}$"

The above mentioned approach and equations (3.1 – 3.3) were used in *section 5.3* to indicate which elemental gains and losses are associated with hydrothermal breccias and hematitised tuffs.

4 Local geology, field observations and petrography

The study area is located circa 20 km north of Modimolle and covers an area of approximately 12 km^2. The local geology is characterised by volcanic rocks (rhyolites and tuffs) of the Schrikkloof Formation, overlain by clastic sedimentary rocks (sandstones, conglomerates, mudrocks and siltstones) of the Swaershoek Formation, Waterberg Group, Figure 4.1. Both volcanic and clastic sedimentary sequences are approximately striking in the northwest-southeast direction, generally dipping southwest at roughly 35° (Figure 4.1 and 4.2).

In the field, rhyolites are characterised by flow-folded bands and have a brown weathered surface whereas in hand specimen (on the fresh surface) they appear dark grey. In contrast, tuffs appear to have a light coloured (whitish) weathering surface with angular greenish clasts of various sizes. Hydrothermal breccias appear to be confined within tuffaceous layers and are characterised by interconnected reddish to black hematite veins.

Sandstones of the Swaershoek Formation are cross-bedded and medium to coarse-grained; these sandstones are intruded by a medium to coarse-grained dolerite sill. Conglomerates are clast-supported with a clast to matrix ratio of more than 3:1. There are minor mudrock occurrences in the area but outcrops are not big enough to be shown in the map. The contact between lithologies is commonly covered by soil and as such the nature of contacts is inferred.

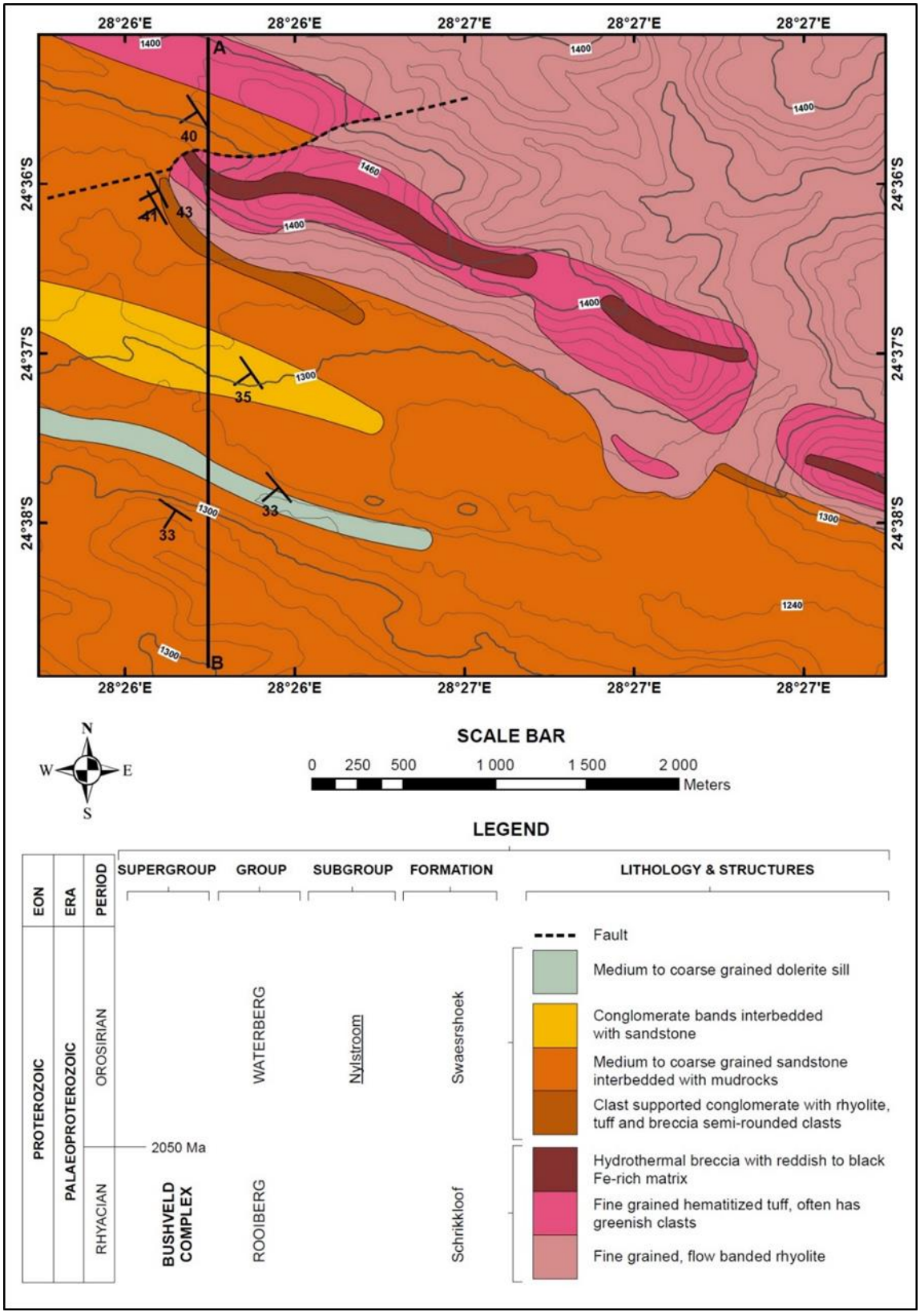

Figure 4.1: A detailed local geological map of the study area. Sediments of the Swaershoek Formation are approximately dipping south. This area was mapped by the author of thesis on September 2017. The location of this map is indicated on *Figure 1.1*.

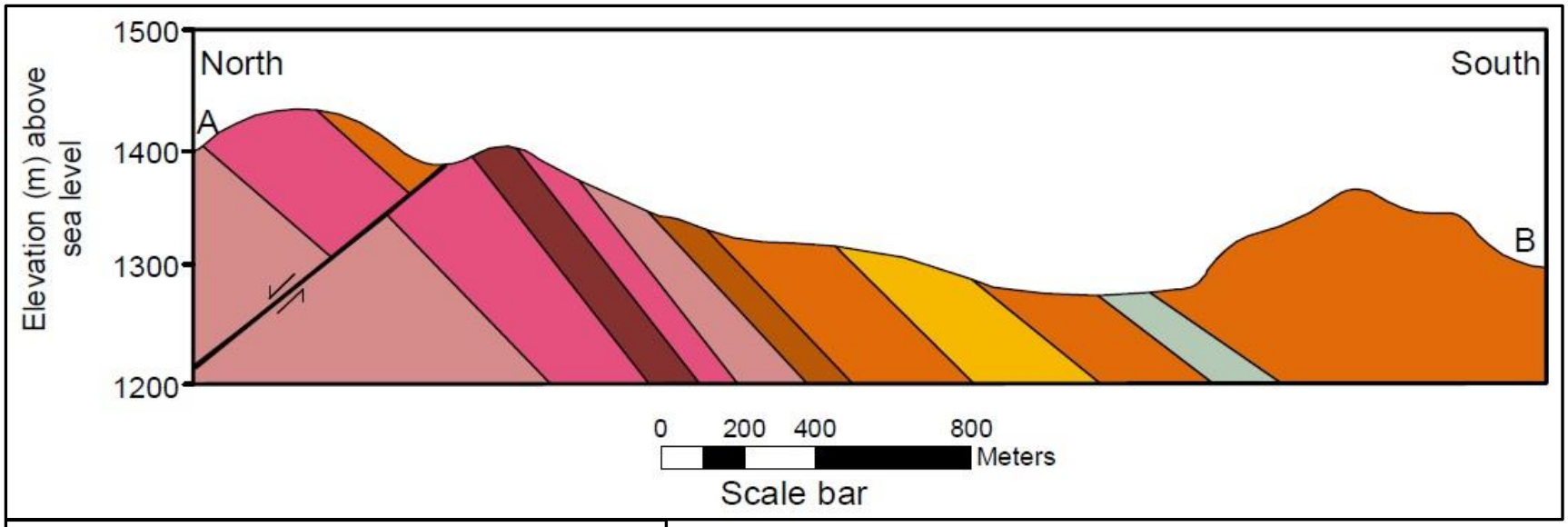

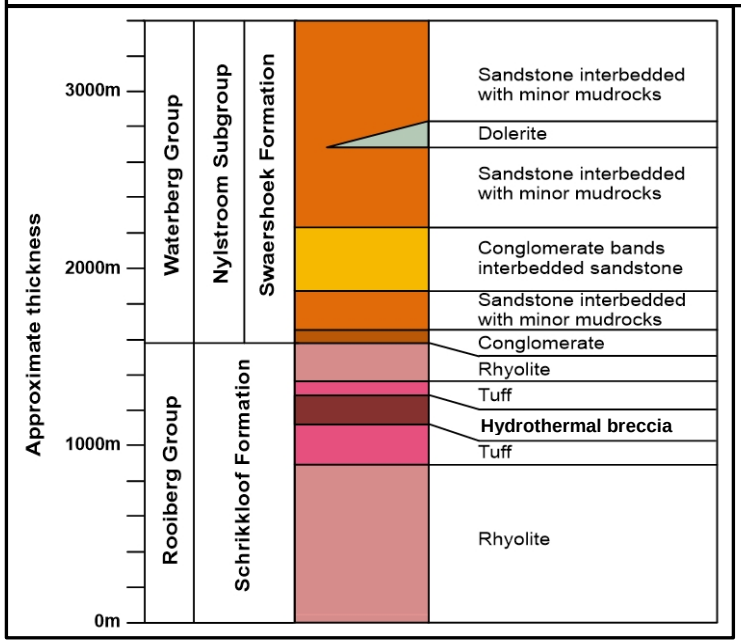

Figure 4.2: (a) A schematic cross-section of line A-B shown in the local geological map. The hydrothermal breccia appears to be sandwiched within tuffs. The younging direction of sediments is south-west. (b) The stratigraphic column of the study area derived from the cross-section above. The hydrothermal breccia unit has a maximum thickness of approximately 200m. The legend for the cross-section and stratigraphic column is the same as Figure 4.1 above.

4.1 Schrikkloof Formation

The lower portion of the Schrikkloof Formation is characterised by melanocratic, strongly flow-banded, fine grained and sparsely porphyritic rhyolites (Figure 4.3). There are fine grained quartz xenoliths of various size hosted within these rhyolites. The rhyolites are generally relatively unaltered as there are minor patches of hematitisation and silicification preserved.

The rhyolites are overlain by discontinuous tuffs, which are generally leucocratic, fine grained with greenish clasts (Figure 4.4a) as well as having vugs filled with fine grained Fe-minerals (i.e. hematite) and quartz. These tuffs appear to have experienced considerable hematitisation in most places (Figure 4.4b), which was subsequently followed by silicification.

The tuffs are also brecciated by Fe-rich fluids to form a layer of crackle to chaotic breccia (Figure 4.4b and 4.5). The Fe-rich fluids formed veins of various sizes which cement large clasts. The presence of crackle breccia (Figure 4.5b) indicates in-situ brecciation by fluids exerting hydrostatic pressure to fracture the rock.

The source of these Fe-rich fluids is possibly the Rooiberg Group itself or perhaps the differentiated granites of the Lebowa Granite Suite. The chaotic breccias might have formed first, as high fluid pressure over a short period of time is required to form this texture. But crackle breccia might have formed by fluids percolating from chaotic breccias.

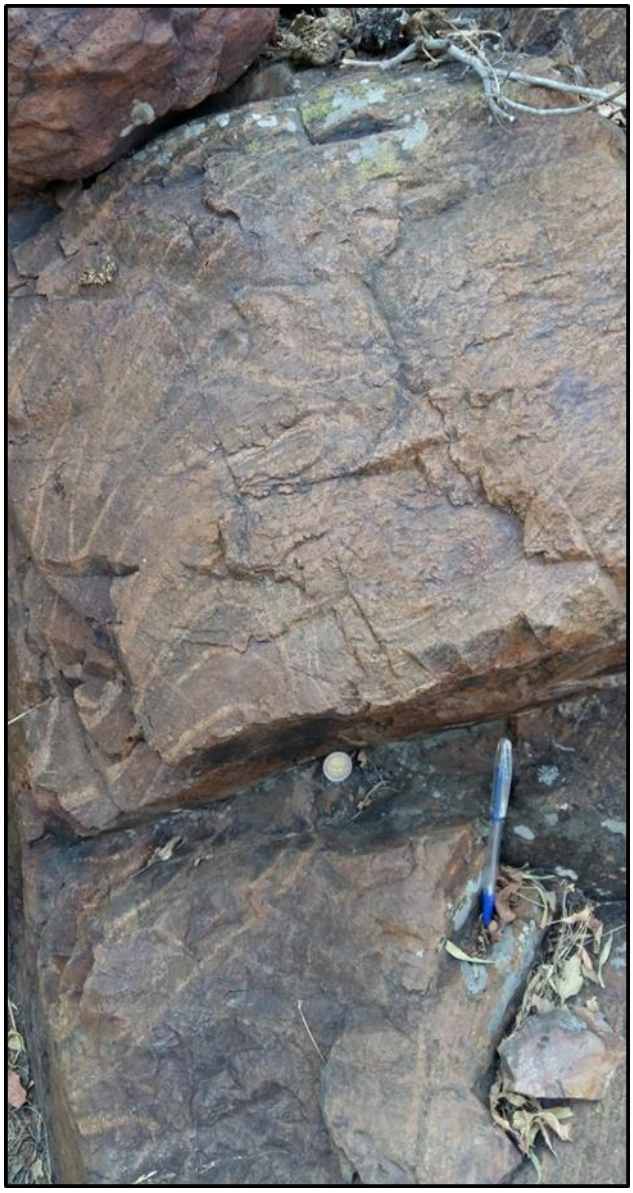

Figure 4.3: A fine grained (aphanitic) rhyolite outcrop of the Schrikkloof Formation with well-preserved flow bands. These rhyolites appear to be least affected by the hematitisation alteration.

The brecciation likely formed in a syndepositional environment and this suggests that fluids were internally derived from the Rooiberg Group. These fluids could be ore-forming fluids rich in base metals and rare earth elements (REE). The economic potential of the fluids was tested using SEM-EDX as well as performing geochemical analyses. The clastic sediments of the Swaershoek Formation are deposited above these altered tuffs.

Figure 4.4: (a) A fine grained, leucocratic and groundmass-supported tuff of the Schrikkloof Formation with green clasts. (b) A brecciated and hematitised tuff of the Schrikkloof Formation where the Fe-rich fluid is cementing angular and rotated clasts of the host rock.

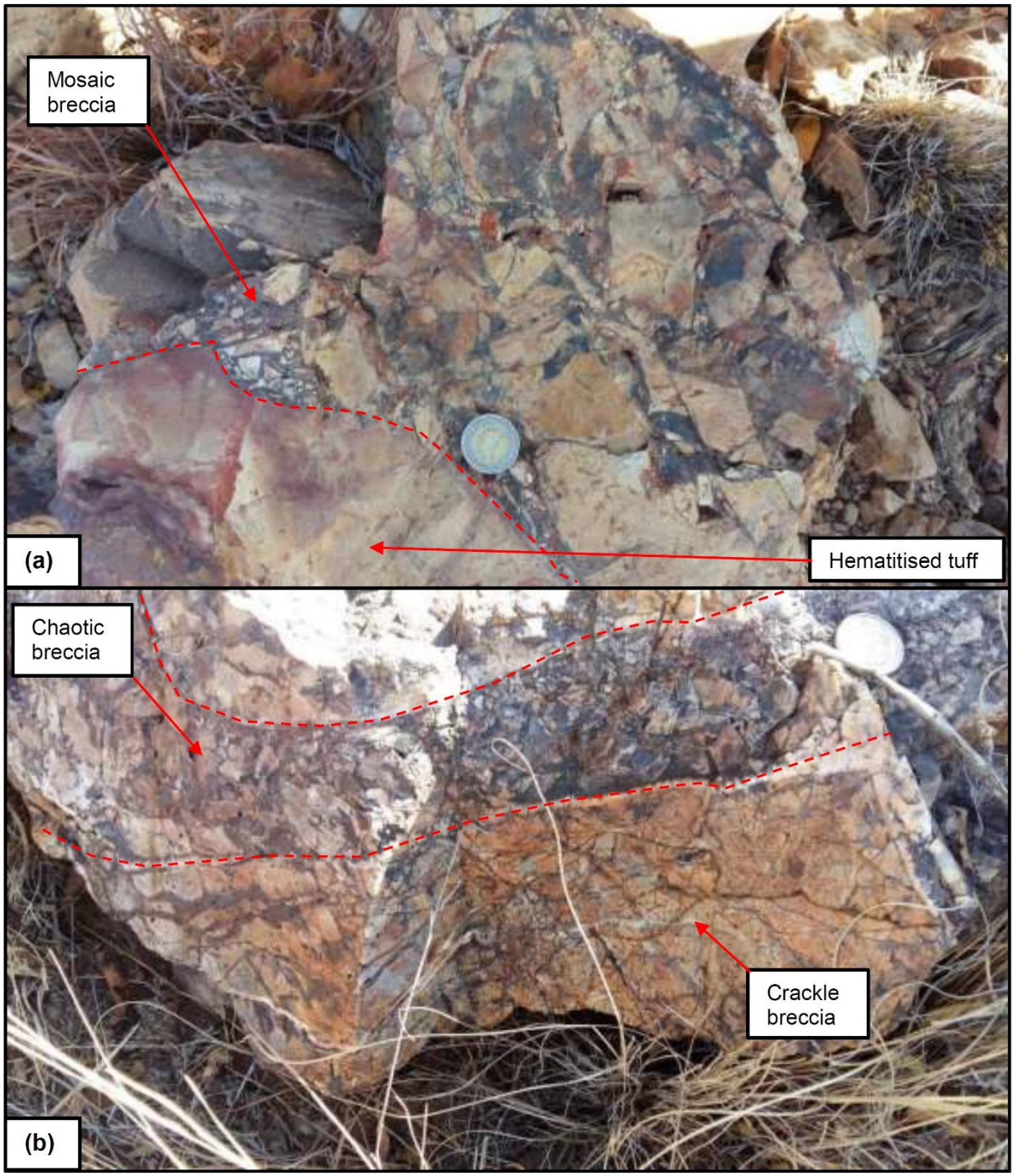

Figure 4.5: (a) Chaotic to mosaic hydrothermal breccia of the Schrikkloof Formation where clasts have been rotated by Fe-fluids. (b) Brecciated tuff of the Schrikkloof Formation with a band chaotic tuff band sandwiched in between crackle breccia.

4.2 Swaershoek Formation

The sedimentary rocks of the lower Swaershoek Formation are predominantly purplish arenite sandstone with discontinuous conglomerates and mudrocks (Figure 4.6). The arenite sandstone is medium to coarse grained, generally striking in a northwest-southeast direction and dipping southwest; conglomerates and mudrocks have similar orientations.

These sandstones commonly include sparsely rounded pebbles of various sizes and composition. Conglomerates are clast-supported with clasts comprising hematitised tuffs and rhyolites (Figure 4.6b); granitic clasts were not observed (as suggested by the literature; Barker et al., 2006). Mudrocks are fine to medium coarse grained and can be observed directly overlying the clast-supported conglomerates.

These sediments appear to have not been affected by hematitisation as observed in rhyolites. A dolerite intruding into arenites has been documented, with a “sill-like” orientation, as the morphology of this mafic lithology is NW-elongated. The dolerite sill is melanocratic, medium to coarse grained, equigranular and composed of plagioclase and pyroxene. Both dolerites and arenite sandstones are permeated by quartz veins of various sizes (Figure 4.6a), indicating silicification.

Figure 4.6: (a) A medium to coarse grained, cross bedded sandstone of the Swaershoek Formation which cross cut by quartz veins. (b) A sharp contact between basal clast supported conglomerate and sandstone of the Swaershoek Formation.

4.3 Contact between Schrikkloof and Swaershoek Formation

The nature of the contact between the felsic volcanics of the Schrikkloof Formation and sediments of the Swaershoek Formation appears to be sharp, although it is covered by shallow soil (Figure 4.7). The contact in the field is marked by a transition from fine-grained tuffs of the Schrikkloof Formation (Rooiberg Group) to clast-supported conglomerate of the Swaershoek Formation (Waterberg Group).

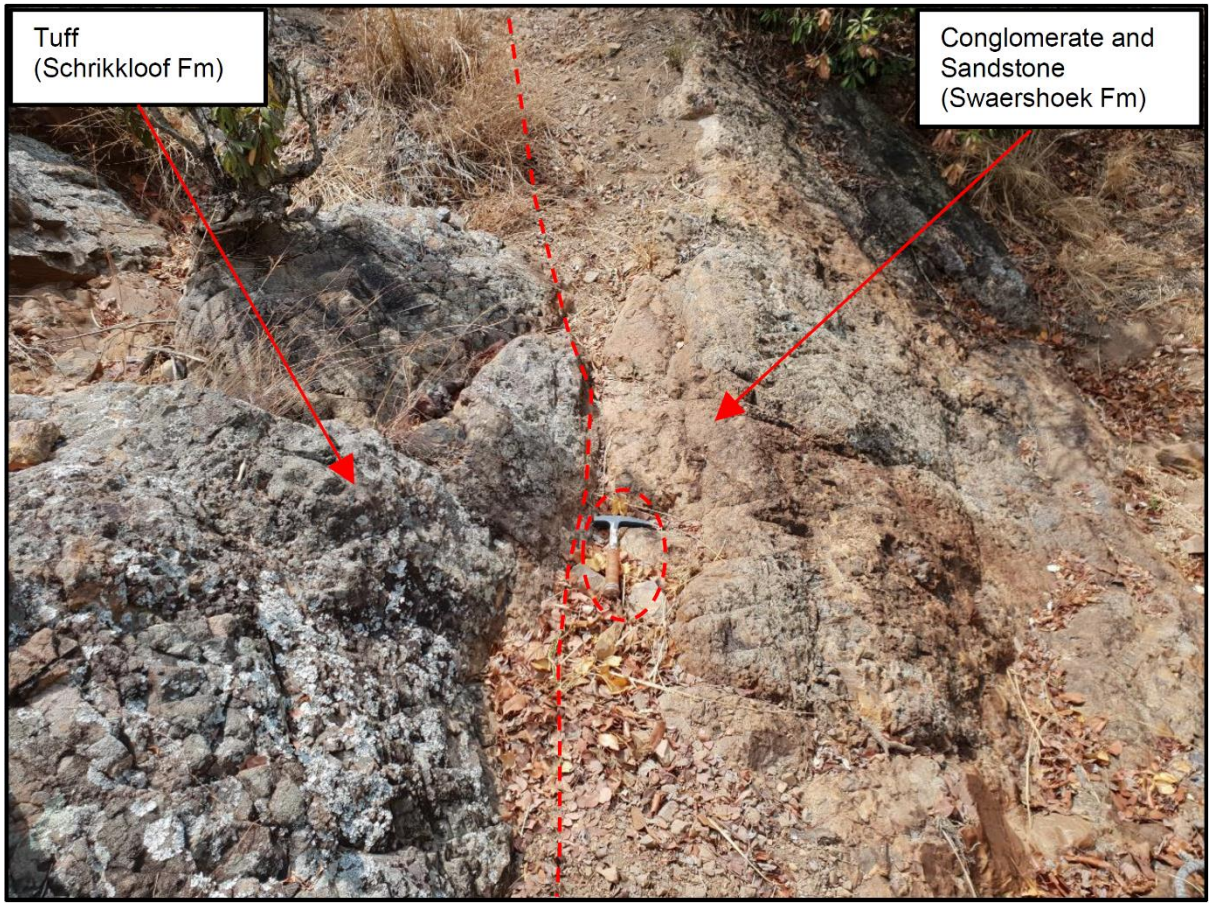

Figure 4.7: Contact between the tuff of the Schrikkloof Formation (left) and conglomerate basal conglomerate of the Swaershoek Formation (right). The geological hammer in the centre of the image is used as a scale.

The contact between the Rooiberg Group and Waterberg Group possibly marks the Rhyacian-Orosirian boundary in the international geological time scale at 2050 Ma (Cohen et al., 2013). This boundary also coincides with the end of the Rooiberg Group volcanism and the onset of deposition of clastic sedimentary rocks of the Waterberg

Group (conglomerates, sandstones and mudrocks). A detailed geochronological study is required to constrain this boundary.

4.4 Lithology (hand specimen)

A closer look at hand specimen samples provides a better insight on textures and mineralogy of rocks. A fundamental understanding of mineralogy and textures provides useful information as well as interpretation on inferring the source, origin and tectonic history of rocks. This section focuses on significant textures, hydrothermal alterations and mineralogy of rhyolites, tuffs and brecciated tuffs of the upper Schrikkloof Formation. There is reference to the sandstones and conglomerates of the Swaershoek Formation as this is part of the study area, however, the objective of this thesis focuses on the volcanic rocks of the Schrikkloof Formation.

4.4.1 Rhyolites

A hand specimen of rhyolites (Sample 26; Figure 4.8) shows a melanocratic, dark grey to black in colour on the fresh surface, with fine grained (aphanitic) texture. This fine grained texture indicates that the rock crystallised from quenching (rapid cooling) of lava in a subaerial environment. The rhyolites are also relatively undeformed and unaltered by heat, pressure as well as fluids after their crystallisation.

Figure 4.8: A fresh surface of greyish to black aphanitic melanocratic rhyolite of the Schrikkloof Formation composed of K-feldspar phenocrysts and quartz groundmass.

4.4.2 Tuffs

Hand specimens of tuffs show aphanitic texture with varying colour, from leucocratic to melanocratic and angular clasts from less than 2 to 20 mm (Figure 4.9). These tuffs appear to be relatively unaltered (Figure 4.9b, c and d), although there are patches of hematitisation (Figure 4.9a) which are proximal to the hydrothermal breccias. Minor patches of silicification are not uncommon and are typically disseminated.

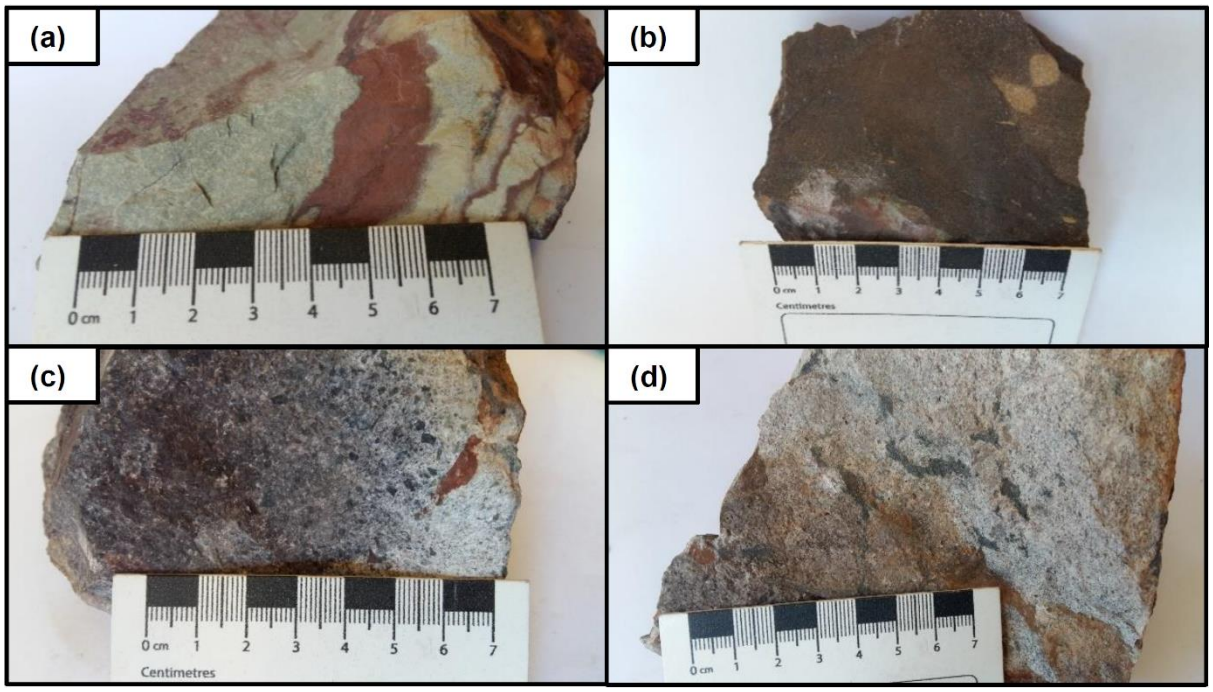

Figure 4.9: Schrikkloof Formation - (a) Fine grained hematitised tuff; (b) Tuff with quartz xenoliths with a 10 mm diameter; (c) Tuff with angular clasts of approximately 2 mm diameter. (d) Leucocratic tuff.

4.4.3 Hydrothermal breccias

The hydrothermal breccias (Figure 4.10) are characterised by crackle to chaotic textures; both matrix and clasts are fine grained. Crackle breccias in Figure 4.10 a, b and c commonly have >75% of leucocratic clasts with a >5mm diameter. The clasts are light coloured, and in some areas they comprise mainly quartz with iron staining. This suggests that tuffs were the primary rocks which were brecciated by fluids. Furthermore, crackle breccias have less than 25% of reddish brown to black veins comprising predominantly of Fe, hosted in hematite. The breccia reddish Fe-veins commonly have a thickness that ranges from <1mm to 20mm. Thin veins (<1mm) in the area are mostly associated with crackle breccias (Figure 4.10b) whereas thick veins (~20mm) are more common in chaotic hydrothermal breccias (Figure 4.10). The mineralogical composition of these Fe-rich veins is predominantly hematite.

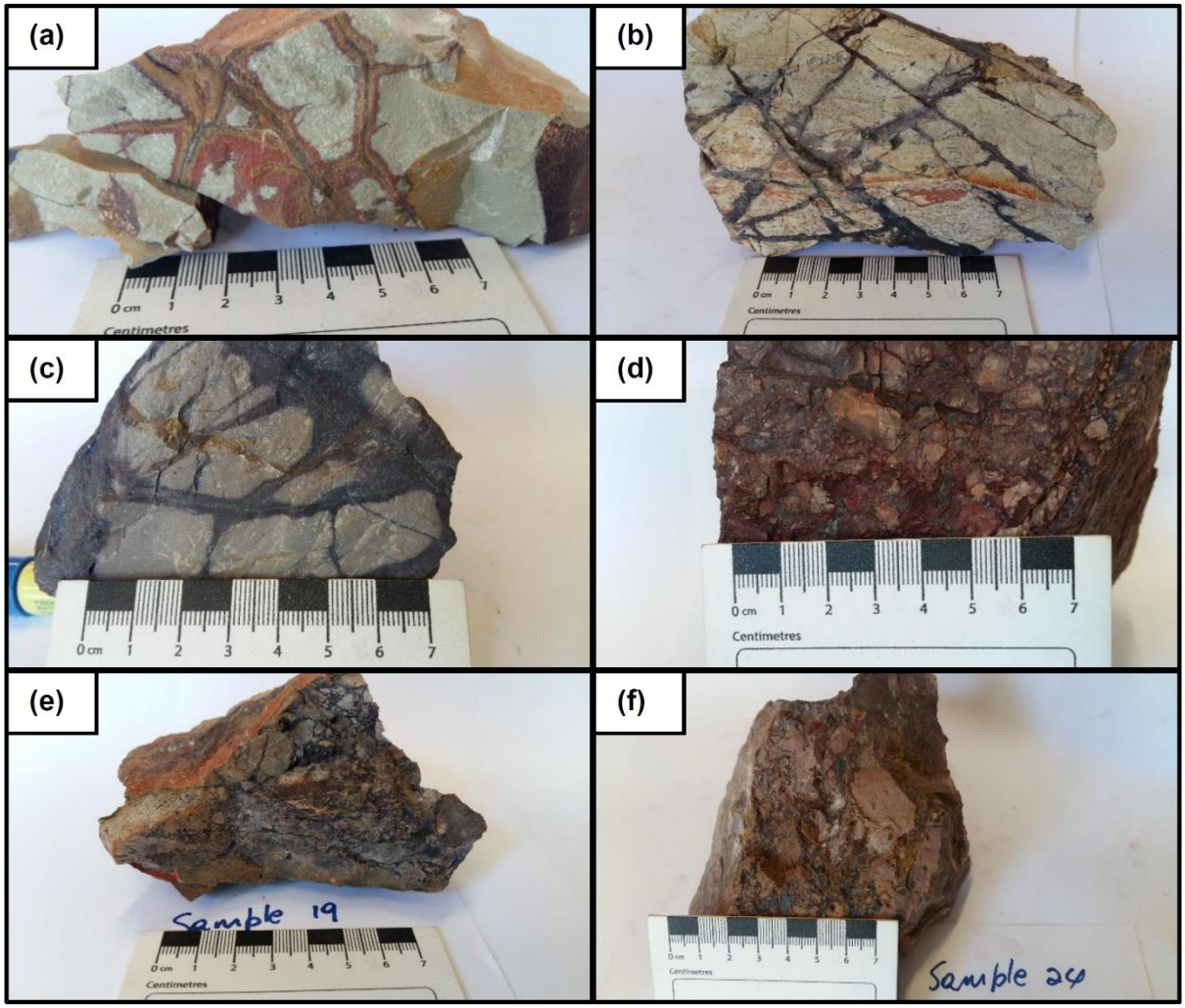

Figure 4.10:Schikkloof Formation - (a, b & c) Hydrothermal crackle breccias with a >5mm clasts size and a matrix. These breccias generally have than 75% large clasts. (d, e & f) Hydrothermal mosaic to chaotic breccias where clasts have been partially or completely rotated. Roughly 50 to 65% of these rocks are made of clasts and the other 35 to 50% is the matrix.

4.5 Petrography

4.5.1 Rhyolites

Under the microscope, rhyolites exhibit sparsely micro-porphyritic texture with approximately 2000µm (2mm) K-feldspar phenocrysts in a fine grained groundmass (Figure 4.11 and 4.12). The K-feldspar phenocrysts are elongated, sericitised, euhedral and show simple twinning.

The phenocrysts are light coloured with no pleochroism in plain polarised light (PPL) under transmitted light microscopy (Figure 4.11a and 4.12b). This texture is very common in both altered and unaltered K-feldspar. There appears to be hematitisation associated with sericitised K-feldspar phenocrysts (Figure 4.11).

The hematitisation is interpreted to have occurred within the wear abrasion stage (as explained on stage 2 in section 1.3) with other minor processes such as volume expansion, corrosive wear and development of fluid-assisted brecciation.

The mineralogical paragenetic sequence is marked by initial growth of euhedral K-feldspar grains in the magma, followed rapid quenching during eruption of the lava. Rapid cooling promotes nucleation and prohibits crystal growth, accentuating the development of a porphyritic texture (Winter, 2014), which is common in subaerial volcanic environments. Sericitisation appears to have followed after solidification of rhyolites and subsequently hematitisation by Fe-rich fluids (Figure 4.11).

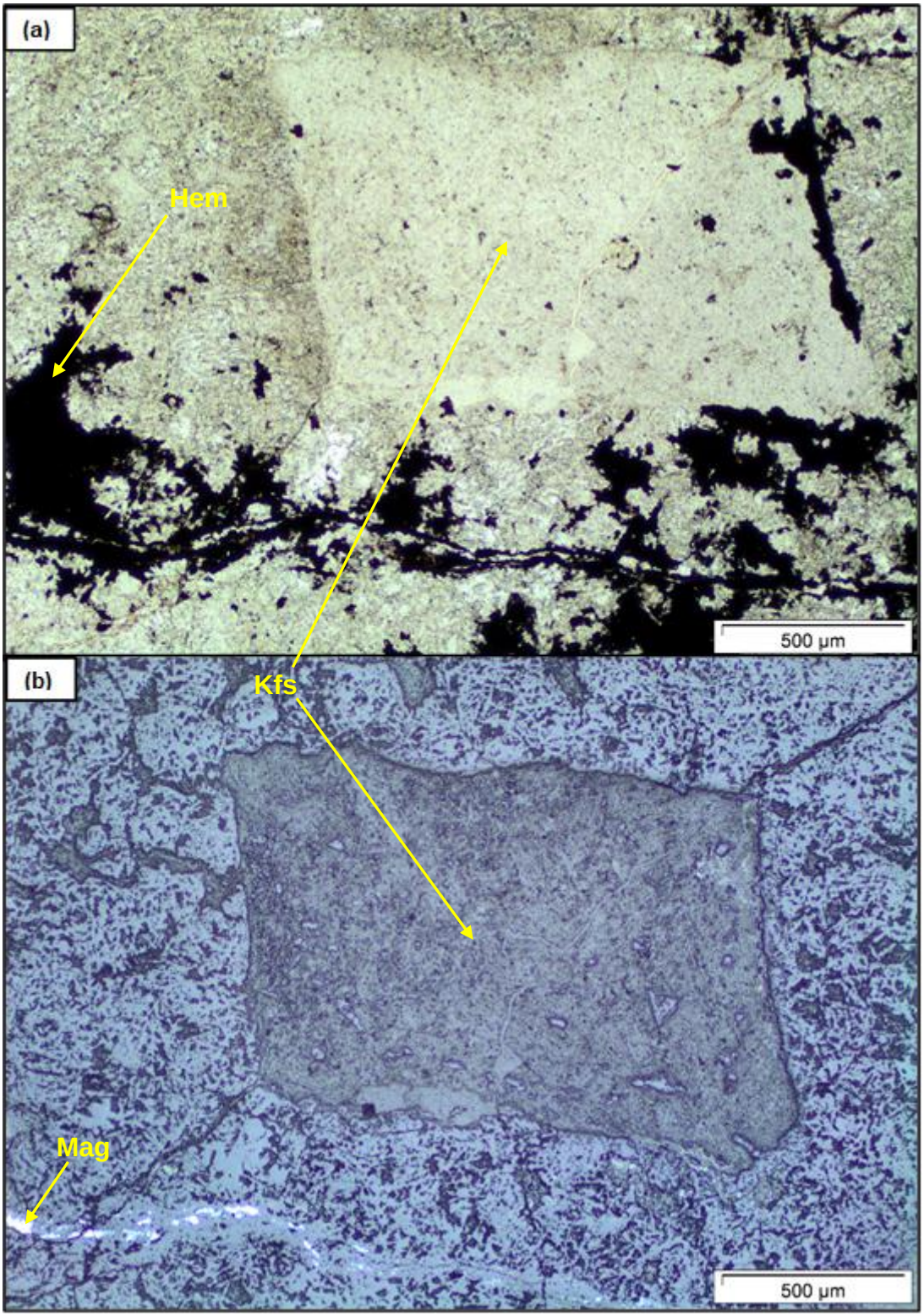

Figure 4.11: (a) Photomicrograph of a porphyritic rhyolite (sample 07) with a euhedral sericitised and hematitised K-feldspar grain under plain polarised light (PPL) in transmitted light(b) the same rock in reflected light shows magnetite (Mag) and hematite (Hem) associated with hematitisation.

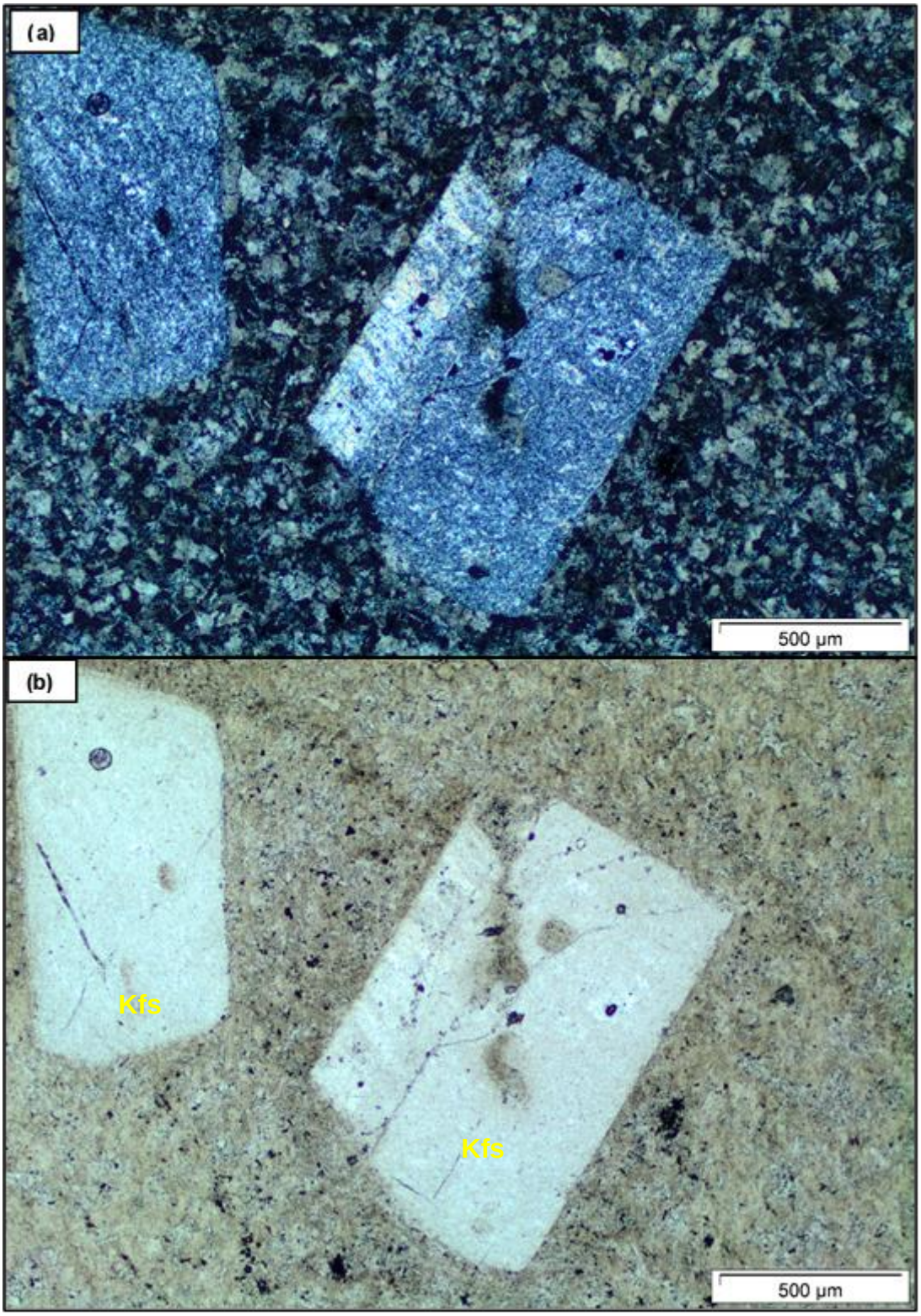

Figure 4.12: A least altered rhyolite in sample 25 under (a) cross polarised light (XPL) and (b) plane polarised light (PPL) showing sericitised K-feldspar phenocrysts.

4.5.2 Tuffs

The primary texture of tuffs is cryptocrystalline to glassy (Figure 4.13 and 4.14) with relatively unaltered euhedral quartz phenocrysts, which are ~100µm in diameter (Figure 4.13b). The size and types of clasts classify these pyroclastic rocks as ash tuffs in terms of the Fisher (1966) classification, as there are approximately 75% clasts with <2mm diameter (Figure 4.13).

These tuffs are cut by secondary veins which mainly comprise of oxide minerals such as hematite and magnetite (Figure 4.13a). An alteration halo is common around these hematite and magnetite veins which are hosted within tuffs (Figure 4.13a and 4.14a). The process describing the formation of this texture was presented in section 1.3. It involves significant wear abrasion (stage 2) with considerable fluid propagation and minor fluid-assisted brecciation.

Fundamentally, this process occurs prior to the dilation stage, where there are interconnected network of fluids. Hydrous minerals (such as muscovite) seem to have replaced opaque minerals (Figure 4.14b and c). This process occurred after fluid-assisted brecciation and crucial to this study (as the geochemistry of preserved rocks might be affect by this late alteration).

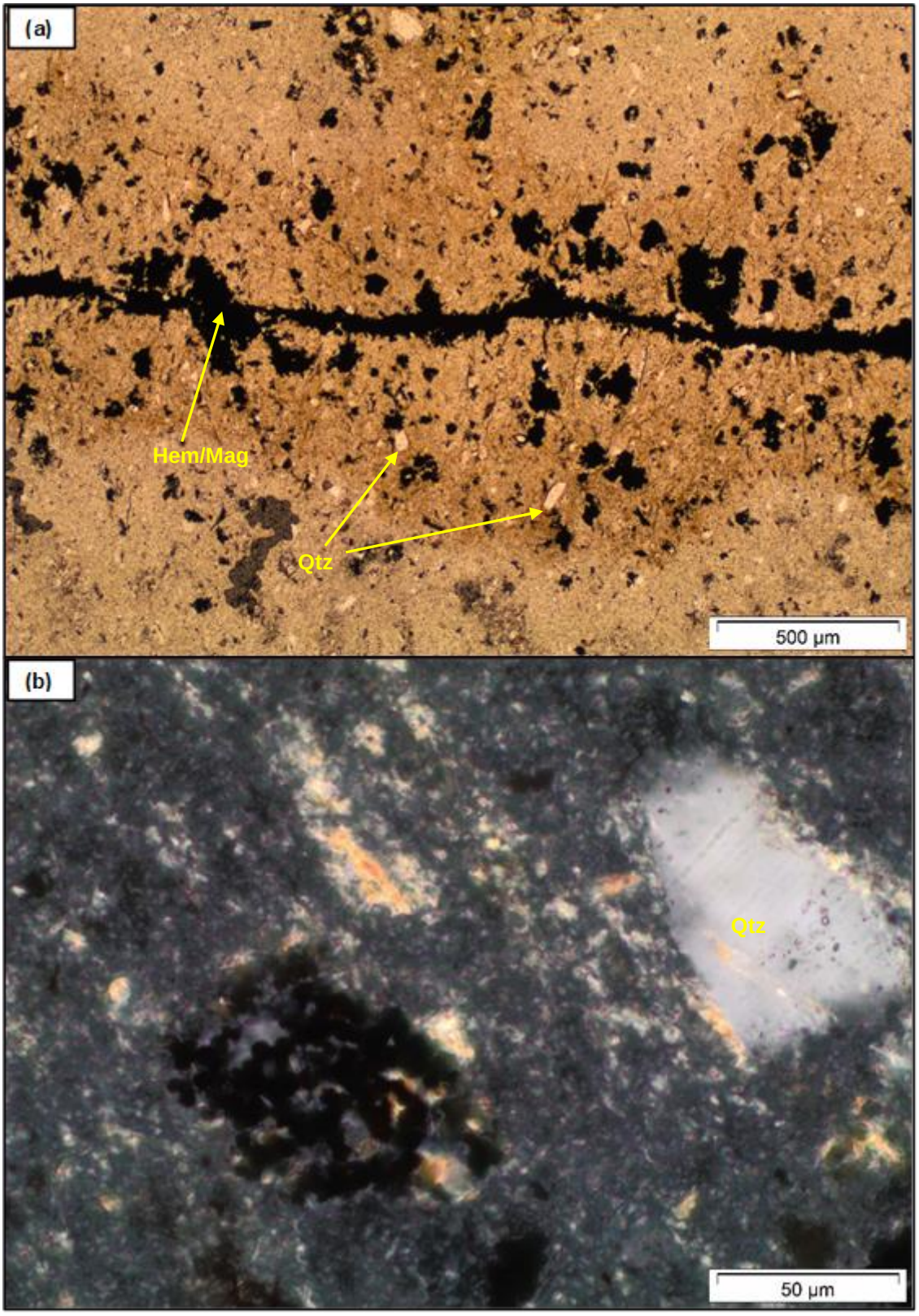

Figure 4.13: (a) A tuff with a quartz phenocrysts (<100µm) cut by a hematite (Hem) and magnetite (Mag) vein (PPL). (b) An angular quartz fragment under 40x magnification in XPL.

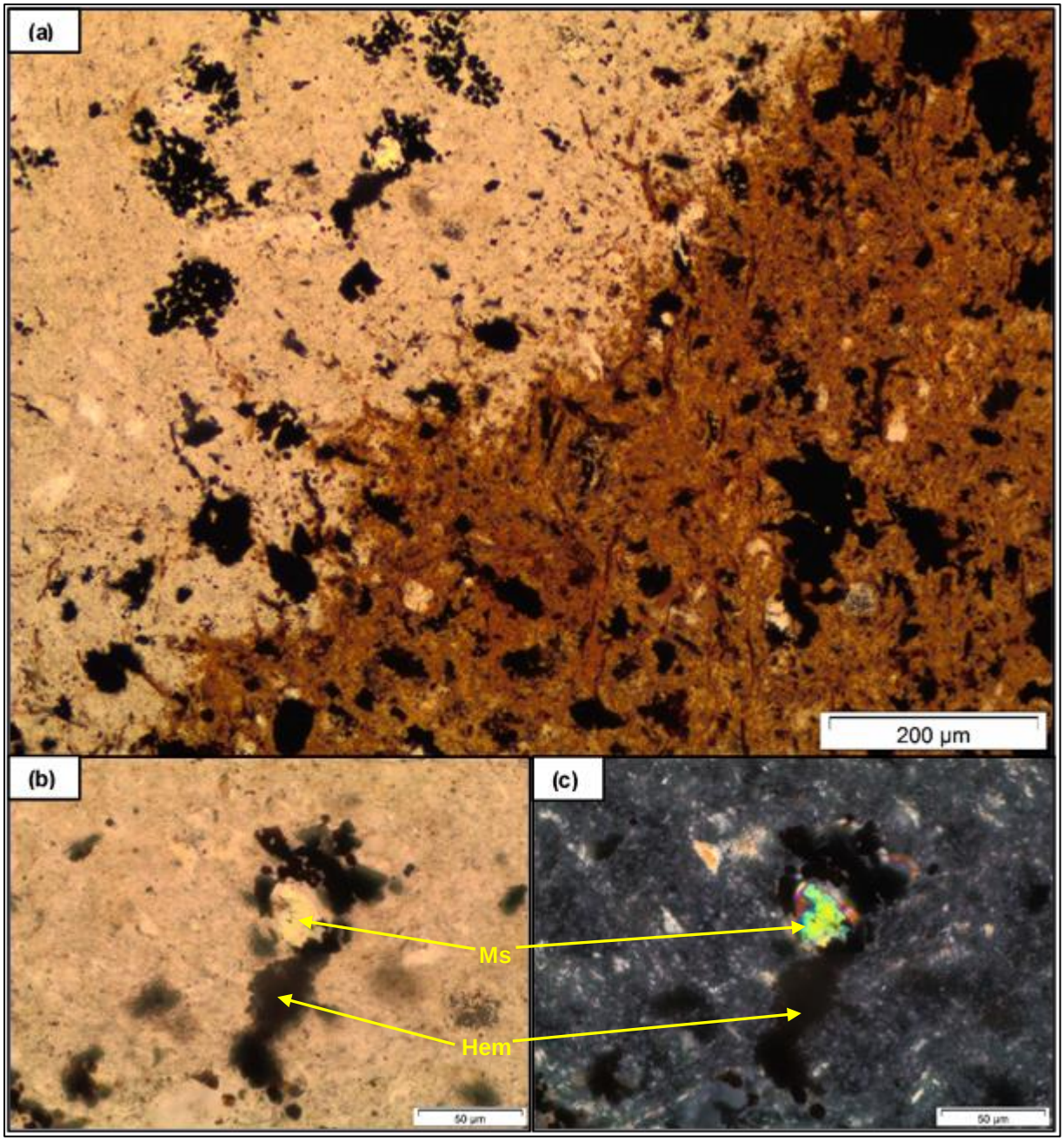

Figure 4.14: (a) Alteration halos commonly form around veins (as shown in Figure 4.13a). Replacement of hematite (Hem) by muscovite (Ms) under (b) PPL and (c) XPL.

4.5.3 Hydrothermal breccia

The chaotic, mosaic and crackle brecciation textures are not uncommon. Sample 19 had both chaotic and mosaic brecciation textures preserved (Figure 4.15a, b). This chaotic-mosaic breccia is composed of tuffaceous clasts cemented by hematite; the tuffaceous clasts commonly comprise quartz phenocrysts (Figure 4.15b). The clasts of the chaotic breccia are of various unequal sizes, commonly angular and considerably rotated (Figure 4.15a). The chaotic breccia appears to have formed by violent fluid brecciation, whereby the rock was fragmented into various clast sizes. This process explains the lack of alteration halos around clasts, and also the clast shapes. By contrast, the mosaic breccia has rounded edges and clasts of various sizes (Figure 4.15b), with minor rotation. There are minor alteration halos around clasts within mosaic breccias (Figure 4.15b).

A secondary silicification alteration process occurred after hematitisation, whereby hematite was replaced by quartz (Figure 4.16; Sample 09). The silicification appears to be associated with recrystallisation of quartz within the tuffaceous clasts (Figure 4.16b). The primary mosaic brecciation of this rock is preserved despite the secondary silicification. The secondary quartz might have been derived by leaching of the tuffaceous country rock. Another example of a hydrothermal breccia is shown in Figure 4.17 (Sample 15), where the rock shows a crackle breccia texture. The crackle breccia appears to have been oxidised and weathered (Figure 4.17) to form hematite veins and goethite alteration halos.

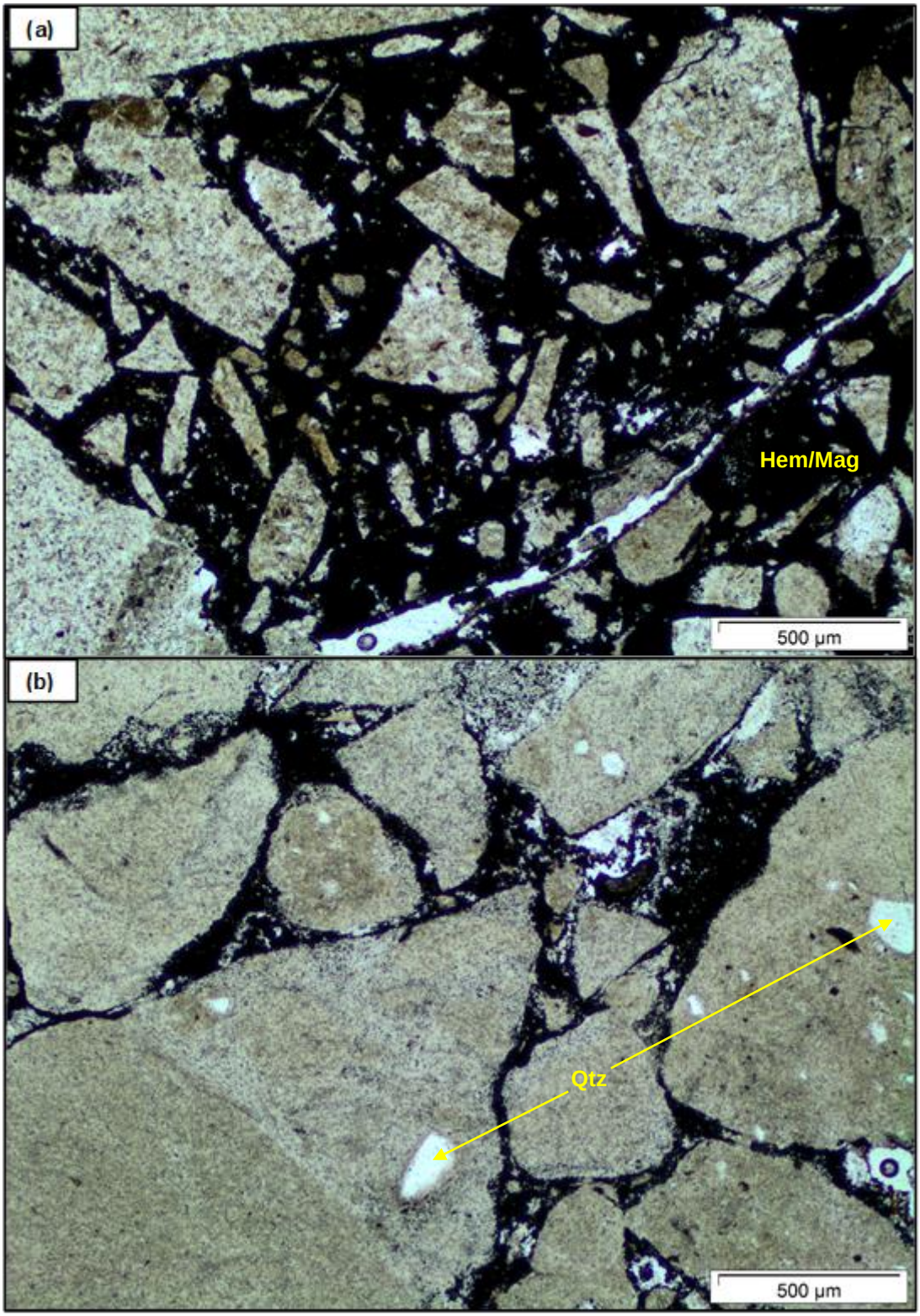

Figure 4.15: (a) A chaotic breccia where angular tuffaceous clasts are cemented by what appears to be opaque hematite/magnetite interstitial fluids. (b) A mosaic breccia where the clasts are composed tuffs with quartz phenocrysts in a glassy groundmass.

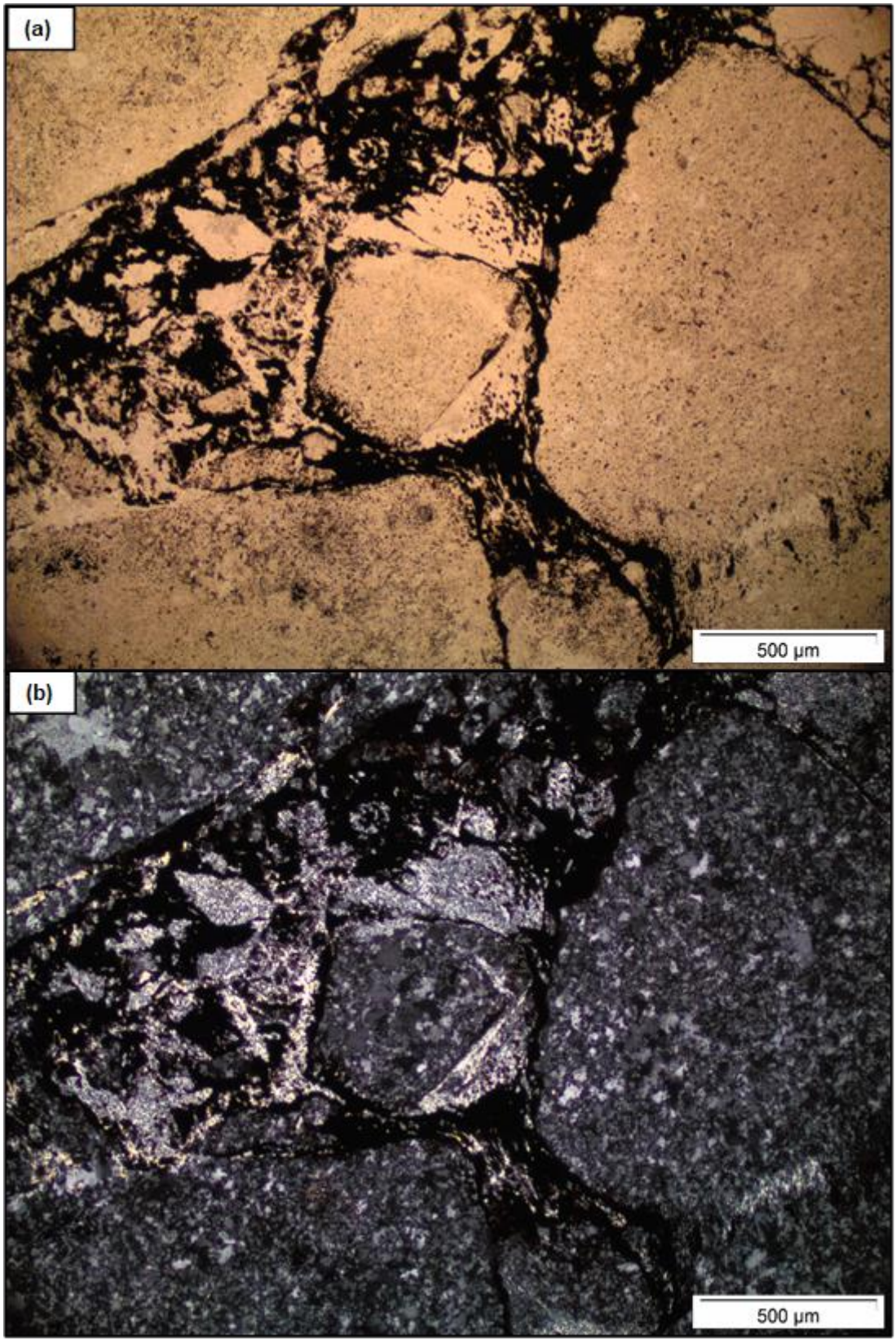

Figure 4.16: A mosaic breccia with siliceous clasts cemented by opaque hematite/magnetite veins under (a) PPL and (b) XPL.

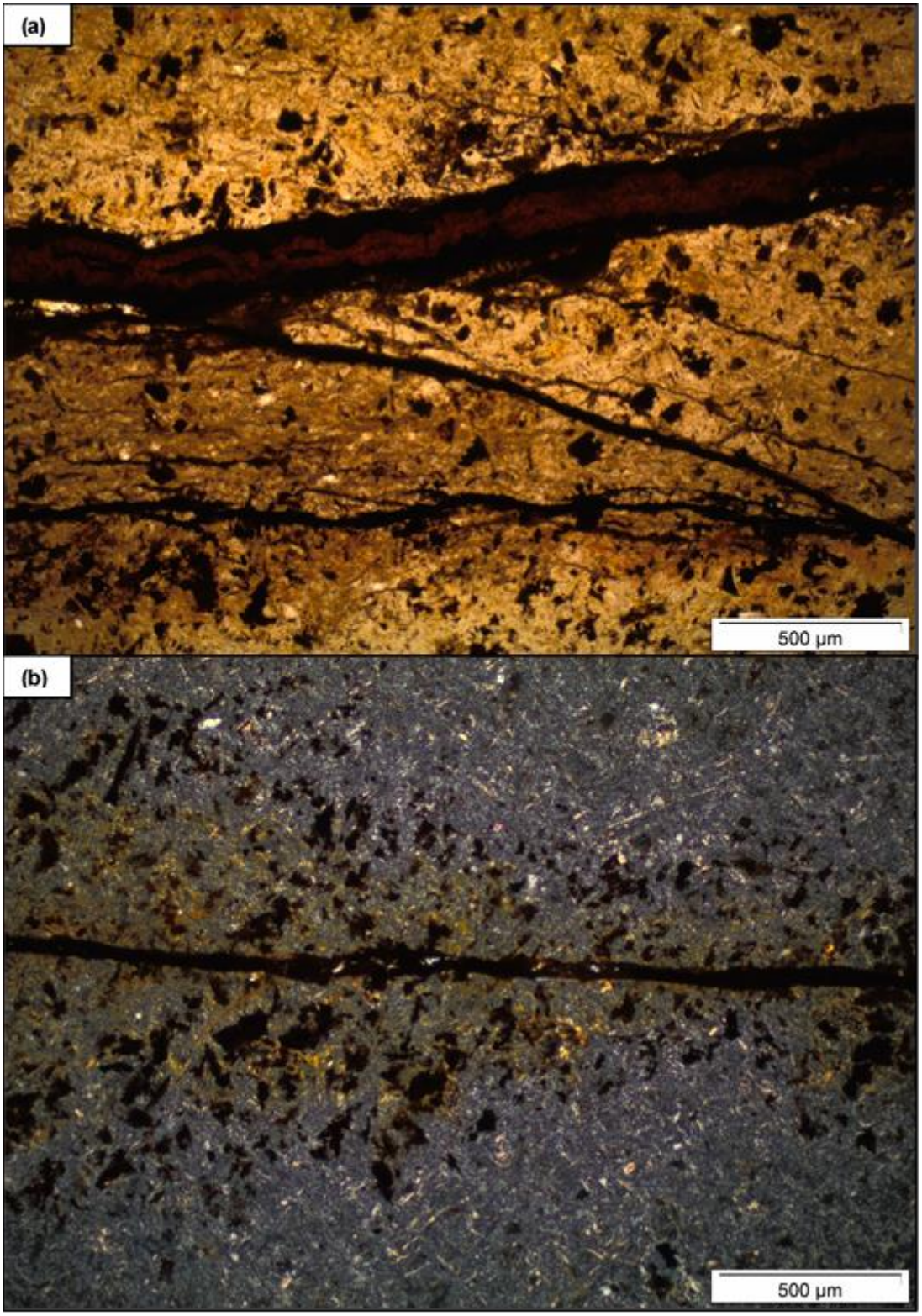

Figure 4.17: (a) Interconnected veins forming a crackle breccia texture under PPL. These veins appear to be oxidised from magnetite or hematite to form goethite. (b) A hematite vein with a goethite halo under XPL.

5 Mineralogy and whole rock geochemistry

5.1 SEM-EDX analysis

The SEM-EDX technique was adopted to analyse a hydrothermal breccia (Sample 19) and a hematitised tuff (Sample 36), in order to identify the composition of veins and clasts within the system. Only two rocks (mounted on polished thin sections and carbon-coated) were analysed because of budget constraints. Sample 19 shows a chaotic to mosaic brecciation texture (as indicated above in Figure 4.15), whereas Sample 36 (a hematitised tuff) was particularly selected for SEM-EDX analysis because of a high Pb content of 1665.8 ppm (~0.17 wt.%), which suggests the presence of Pb minerals, see Table A3.3 in Appendix 3. The SEM-EDX spot analysis of each spectrum in the backscattered electron (BSE) images below are reported in Appendix 2, including peaks and relative mineralogical composition. The chemical formula of each mineral was deduced by comparing peaks and the relative atomic concentration of elements (reported on each SEM-EDX diagram on Appendix 2).

5.1.1 Sample 19 SEM-EDX analysis

The BSE images of Sample 19 (Figure 5.1) indicate that this hydrothermal breccia is composed mainly of quartz (SiO_2), hematite (Fe_2O_3) and minor anglesite ($PbSO_4$). Anglesite is commonly less than 250 µm in size with a anhedral or interstitial shape, hosted within hematite veins (Figure 5.1 – 5.4); the modal abundance of this Pb bearing mineral is less than 1%. This SEM-EDX analysis augments that observations both in hand specimen and petrography (Fe-rich veins and cross cutting Si-rich country rock) are precise.

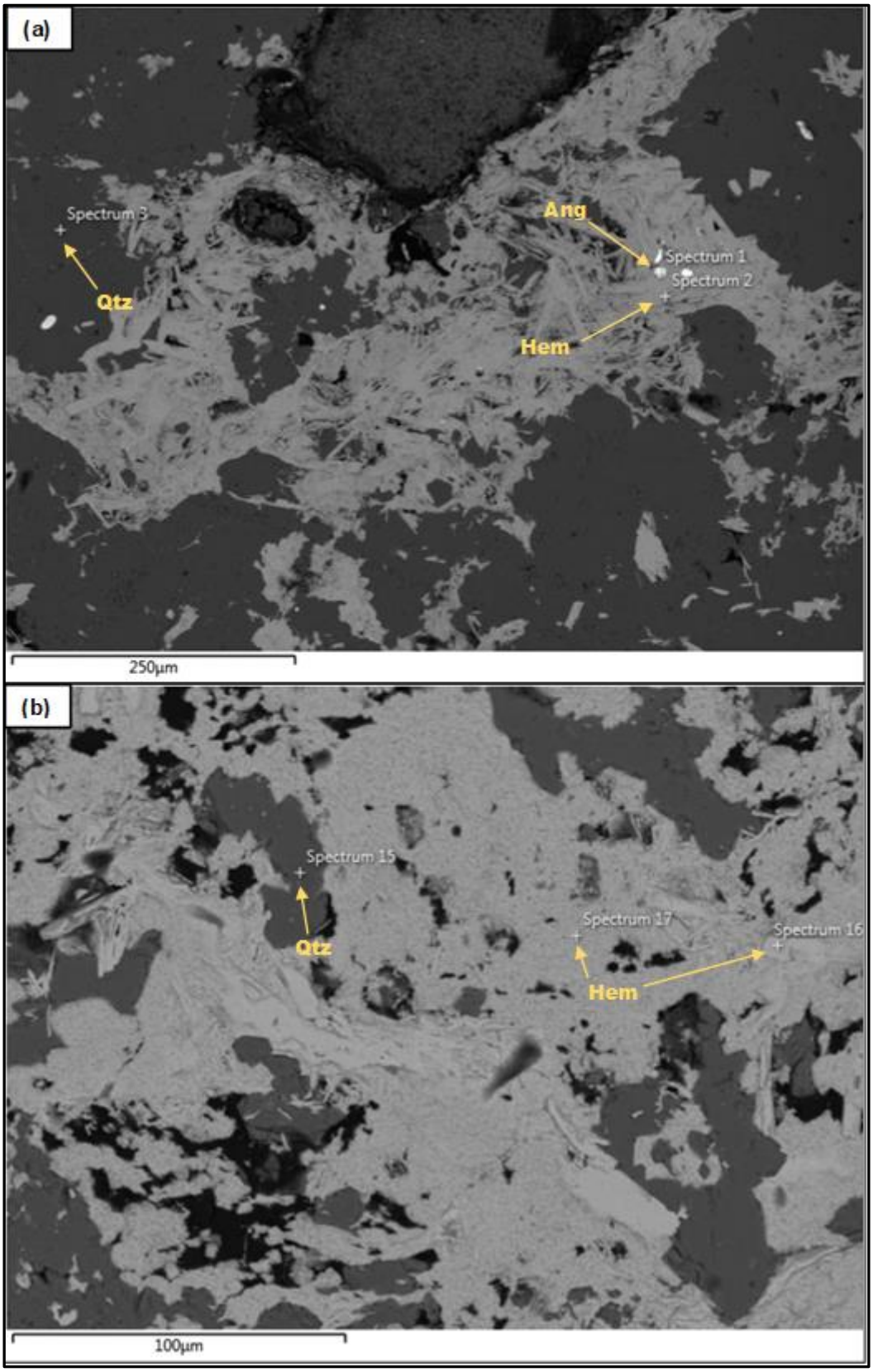

Figure 5.1: BSE images of a hydrothermal breccia from Sample 19. (a) Shows quartz (Qtz), hematite (Hem) and minor anglesite (Ang) mineralogy. (b) Indicates quartz (Qtz) and hematite (Hem) mineralogy. SEM-EDX spectrums are reported in Appendix 2.

This Si-rich tuffaceous host rock appears to be barren of sulphide minerals such as galena. It is evident that ore forming minerals (i.e. anglesite and other related sulphides) are not abundant within hydrothermal breccias. The uncommon occurrence of ore forming minerals possibly indicates that the conditions for trapping or precipitating metals were not suitable, alternatively the fluids were depleted in metals. As such, these hydrothermal breccias indicate fluid pathways for ore forming minerals in the system and not their trap.

5.1.2 Sample 36 SEM-EDX analysis

The BSE images (Figure 5.2, 5.3 and 5.4) illustrate the composition of the host rock, and clarify the fluid composition and their associated ore minerals. The host rock is predominantly composed of crystalline quartz and K-feldspar ($KAlSi_3O_8$). The tuffaceous country rock appears to be composed of Si, K as well as Al and is crosscut by an interconnected network of Fe-rich veins, which form interstitial hematite and chlorite ($(Fe_5Al)(Si_3,Al)O_{10}(OH)_8$). This alteration style is commonly referred to as hematitisation and is associated with oxidizing fluids reacting with reduced country rock or mix reduced fluids (Robb, 2005).

Hematite veins are commonly associated with anglesite. Furthermore, anglesite is commonly formed by oxidation of galena (PbS) in supergene environments and is abundant in oxidised portions of lead deposits or mineralisation (Klein and Dutrow, 2007). Anglesite can also form by dissolution of lead sulphides (such as galena) and subsequent precipitation as well as recrystallisation under suitable conditions (Klein and Dutrow, 2007; Sergeev et al, 2017; Verhaert et al., 2017; Liu et al., 2022). There were no relict cores of galena observed, suggesting that the supergene alteration possibly ran to completion.

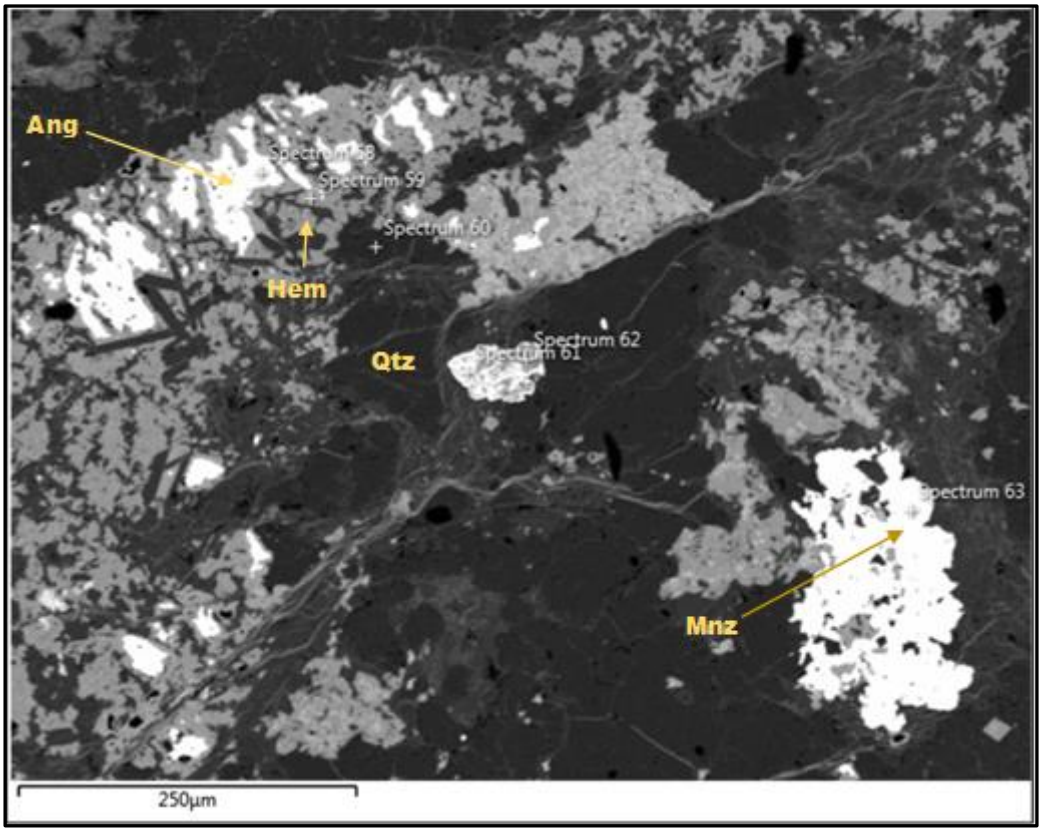

Figure 5.2: Sample 36; A BSE image showing quartz (Qtz), hematite (Hem), anglesite (Ang) and monazite (Mnz). The network of hematite veins appears to be associated with both anglesite and monazite. SEM-EDX spectrums are reported in Appendix 2.

Chlorite possibly formed at low temperatures (Figure 5.3b) by a fluid-rock reaction between Fe-rich oxidizing fluids and Si-K rich host rock to form an interconnected network of veins. REE-bearing minerals such as monazite are associated with this chloritisation (Figure 5.2 and Figure 5.3b) and suggest the existence of Th and REE-bearing fluids. Monazite appears to be a common mineral in this hydrothermal system and this suggests that REE enrichment is possible.

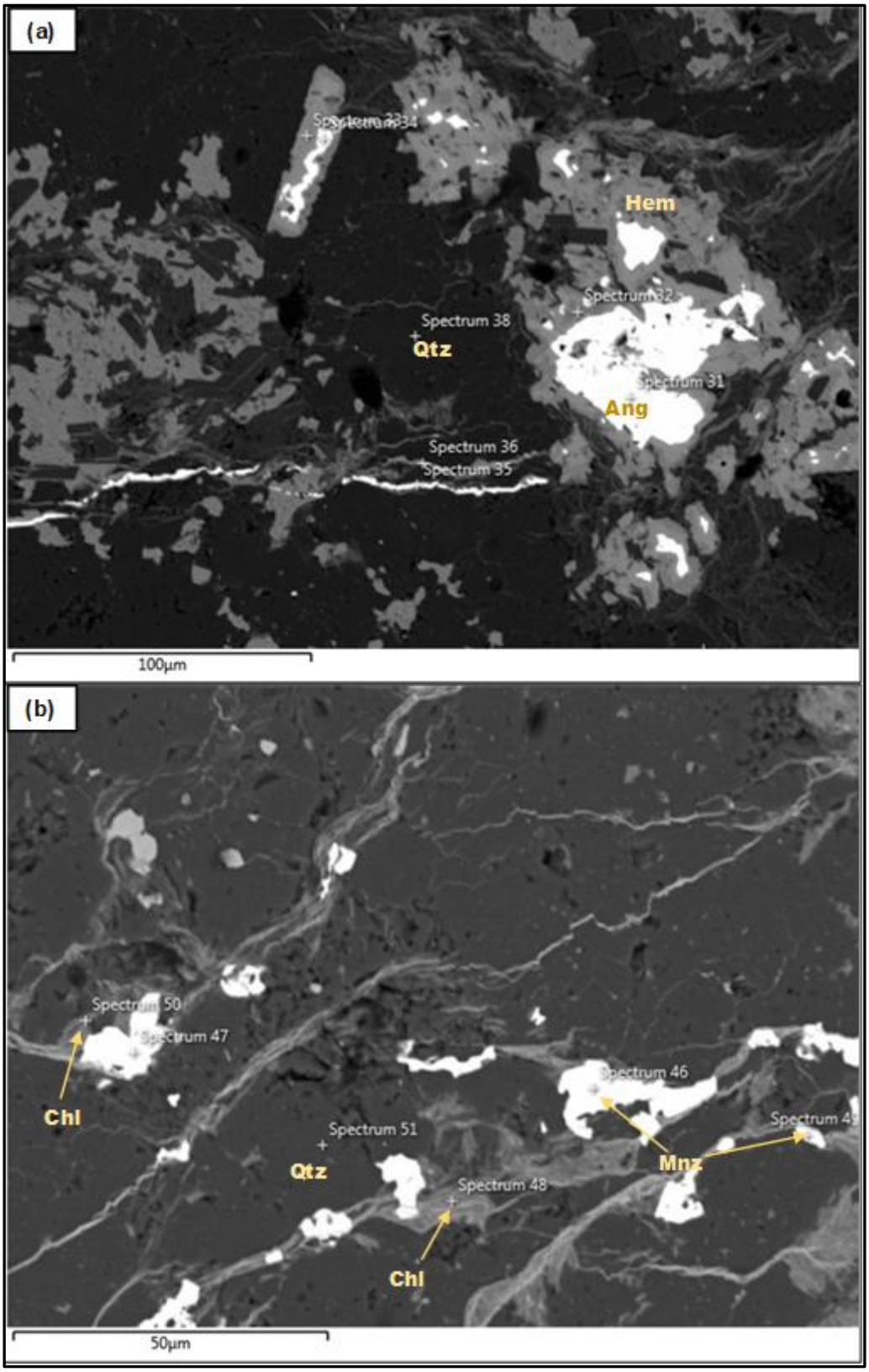

Figure 5.3: Sample 36; (a) A BSE image showing hematite (Hem) associated with anglesite (Ang). (b) A BSE image showing chlorite (Chl) associated with monazite (Mnz). Chlorite could have possibly formed by Fe-fluids reacting with the quartz rich matrix at low temperatures. SEM-EDX spectrums are reported in Appendix 2.

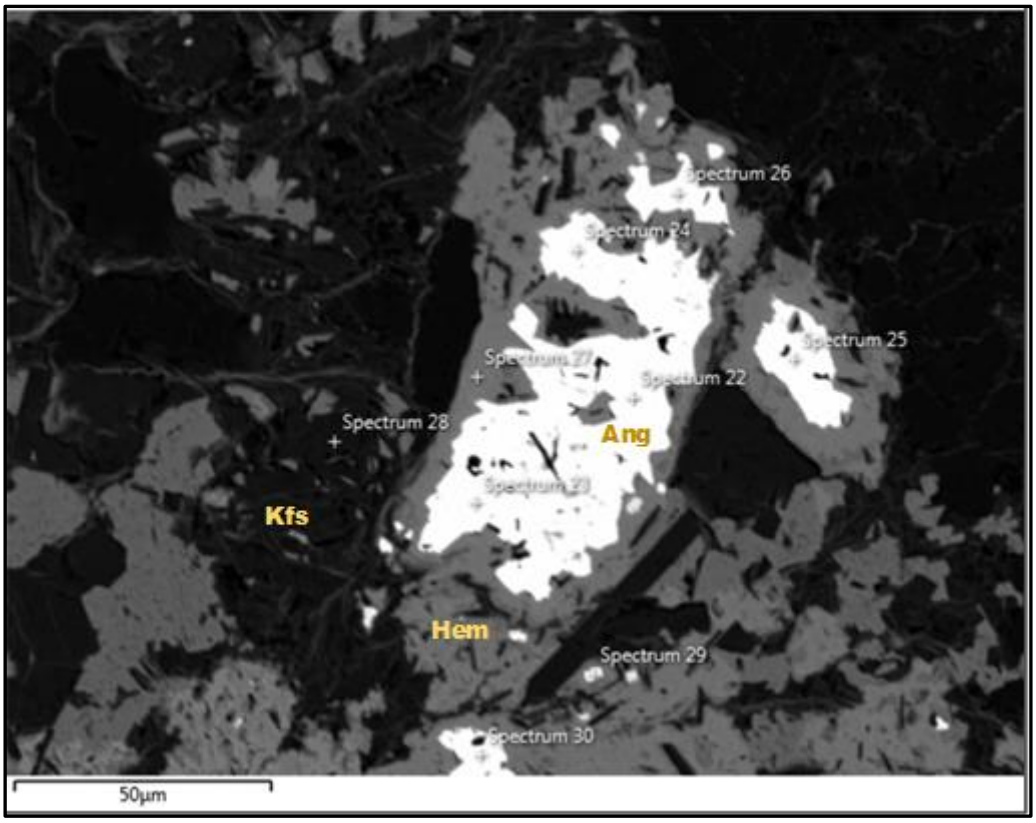

Figure 5.4: Sample 36; A BSE image showing anglesite associated with hematite. SEM-EDX spectrums are reported in Appendix 2.

5.2 Whole rock geochemistry

The XRF, ICP-MS and ICP-OES geochemical results for both major and trace elements are reported in Appendix 3 (Table A3.1 – A3.5). The geochemical results in Appendix 3 refer to rhyolites (Table A3.1), tuffs (Table A3.2 and A3.3) and hydrothermal breccias (Table A3.4 and A3.5). There is a unique rock in Table A3.5 Appendix 3 which indicates the composition of veins; Sample 08. This particular rock (Sample 08) is a grab sample from collected in the field that contains 87.4 wt.% Fe_2O_3, 114 ppm Pb, 113 ppm Sb, and 286 ppm W. This composition characterises the reddish veins cutting across rhyolites and tuffs as well as their potential base metal contents.

5.2.1 Geochemical classification and tectonic setting

The classification scheme by Winchester and Floyd (1977) uses relatively immobile elements (Zr/TiO_2 vs Nb/Y) hence it is suitable for hydrothermally altered rocks as opposed to the TAS (Total Alkalis vs Silica) classification scheme. The Winchester and Floyd (1977) geochemical discrimination diagram (Figure 5.5) was therefore adopted to classify the various volcanic rocks within the study area.

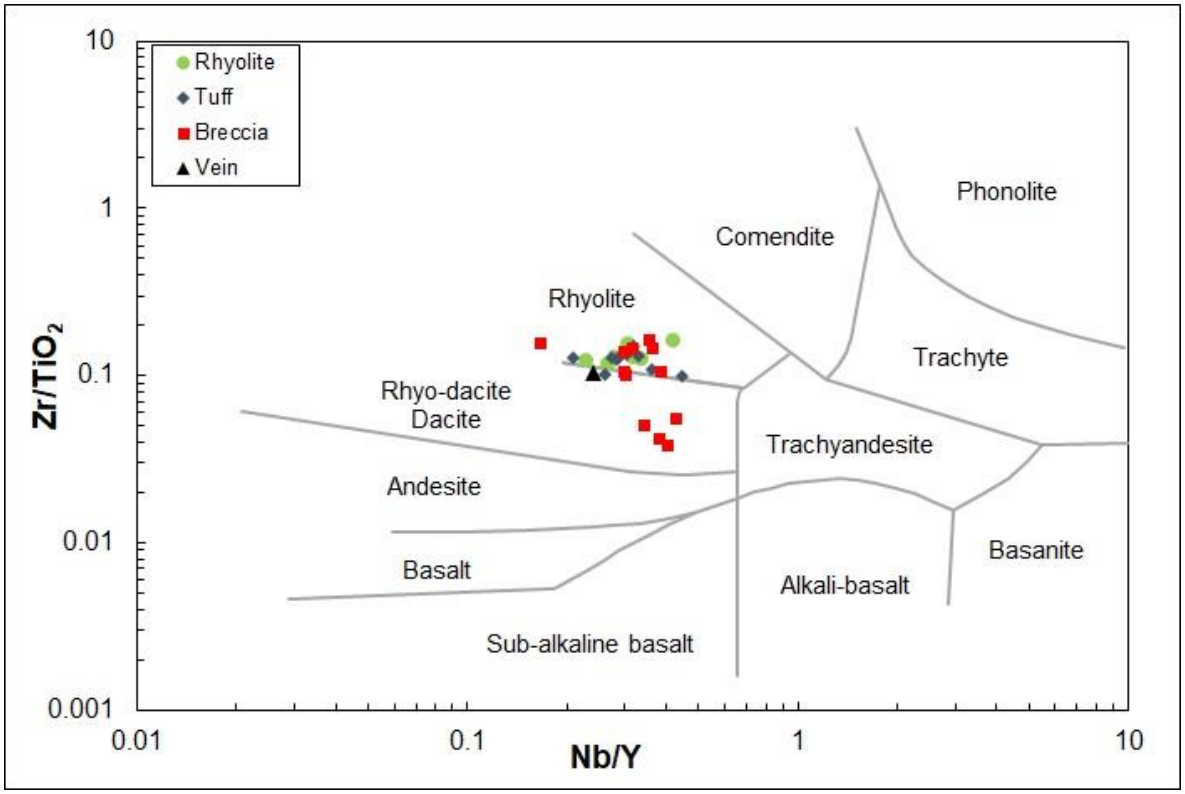

Figure 5.5: Geochemical classification of rhyolites, tuffs and breccias from the study area. Tuffs have a rhyolitic composition whereas breccias have a rhyolitic to dacitic composition. This classification was adopted from Winchester and Floyd (1977).

Figure 5.5 indicates that the field observations and descriptions above (section 4.1 and 4.4) of rhyolites are accurate. Furthermore, tuffs appear to have a similar composition to rhyolites and breccias have a rhyolitic to dacitic composition. The dacitic composition may be a result of hydrothermal alteration with silica removal from the system and iron enrichment (as indicated by BSE images above).

The tectonic setting discrimination diagram Rb vs Nb+Y (Pearce et al., 1984) in Figure 5.6 suggests that rhyolites and tuffs were deposited in a within-plate setting. There is small number of rock samples (predominantly hydrothermal breccias) plotting within the volcanic arc setting and this might be due to alteration.

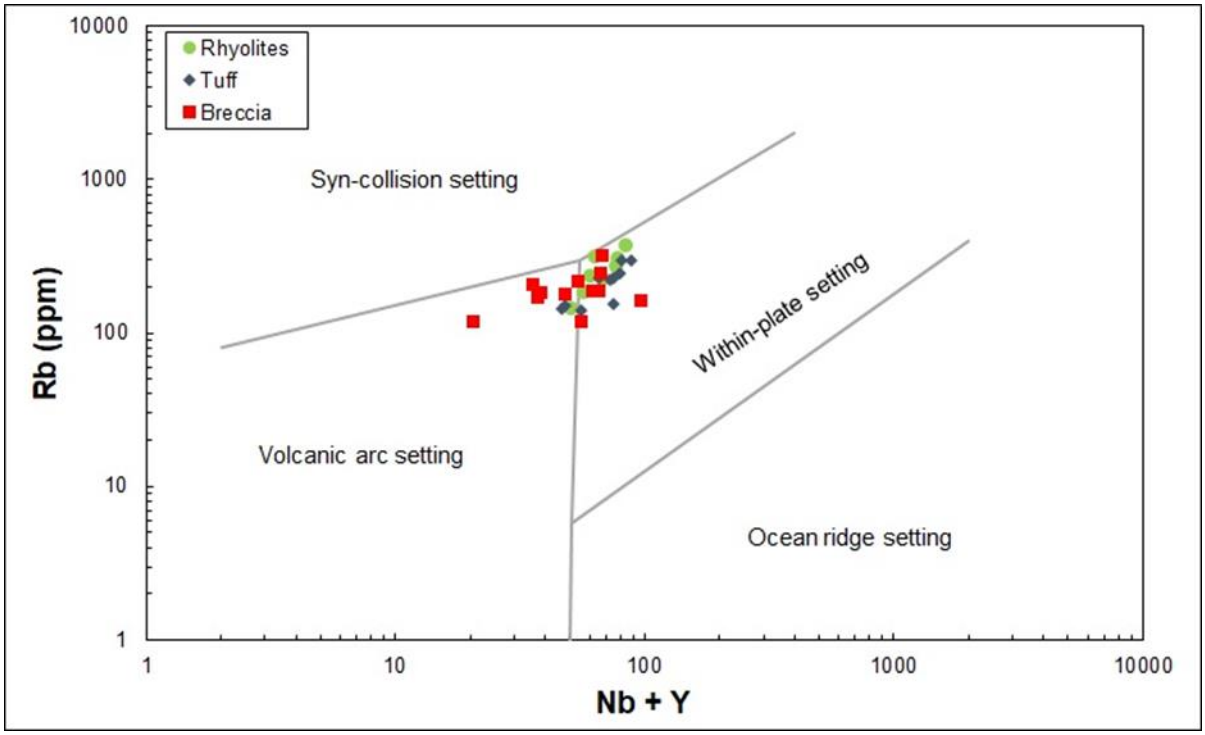

Figure 5.6: Discrimination diagram which suggests a within-plate tectonic setting for the analysed samples. The overlap of hydrothermal breccias into the volcanic arc setting is because of hematitisation alteration. Adopted from Pearce et al., (1984).

5.2.2 Major elements

The bivariate Harker plots are plotted below in Figure 5.7 include TiO_2, Al_2O_3, Fe_2O_3 and K_2O. There is scatter around these smooth trends which is possibly due to variable degrees of alteration. These smooth trends of the above-mentioned major elements suggest that rhyolites, tuffs and breccias are genetically related.

This co-genetic relationship, however, does not disclose the nature, composition and source of hydrothermal fluids within these volcanic rocks. From the diagrams it also noticeable that the TiO_2 content (indicated on Figure 5.7a) does not change with SiO2

and is less than 1 wt.%, common for felsic rocks such rhyolites and granites. Other major elements, including Al_2O_3, Fe_2O_3 and K_2O, (Figure 5.7b – d) show negative trends.

For the same SiO_2 content, breccias (Figure 5.7b and c) appear to be relatively depleted in Al_2O_3 and enriched in Fe_2O_3. This can be attributed to alteration whereby aluminium bearing minerals such as biotite are altered to chlorite, hence causing the dilution of Al_2O_3 in the system. The enrichment of Fe_2O_3 supports the introduction of Fe into the system by hydrothermal fluids and this is also augmented by petrography and SEM-EDX analysis (section 4.5 and 5.1 above).

There are two low-SiO_2 tuff samples (Figure 5.7) which have less than 65 wt.% SiO_2 and these rocks could be dacitic in composition as suggested by the geochemical classification scheme above in Figure 5.5.

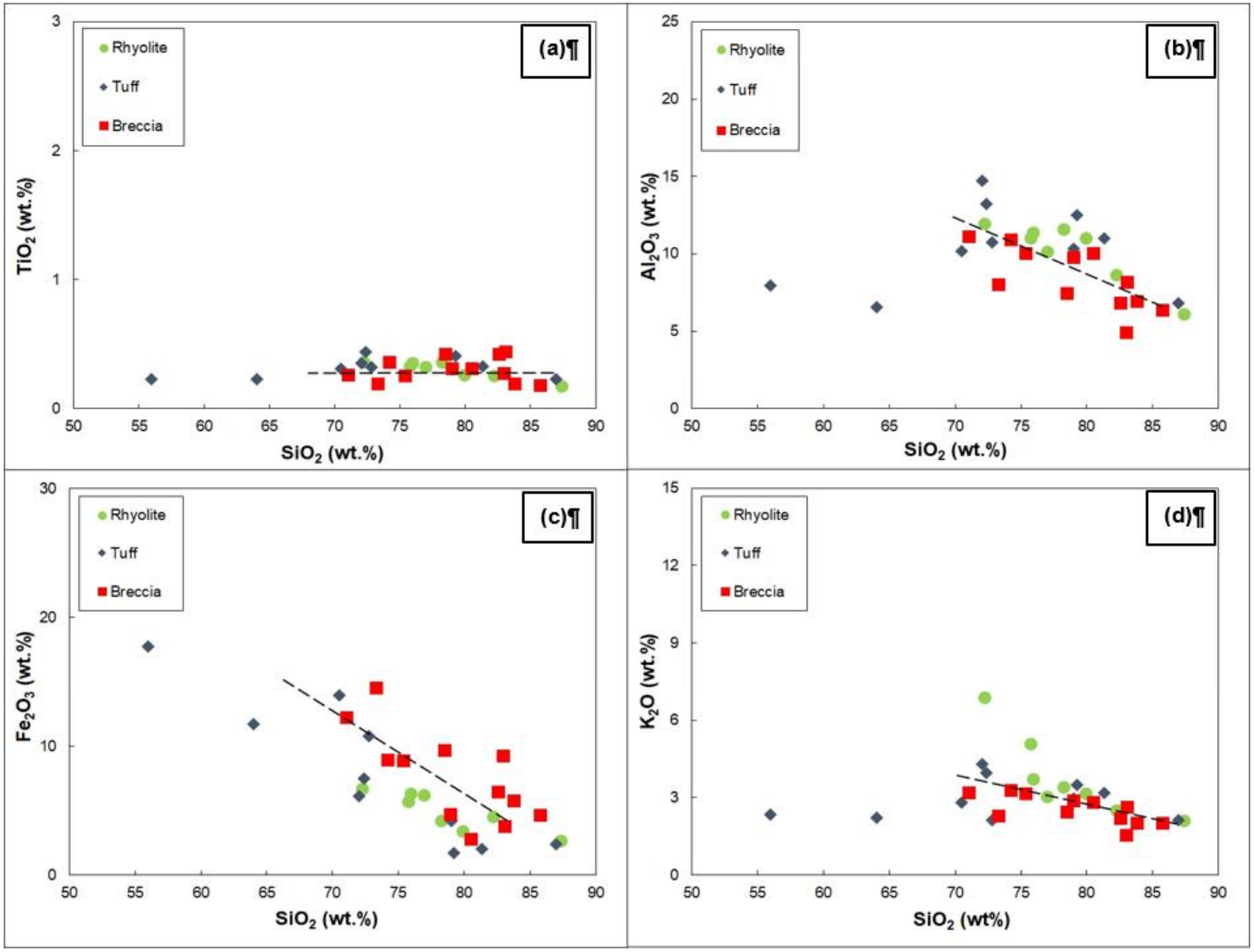

Figure 5.7: Bivariate Harker diagrams of (a) TiO_2, (b) Al_2O3, (c) Fe_2O_3 and (d) K_2O. Silica appears to have generally negative correlations to the major elements, except TiO_2.

Fe_2O_3/K_2O and TiO_2/K_2O ratios (Figure 5.8a, b) are plotted against K_2O (wt.%). The diagrams highlight fractionation and hematitisation trends. Fractionation in rhyolites gives a relatively horizontal trend at increasing K values, whereas, hematitisation produces steep vertical trend towards higher Fe_2O_3/K_2O and TiO_2/K_2O ratios.

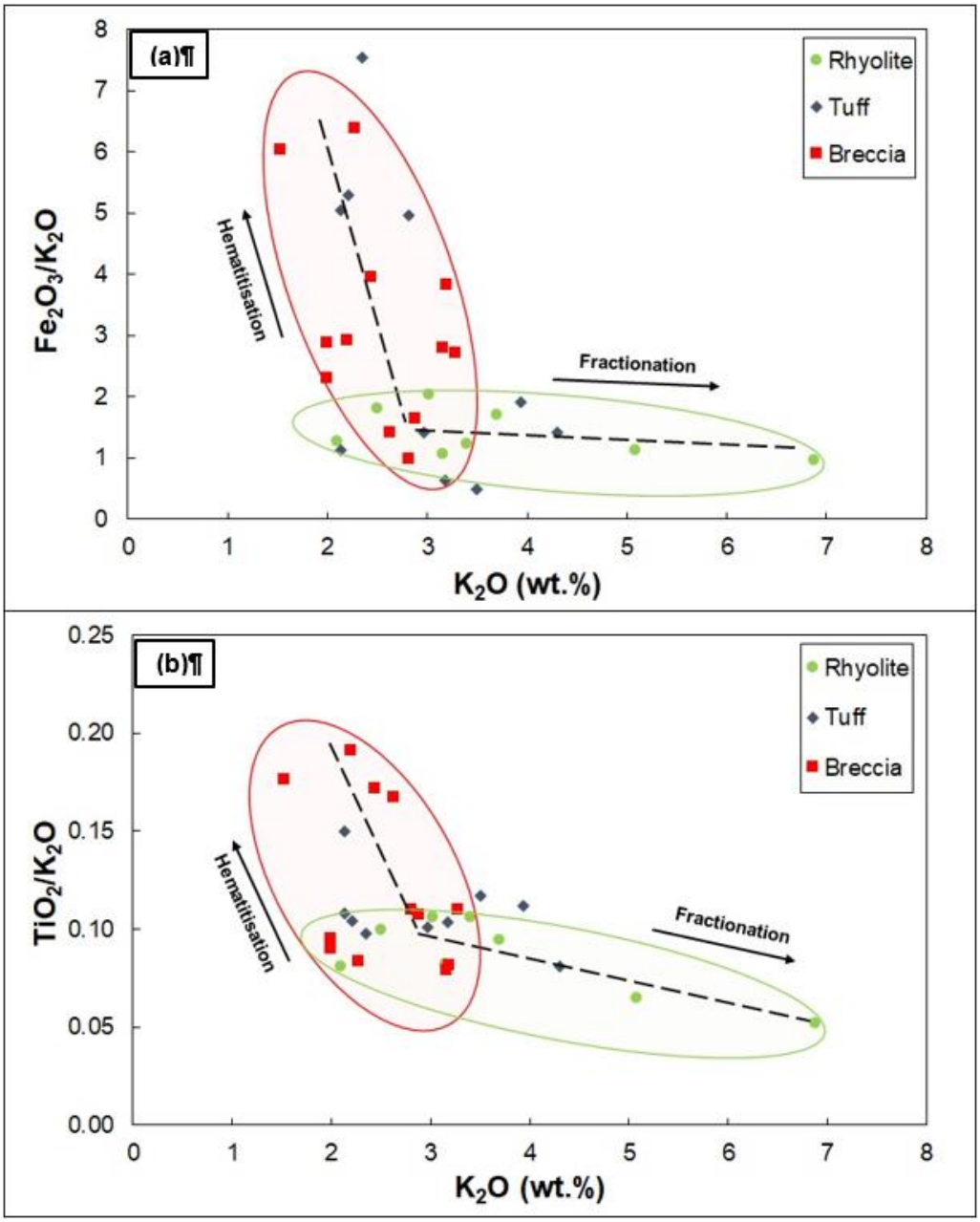

Figure 5.8: Bivariate diagrams of major element ratios of (a) Fe_2O_3/K_2O against K_2O and (b) TiO_2/K_2O against K_2O.

The bivariate plots (Figure 5.8) suggest that the fractionation of rhyolites and deposition of tuffs were likely primary processes in the system and the rocks were

subsequently brecciated and hematitised by secondary Fe-rich fluids. The brecciation and hematitisation process depleted the system in K_2O and enriched it in Fe_2O_3 (Figure 5.8). The high TiO_2/K_2O ratio is therefore to be considered a result of potassium depletion in the system and not titanium enrichment.

5.2.3 Trace elements

The Rb/Sr vs Sr diagram (Figure 5.9) suggests that the upper Schrikkloof Formation is fractionated towards higher Rb/Sr ratios. Commonly, Sr is highly compatible in calcium bearing minerals such as plagioclase, however, Rb is more compatible with potassium bearing minerals such as K-feldspar and mica.

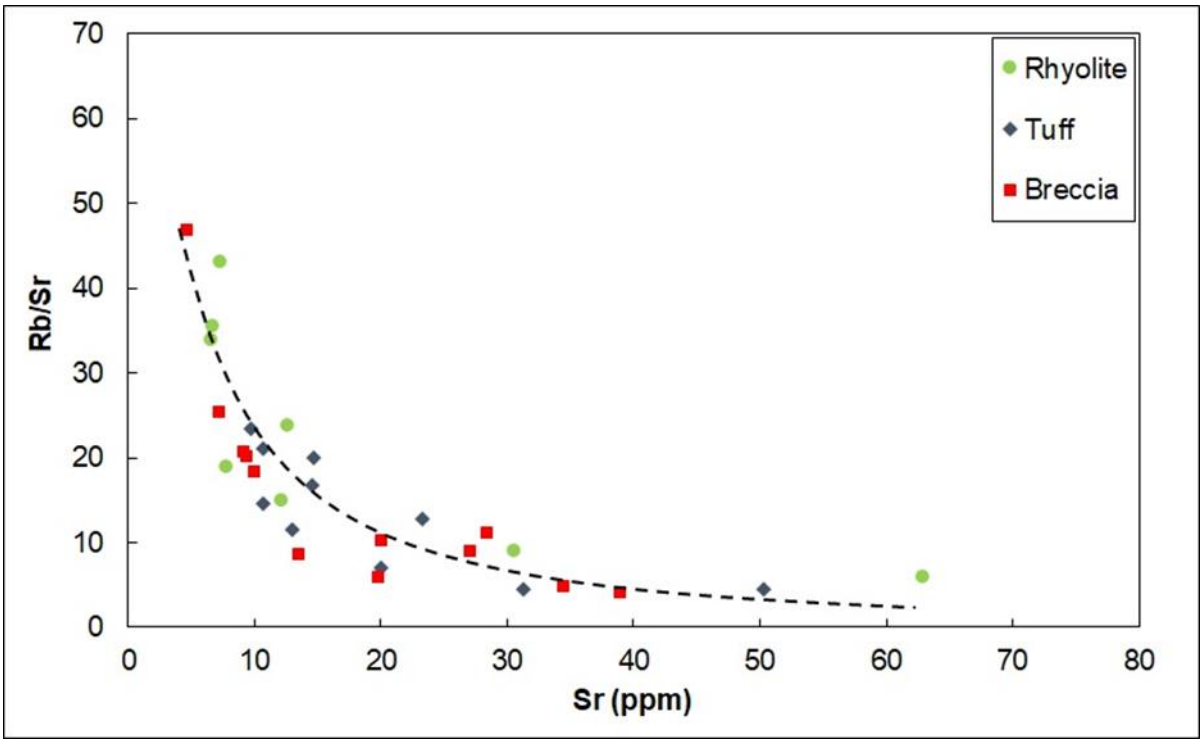

Figure 5.9: Rb/Sr vs Sr plot. Indicates that the upper Schrikkloof Formation is more fractionated towards higher Rb/Sr ratio.

The high Rb/Sr ratio tends to increase towards mineralisation because of the replacement of plagioclase by potassium bearing micas (such as sericite) in felsic rocks. Furthermore, felsic rocks with high Rb/Sr ratio tend be enriched in metals and this ratio can be used as a vector to mineralisation.

The bivariate diagrams of other oxides and trace elements (Al_2O_3, TiO_2, Nb and Y) are plotted against Zr in Figure 5.10. The plots suggest that Al_2O_3, TiO_2, Nb, Y and Zr behave as immobile elements during the hematitisation process. These bivariate diagrams also suggest that rhyolites, tuffs and breccias are genetically related, as suggested by the Harker plots in Figure 5.7. Sample 08, the distinctive Fe-vein, was also plotted with other rocks in Figure 5.10 and it too also followed the trends of these felsic rocks; although it is depleted of rock forming minerals.

The chondrite-normalised REE patterns of rhyolites, tuffs and breccias (Figure 5.11) are compared to the average composition of the upper continental crust, enriched mantle and depleted mantle. The enriched mantle and continental have a relatively high concentration of incompatible light rare earth elements (LREE) compared to the depleted mantle; however, compatible HREE appear to be enriched in the depleted mantle.

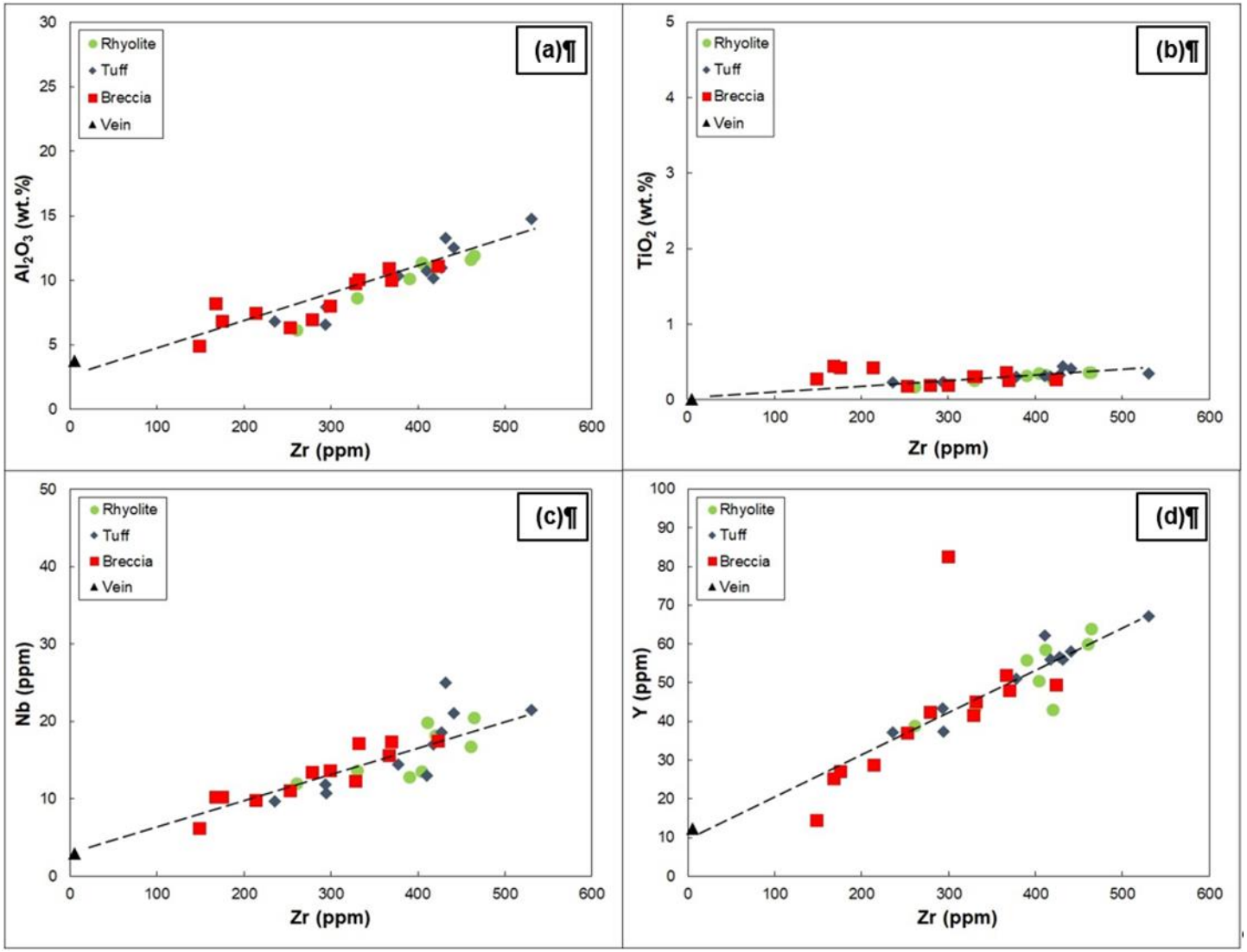

Figure 5.10: Bivariate plots of (a) Al_2O_3 vs Zr; (b) TiO_2 vs Zr; (c) Nb vs Zr; (d) Y and Zr. These plots suggest that Al_2O_3, TiO_2, Nb, Y and Zr are immobile during the hydrothermal alteration process.

Rhyolites, tuffs and hydrothermal breccias have similar REE patterns which show enrichment of light rare earth elements (LREE), a negative Eu anomaly and depletion of heavy rare earth elements (HREE). This pattern is similar to the upper continental crust (Figure 5.11); the negative Eu anomaly is consistent with feldspar fractionation (Rudnick, 1990).

The REE patterns suggest that the Rooiberg Group was derived from melting of crustal material possibly by a fixed heat source genetically related to the Bushveld Magma; as the volcanic rocks of the Rooiberg Group are deposited within the lateral extent of the Rustenburg Layered Suite. During this process, incompatible elements (such as LREE) were probably incorporated into the melt in the magma chamber.

The magma chamber was possibly sitting in the lower- to mid-continental crust, whereby incompatible elements from the country rock are incorporated into the melt during phase separation and crustal contamination of the parental magma (Hatton, 1995; Hatton and Schweitzer, 1995; Buchanan et al., 2002). This may explain the enrichment of REE in the felsic phase of the felsic phase of the Bushveld Complex.

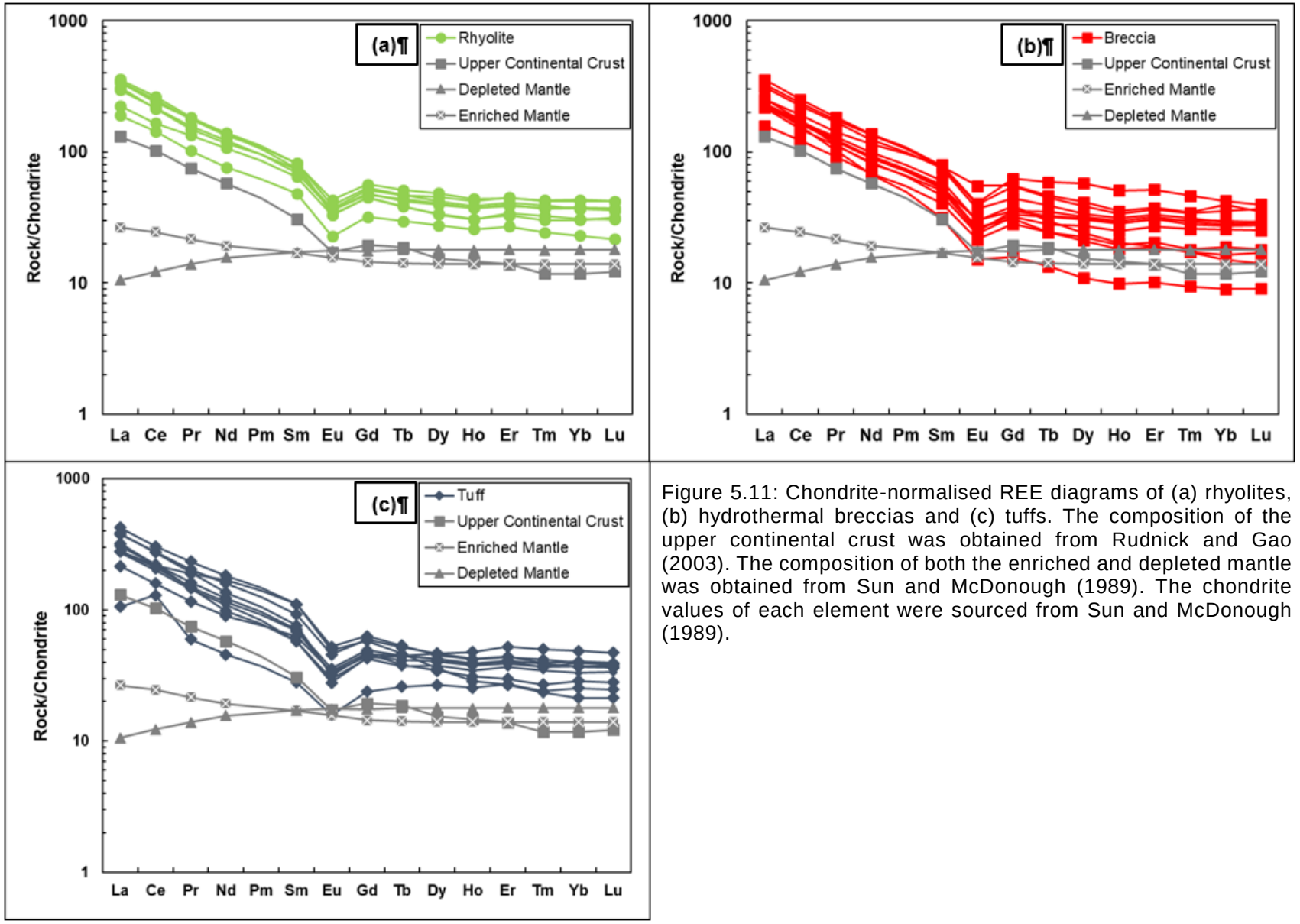

Figure 5.11: Chondrite-normalised REE diagrams of (a) rhyolites, (b) hydrothermal breccias and (c) tuffs. The composition of the upper continental crust was obtained from Rudnick and Gao (2003). The composition of both the enriched and depleted mantle was obtained from Sun and McDonough (1989). The chondrite values of each element were sourced from Sun and McDonough (1989).

5.3 Mass balance

As mentioned above (section 3.3), the chemical constituent's gains and losses associated with hydrothermal alteration processes can be quantified utilizing the isocon approach by Gresens (1967) and Grant (1986). The hydrothermal breccias are primarily hosted by tuffs (Figure 4.1), as such the mass balance calculations and diagrams are going to compare least altered tuffs against hematitised tuffs and hydrothermal breccias.

The mass balance analysis is indicated below in Table 5.1 – 5.6 and their graphical representation is presented in Figures 5.12 and 5.13. Particular chemical elements (SiO_2, TiO_2, Al_2O_3, Fe_2O_3 (t), K_2O, Ce, Cu, La, Nd, Pb, W, Y, Zn and Zr) were considered for mass balance calculations, based on SEM-EDX analysis, petrography and hand-specimen observations.

The concentration of elements data of least altered rocks ($\boldsymbol{C_i^O}$) as well as altered hematitised tuffs or hydrothermal breccia ($\boldsymbol{C_i^A}$) is from geochemical results (Appendix 3). These concentrations were used to calculate the slope from the origin to the data point ($\boldsymbol{C_i^A/C_i^O}$) for each element. The slope of the isocon ($\boldsymbol{M^O/M^A}$) is estimated graphically utilizing Zr and TiO_2 as immobile elements. The mass gain/loss relative to the least altered rock ($\Delta\boldsymbol{C_i/C_i^O}$) is calculated utilizing Equation 3.3.

The scaled values of elements ($\boldsymbol{*C_i^O}$ and $\boldsymbol{*C_i^A}$) for least altered and most altered rocks are plotted in Figure 5.12 and Figure 5.13 to illustrate graphically the gains and losses of chemical constituents. $\boldsymbol{*C_i^O}$ is an arbitrary value used to calculate the scaling factor **($\boldsymbol{*C_i^O/C_i^O}$)**. The value of $\boldsymbol{*C_i^A}$ is simply calculated by multiplying the scaling factor by $\boldsymbol{C_i^A}$**.**

5.3.1 Least altered tuff vs altered hematitised tuff

The isocon analysis of the least altered tuff (Sample 05) is compared to three hematitised tuffs (Sample 35, 36 and 43) in Table 5.1 – 5.3. Sample 35 has an average mass gain of +7.57%, with Sample 36 having an average mass gain of +16.27% and Sample 43 having an average mass gain of +7.22%.

The isocon diagram (Figure 5.12) suggests that Y and Al_2O_3 are relatively immobile during this hematitisation alteration as these elements plot along the isocon. Gains are found for SiO_2, Fe_2O_3, Cu, Pb, Zn and REE (Ce, La, Nd), while the loss in K_2O is due hematitisation and silicification. The gains and losses of W are inconsistent and vary on each rock sample. Other elements are fairly immobile in the system despite alteration.

Table 5.1: Isocon analysis of Sample 05 (least altered tuff) and Sample 35 (altered hematitised tuff). The average mass gain between these two sample is +7.57%.

	Least altered tuff	**Altered hematitised tuff**	**Slope to data point**	**Gain or loss relative to C_i^O**	**Scaling factor**	**Scaled concentrations**	
	C_i^O – Sample 05	**C_i^A – Sample 35**	**C_i^A/C_i^O**	**$\Delta C_i/C_i^O$**	**$(*C_i^O/C_i^O)$**	**$*C_i^O$ – Sample 05**	**$*C_i^A$ – Sample 35**
SiO_2	72.05	70.50	0.98	0.24	0.14	10.00	9.78
TiO_2	0.35	0.31	0.89	0.13	2.29	0.80	0.71
Al_2O_3	14.75	10.18	0.69	-0.12	1.22	18.00	12.42
Fe_2O_3 (t)	6.13	13.98	2.28	1.90	2.61	16.00	36.49
K_2O	4.30	2.82	0.66	-0.17	6.98	30.00	19.67
Ce	135.67	128.45	0.95	0.20	0.17	22.50	21.30
Cu	1.00	16.10	16.10	19.46	1.00	1.00	16.10
La	75.88	66.58	0.88	0.12	0.23	17.50	15.36
Nd	45.80	53.50	1.17	0.48	0.33	15.00	17.52
Pb	12.10	425.40	35.16	43.68	0.06	0.70	24.61
W	3.50	81.80	23.37	28.70	0.43	1.50	35.06
Y	67.28	55.95	0.83	0.06	0.11	7.50	6.24
Zn	12.00	116.00	9.67	11.29	0.06	0.70	6.77
Zr	530.50	417.40	0.79	0.00	0.06	32.50	25.57

Table 5.2: Isocon analysis of Sample 05 (least altered tuff) and Sample 36 (altered hematitised tuff). The average mass gain/loss between these two samples is +16.27%.

	Least altered tuff	Altered hematitised tuff	Slope to data point	Gain or loss relative to C_i^O	Scaling factor	Scaled concentrations	
	C_i^O – Sample 05	C_i^A – Sample 36	C_i^A/C_i^O	$\Delta C_i/C_i^O$	$(*C_i^O/C_i^O)$	$*C_i^O$ – Sample 05	$*C_i^A$ – Sample 36
SiO_2	72.05	72.79	1.01	0.30	0.14	10.00	10.10
TiO_2	0.35	0.32	0.91	0.18	2.29	0.80	0.73
Al_2O_3	14.75	10.73	0.73	-0.06	1.22	18.00	13.09
Fe_2O_3 (t)	6.13	10.76	1.76	1.27	2.61	22.00	38.62
K_2O	4.30	2.13	0.50	-0.36	6.98	30.00	14.86
Ce	135.67	169.38	1.25	0.61	0.17	22.50	28.09
Cu	1.00	12.40	12.40	15.02	1.00	1.00	12.40
La	75.88	89.55	1.18	0.52	0.23	17.50	20.65
Nd	45.80	74.57	1.63	1.10	0.33	15.00	24.42
Pb	12.10	1665.80	137.67	176.82	0.06	0.20	27.53
W	3.50	1.20	0.34	-0.56	0.43	10.00	3.43
Y	67.28	62.18	0.92	0.19	0.11	7.50	6.93
Zn	12.00	313.00	26.08	32.69	0.06	0.70	18.26
Zr	530.50	410.70	0.77	0.00	0.06	32.50	25.16

Table 5.3: Isocon analysis of Sample 05 (least altered tuff) and Sample 43 (altered hematitised tuff). The average mass gain/loss between these two samples is +7.22%.

	Least altered tuff	Altered hematitised tuff	Slope to data point	Gain or loss relative to C_i^O	Scaling factor	Scaled concentrations	
	C_i^O – Sample 05	C_i^A – Sample 43	C_i^A/C_i^O	$\Delta C_i/C_i^O$	$(*C_i^O/C_i^O)$	$*C_i^O$ – Sample 05	$*C_i^A$ – Sample 43
SiO_2	72.05	79.03	1.10	0.54	0.14	10.00	10.97
TiO_2	0.35	0.30	0.86	0.20	2.29	0.80	0.69
Al_2O_3	14.75	10.34	0.70	-0.02	1.22	18.00	12.62
Fe_2O_3 (t)	6.13	4.20	0.69	-0.04	0.65	4.00	2.74
K_2O	4.30	2.97	0.69	-0.03	6.98	30.00	20.72
Ce	135.67	122.81	0.91	0.27	0.17	22.50	20.37
Cu	1.00	20.40	20.40	27.64	1.50	0.15	30.60
La	75.88	65.13	0.86	0.21	0.23	17.50	15.02
Nd	45.80	50.77	1.11	0.56	0.33	15.00	16.63
Pb	12.10	306.10	25.30	34.52	0.02	0.20	5.06
W	3.50	5.30	1.51	1.13	2.86	10.00	15.14
Y	67.28	50.99	0.76	0.06	0.11	7.50	5.68
Zn	12.00	317.00	26.42	36.09	0.06	0.70	18.49
Zr	530.50	377.90	0.71	0.00	0.07	36.00	25.64

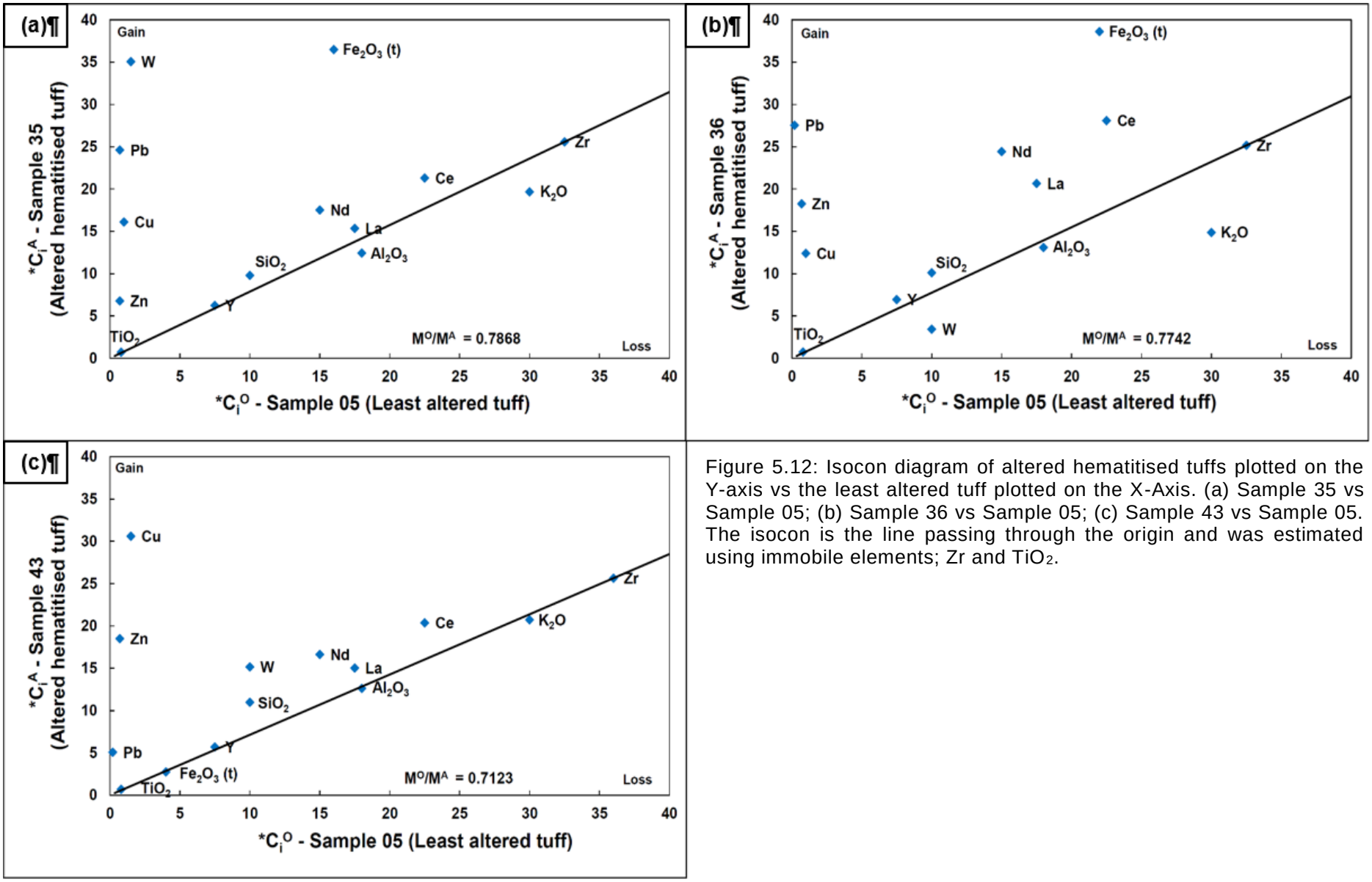

Figure 5.12: Isocon diagram of altered hematitised tuffs plotted on the Y-axis vs the least altered tuff plotted on the X-Axis. (a) Sample 35 vs Sample 05; (b) Sample 36 vs Sample 05; (c) Sample 43 vs Sample 05. The isocon is the line passing through the origin and was estimated using immobile elements; Zr and TiO_2.

5.3.2 Least altered tuff vs hydrothermal breccia

Another relatively unaltered tuff (Sample 18) is compared against three hydrothermal breccias (Sample 09, 24 and 30). The results are in Table 5.4 – 5.6. The relative mass gain for Sample 09, 24 and 30 is +1.02%, +1.18% and +0.58%, respectively. The isocon diagrams of hydrothermal breccias in Figure 5.13 suggest that the major gains are in Fe_2O_3, Cu, Pb, Zn and losses are recorded for of SiO_2, K_2O and REE (Ce, La, Nd). The depletion of REE is possibly because the physiochemical properties in the system were not conducive for precipitating these elements.

Other elements such as Y and W are inconsistent as gains and losses vary in different rocks. Al_2O_3 also behaves as immobile element as it plots along the isocon line. These brecciated samples have less potential for mineralisation as they are depleted in REE; this might indicate that these breccias represent fluid pathways while the hematitised tuffs are suitable traps for the hydrothermal fluids.

Table 5.4: Isocon analysis of Sample 18 (least altered tuff) and Sample 09 (hydrothermal breccia). The average mass gain/loss between these two samples is +1.02%.

	Least altered tuff	**Hydrothermal breccia**	**Slope to data point**	**Gain or loss relative to C_i^O**	**Scaling factor**	**Scaled concentrations**	
	C_i^O – Sample 18	**C_i^A – Sample 09**	**C_i^A/C_i^O**	**$\Delta C_i/C_i^O$**	**$(*C_i^O/C_i^O)$**	**$*C_i^O$ – Sample 18**	**$*C_i^A$ – Sample 09**
SiO_2	86.96	73.34	0.84	-0.34	0.40	35.00	29.52
TiO_2	0.23	0.19	0.83	-0.35	4.35	1.00	0.83
Al_2O_3	6.83	8.03	1.18	-0.07	2.64	18.00	21.16
Fe_2O_3 (t)	2.43	14.51	5.97	3.70	2.06	5.00	29.86
K_2O	2.13	2.27	1.07	-0.16	14.08	30.00	31.97
Ce	134.79	116.77	0.87	-0.32	0.05	7.00	6.06
Cu	4.40	8.70	1.98	0.56	1.14	5.00	9.89
La	66.46	59.53	0.90	-0.29	0.26	17.50	15.68
Nd	79.30	53.47	0.67	-0.47	0.15	12.00	8.09
Pb	54.70	71.10	1.30	0.02	0.18	10.00	13.00
W	3.70	52.50	14.19	10.17	0.54	2.00	28.38
Y	37.13	82.58	2.22	0.75	0.40	15.00	33.36
Zn	14.00	37.00	2.64	1.08	0.21	3.00	7.93
Zr	235.90	299.60	1.27	0.00	0.11	25.00	31.75

Table 5.5: Isocon analysis of Sample 18 (least altered tuff) and Sample 24 (hydrothermal breccia). The average mass gain/loss between these two samples is +1.18%.

	Least altered tuff	Hydrothermal breccia	Slope to data point	Gain or loss relative to C_i^O	Scaling factor	Scaled concentrations	
	C_i^O – Sample 18	C_i^A – Sample 24	C_i^A/C_i^O	$\Delta C_i/C_i^O$	$(*C_i^O/C_i^O)$	$*C_i^O$ – Sample 18	C_i^A – Sample 24
SiO_2	86.96	74.22	0.85	-0.45	0.40	35.00	29.87
TiO_2	0.23	0.36	1.57	0.01	2.17	0.50	0.78
Al_2O_3	6.83	10.89	1.59	0.03	2.64	18.00	28.70
Fe_2O_3 (t)	2.43	8.90	3.66	1.35	2.06	5.00	18.31
K_2O	2.13	3.28	1.54	-0.01	2.35	5.00	7.70
Ce	134.79	145.00	1.08	-0.31	0.17	22.50	24.20
Cu	4.40	5.60	1.27	-0.18	0.45	2.00	2.55
La	66.46	77.92	1.17	-0.25	0.26	17.50	20.52
Nd	79.30	63.06	0.80	-0.49	0.23	18.00	14.31
Pb	54.70	172.30	3.15	1.03	0.18	10.00	31.50
W	3.70	52.50	14.19	8.12	0.27	1.00	14.19
Y	37.13	51.92	1.40	-0.10	0.27	10.00	13.98
Zn	14.00	191.00	13.64	7.77	0.18	2.50	34.11
Zr	235.90	366.90	1.56	0.00	0.11	25.00	38.88

Table 5.6: Isocon analysis of Sample 18 (least altered tuff) and Sample 30 (hydrothermal breccia). The average mass gain/loss between these two samples is +0.58%.

	Least altered tuff	Hydrothermal breccia	Slope to data point	Gain or loss relative to C_i^O	Scaling factor	Scaled concentrations	
	C_i^O – Sample 18	C_i^A – Sample 30	C_i^A/C_i^O	$\Delta C_i/C_i^O$	$(*C_i^O/C_i^O)$	$*C_i^O$ – Sample 18	C_i^A – Sample 30
SiO_2	86.96	78.98	0.91	-0.35	0.40	35.00	31.79
TiO_2	0.23	0.31	1.35	-0.03	2.17	0.50	0.67
Al_2O_3	6.83	9.76	1.43	0.03	2.64	18.00	25.72
Fe_2O_3 (t)	2.43	4.72	1.94	0.39	4.12	10.00	19.42
K_2O	2.13	2.88	1.35	-0.03	2.35	5.00	6.76
Ce	134.79	103.10	0.76	-0.45	0.17	22.50	17.21
Cu	4.40	6.50	1.48	0.06	0.45	2.00	2.95
La	66.46	54.97	0.83	-0.41	0.26	17.50	14.47
Nd	79.30	43.63	0.55	-0.61	0.23	18.00	9.90
Pb	54.70	229.20	4.19	2.01	0.16	9.00	37.71
W	3.70	1.30	0.35	-0.75	3.24	12.00	4.22
Y	37.13	41.47	1.12	-0.20	0.27	10.00	11.17
Zn	14.00	185.00	13.21	8.48	0.18	2.50	33.04
Zr	235.90	328.80	1.39	0.00	0.11	25.00	34.85

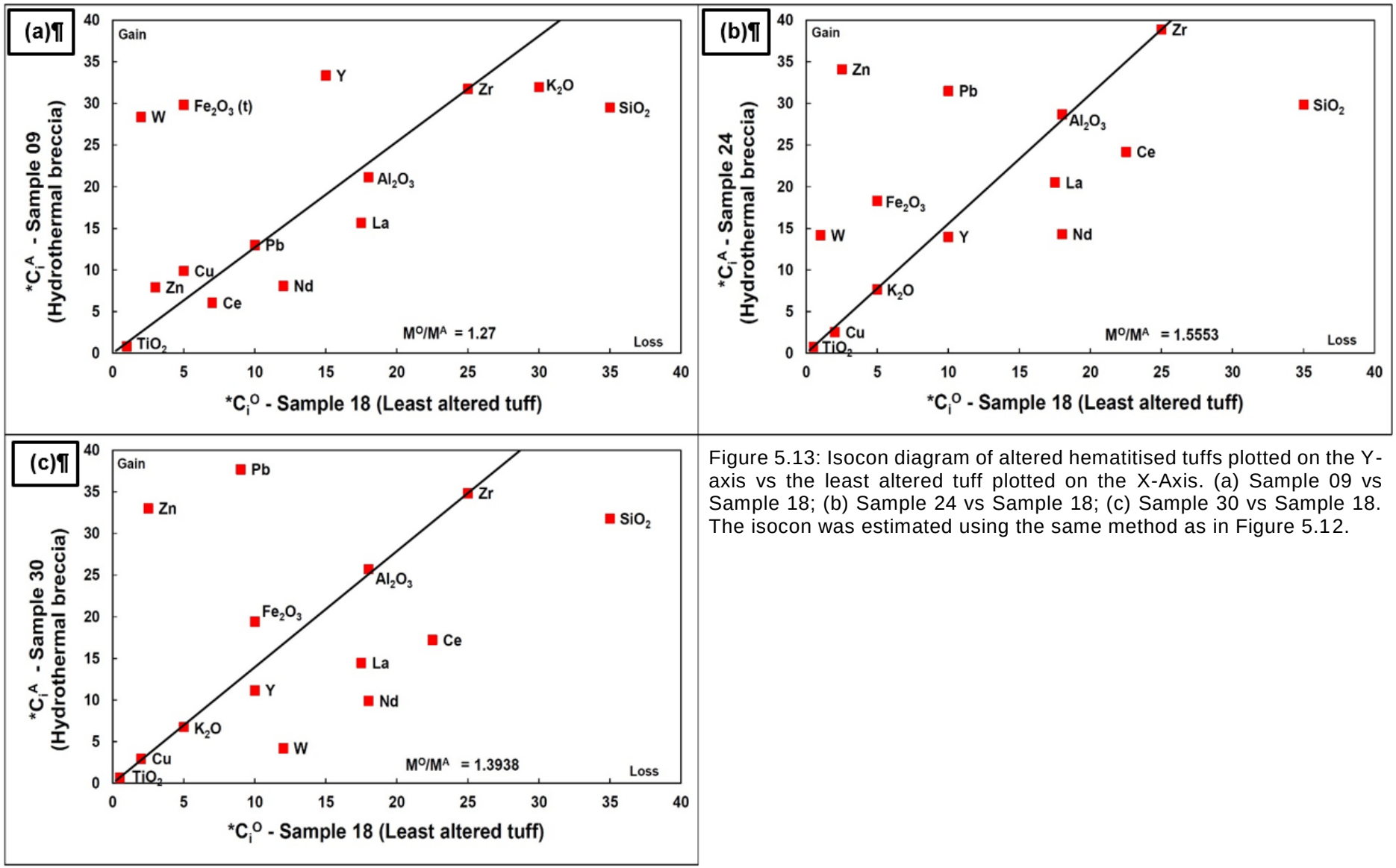

Figure 5.13: Isocon diagram of altered hematitised tuffs plotted on the Y-axis vs the least altered tuff plotted on the X-Axis. (a) Sample 09 vs Sample 18; (b) Sample 24 vs Sample 18; (c) Sample 30 vs Sample 18. The isocon was estimated using the same method as in Figure 5.12.

5.4 Geostatistics: Box and whisker plots

The above mass balance graphs in Figures 5.12 and 5.13 indicate that hydrothermal alteration and hematitisation produced a gain of base metals (particularly Cu, Pb, Zn). However, these mass balance graphs do not indicate the average concentration of chemical elements within rhyolites, tuffs and hydrothermal breccias. Box and whisker plots of the three elements can better visualise the data distribution through mean and quartiles

The average crustal abundance of Cu, Pb and Zn is 28, 17 and 67 ppm, respectively (Rudnick and Gao, 2003), and is reported as a dashed blue line in Figure 5.14.

5.4.1 Pb-Zn-Cu

The average concentration of Cu in rhyolites, tuffs and hydrothermal breccias is 19.2, 24.5 and 4.97 ppm, respectively (Figure 5.14a). This shows that the concentration of Cu is below the average crustal abundance (Figure 5.14a). Lead is constantly above the crustal average: rhyolites have a maximum Pb concentration of 576 ppm and an average of 192 ppm. The average Pb concentration in tuffs is 454 ppm with a maximum of 770 ppm; a peak in Pb of 1666 ppm is found in the tuffs (Figure 5.14b). Hydrothermal breccias have average of 73.3 ppm and a maximum of 230 ppm (Figure 5.14b). This again attests that the Pb concentration in the study area is higher than the crustal average.

The average Zn concentration in rhyolites, tuffs and hydrothermal breccia is 157, 194 and 64.3 ppm, respectively (Figure 5.14c). The maximum Zn concentration in rhyolites, tuffs and hydrothermal breccias is 304, 550 and 191 ppm, respectively. Both rhyolites and tuffs appear to have a higher Zn content compared to the Earth crust;

however, hydrothermal breccias have a Zn content almost equivalent to the Earth's crust.

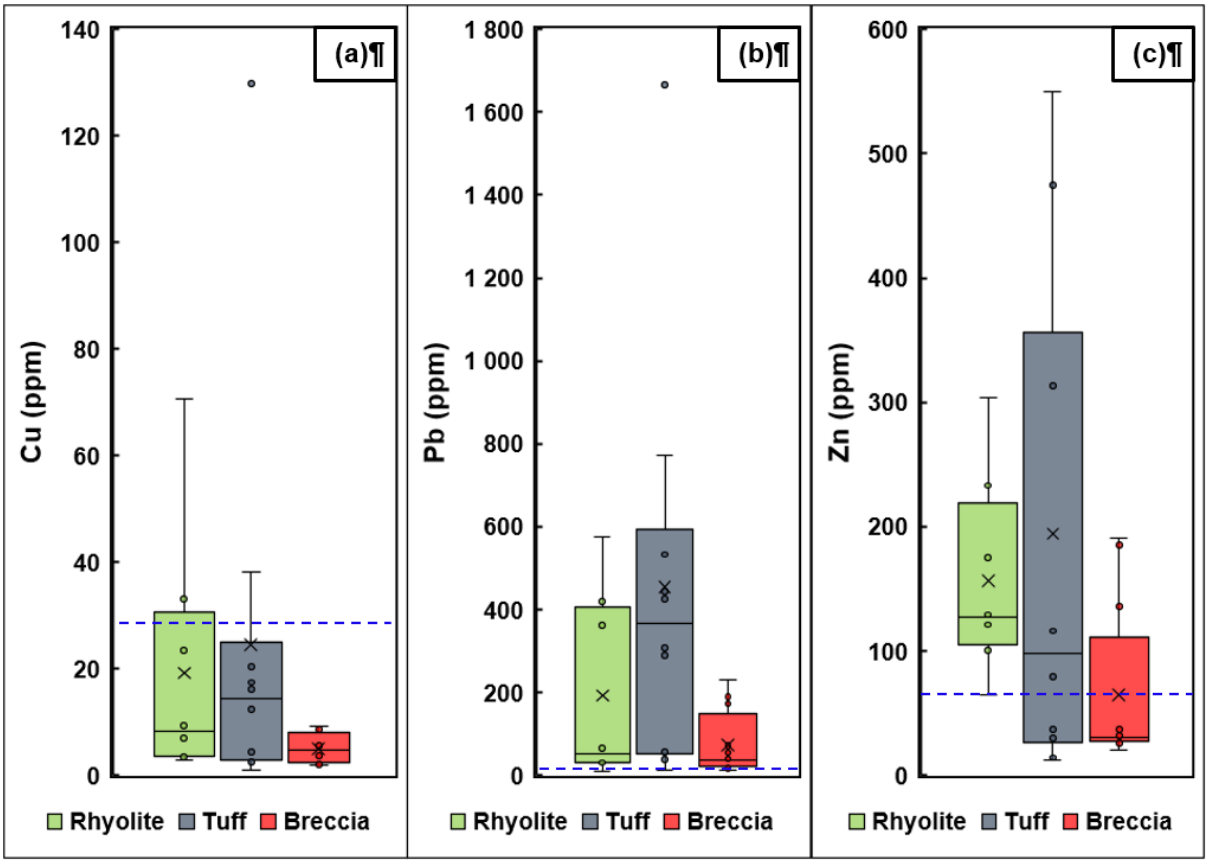

Figure 5.14: Box and whisker plots of (a) Cu; (b) Pb; and (c) Zn. Rhyolites and tuffs have a higher Pb and Zn contents relative to the Earth's crust. The average Zn content of hydrothermal breccias is similar to the Earth's crust. The average concentration (mean) of each chemical constituent is indicated with an "x". The blue line indicates the average crustal abundance of each element (see Rudnick and Gao, 2003).

5.4.2 LREE (Ce-La-Nd)

The average Ce content in rhyolites, tuffs and hydrothermal breccias is 133, 136 and 111 ppm (respectively) and is slightly higher than the crustal abundance (Figure 5.15a). La has averages of 71.2, 70.4 and 59.7 ppm for rhyolites, tuffs and hydrothermal breccia (respectively) and are to some extent greater than that of the crustal abundance (Figure 5.15b). Nd has averages of 59.7, 57.3 and 46.2 ppm for

rhyolites, tuffs and hydrothermal breccias (respectively) and appears to have concentrations higher the average Earth's crust (Figure 5.15c).

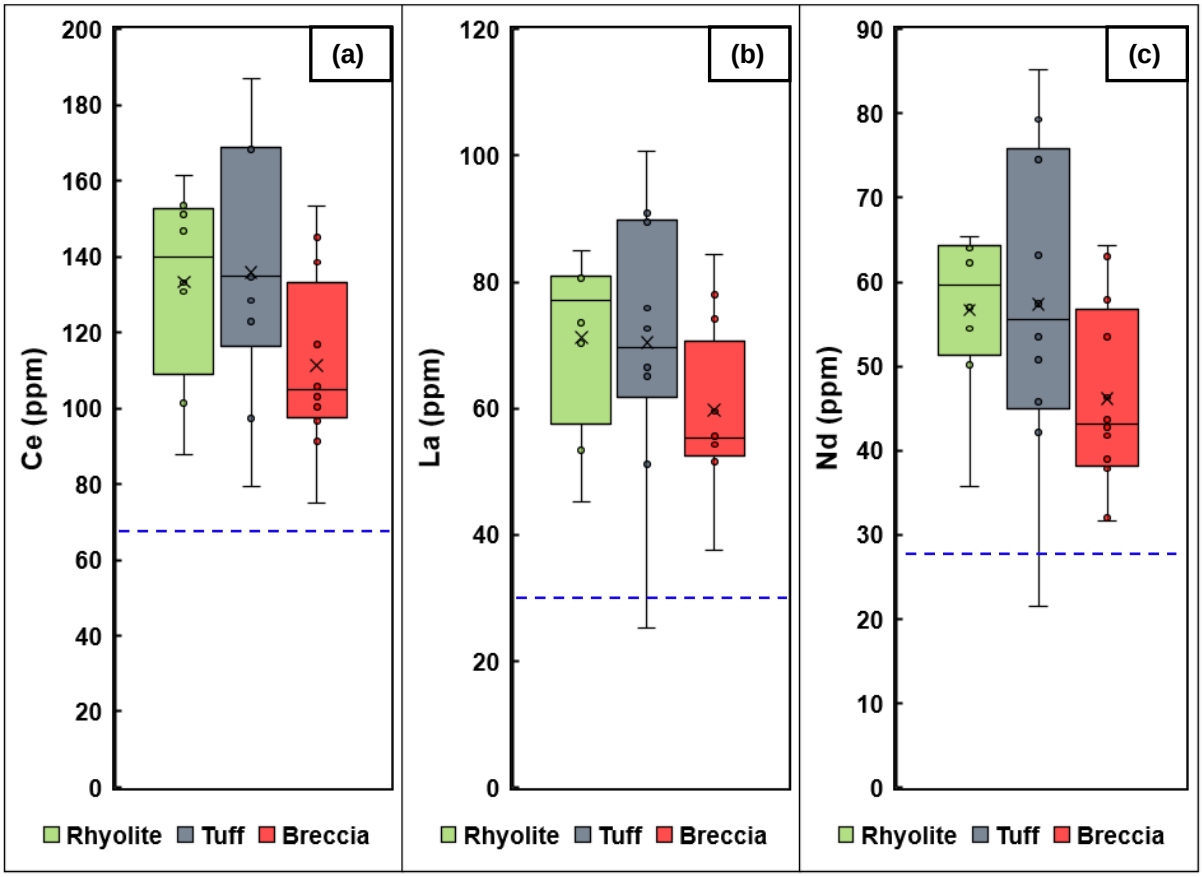

Figure 5.15: Box and whisker plots of (a) Ce; (b) La, and (c) Nd. The blue line indicates the average crustal abundance of each element (see Rudnick and Gao, 2003).

6 Discussion

6.1 Tectonic Setting

Although the use of the discrimination diagram of Fig. 5.6 cannot be resolute in assessing the tectonic setting of our rocks, the results (Figure 5.6) suggest that the Schrikkloof Formation shares affinity with a within-plate setting, and this agrees with the Bushveld Complex (including the Rooiberg Group) being emplaced within the Kaapvaal Craton at ca. ~2.06 Ga (Walraven, 1997, Zeh et al., 2015). It is known that the Bushveld Complex intruded into this Archean craton in a region cross cut by numerous shear zones (Figure 6.1), including the Thabazimbi-Murchison Lineament (TML) and Zoetfontein-Palala Shear Zone (Zeh et al., 2015; Lenhardt et al., 2017).

The TML and Zoetfontein-Palala Shear Zone possibly formed between ca. 2.97 and 2.65 Ga during the amalgamation events of the Witwatersrand Terrane, Pietersburg/Giyani Terrane, Zimbabwe Craton and Limpopo Belt; in addition, it has been reactivated several times until 1.89 Ga (Good and de Wit, 1997; Zeh et al., 2013, 2015). There is evidence of post-Bushveld Complex transpressional deformation at ca. 1.89 Ga, preserved in the younger Waterberg Group (Good and de Wit, 1997).

At 2.05 Ga, the TML experienced dilation due to compression in the NW-SE direction (Figure 6.1b) triggered by the collision of the Zimbabwe and Kaapvaal cratons (Clarke et al., 2009). In this scenario, the TML would possibly sit in an extensional rift zone parallel to the craton collision boundary (Clarke et al., 2009). The deposition of the Rooiberg Group at ca. ~2.06 Ga (Walraven, 1997) possibly indicates the initial dilation of the TML and intrusion of the Bushveld Complex Magma into the Transvaal Supergroup (Clarke et al., 2009).

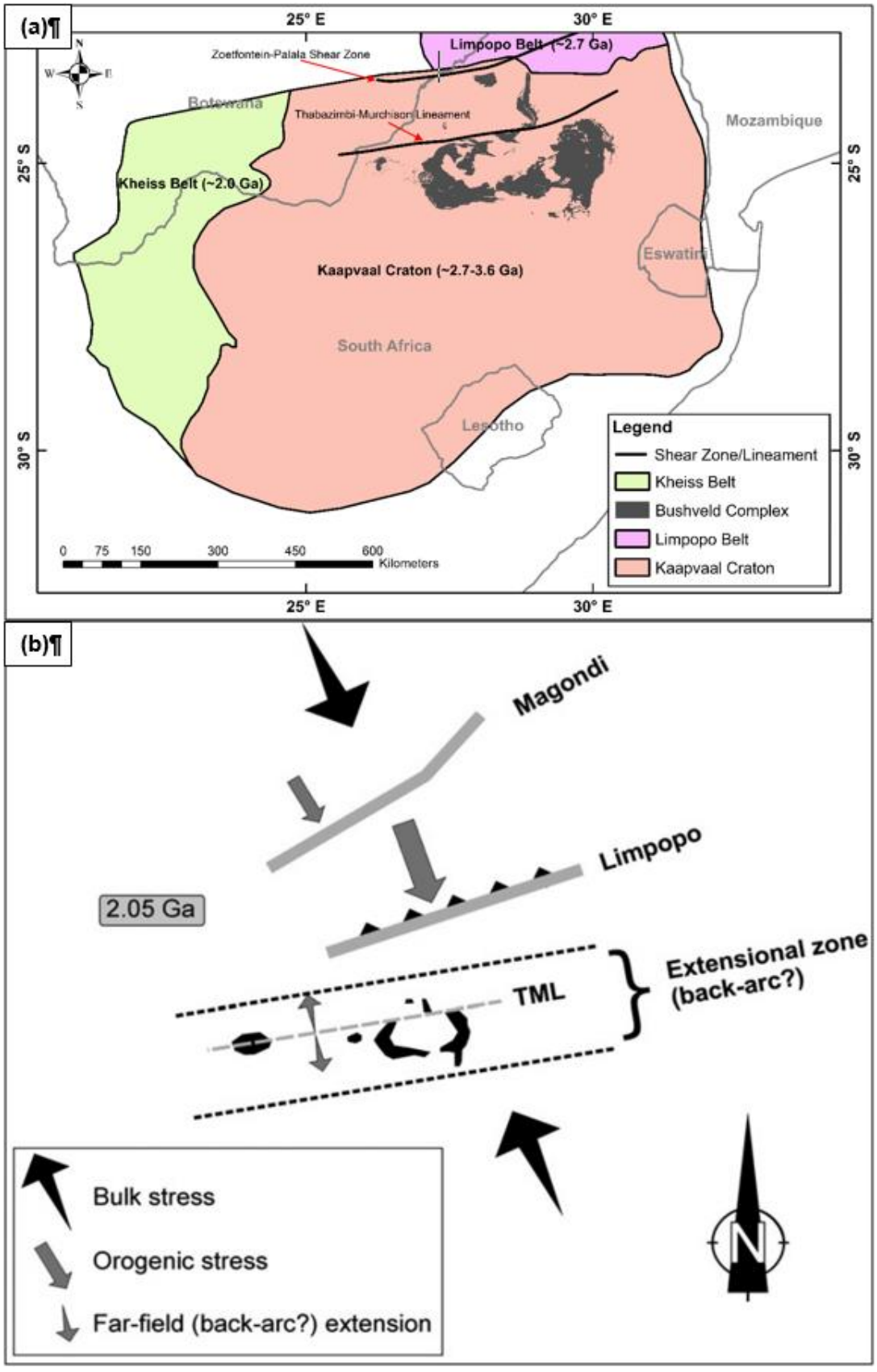

Figure 6.1: (a) Geological map indicating the position of the Bushveld Complex relative to the Kaapvaal Craton, Limpopo Belt and Kheiss Belt. Modified from James et al. (2001) and Rajesh et al. (2020). (b) Emplacement of the Bushveld Complex in an extensional rift zone (Clarke et al., 2009).

6.2 Schrikkloof Formation Emplacement Model

The petrogenesis of the Rooiberg Group and Bushveld Complex has been well studied in the past (e.g., Rhodes, 1975; Twist, 1985; Von Gruenewaldt and Harmer, 1992; Hatton, 1995; Hatton and Schweitzer, 1995; Buchanan and Reimold, 1998; Buchanan et al., 1999, 2002, 2004; VanTongeren et al., 2010, 2016; VanTongeren and Mathez, 2013, 2015; Lenhardt et al., 2017).

Twist (1985) suggested that there are nine distinct magma types of the Rooiberg Group located ~30 km south of Groblersdal (Figure 1.1), including a high magnesium type (MgO > 1.7%), a low magnesium type (MgO < 1.0%) and a Fe-Ti-P type. Schweitzer et al. (1995a, 1995b) corroborated the findings of Twist (1985), and the nine magma types, their equivalent formations and facies are summarised in Table 6.1 (Schweitzer et al., 1995a, 1995b; Lenhardt et al., 2017). Lenhardt et al. (2017) infer that the magma types (including the Damwal, Kwaggasnek and Schrikkloof Formations) erupted and deposited as well welded lava-like rheomorphic ignimbrites.

The observed petrographic textures (section 4.5) of these volcanic rocks are commonly sparsely porphyritic (Figure 4.11 and 4.12) to glassy (Figure 4.13 and 4.14); the tuffaceous rocks commonly show clasts of different sizes (Figure 4.4a). The sparsely porphyritic texture indicates that a high temperature K-feldspar, possibly sanidine phenocrysts, formed in the magma chamber prior the volcanic eruption, and is consistent with previous findings (Hatton and Schweitzer, 1995; Lenhardt et al., 2017). Subsequent to the crystallisation of K-feldspar, the Schrikkloof magma erupted (at temperatures < 1100 °C) to the surface and hence developing a glassy groundmass (Hatton and Schweitzer, 1995; Lenhardt et al., 2017).

Table 6.1: Rooiberg Group magma types, their equivalent formations and lithofacies. Modified from Schweitzer et al. (1995a, 1995b) and Lenhardt et al., (2017).

Magma type	**Formation**	**Facies**
Low magnesium	Schrikkloof	Flow-banded zone
Low magnesium	Kwaggasnek	Massive, dense, vesicular, locally columnar zone
Low magnesium High Fe-Ti-P	Damwal	Porphyritic, crystal-rich zone
High Fe-Ti-P High Titanium Basalt High Magnesium Basal Rhyolite Low Titanium Basaltic Andesite	Dullstroom	Various magma types

Bulk rock composition and petrography observations indicate that the groundmass is quartz rich. The micro-textures and flow-banding observed in the field (Figure 4.3) indicate that the magmatism of the Schrikkloof Formation in the Modimolle area is regionally consistent with the findings of Lenhardt et al., (2017). Textures and field observations also suggest that the emplacement of the Schrikkloof Formation was explosive and formed the upper facies of the Rooiberg Group. In addition, textures and geochemistry of the Schrikkloof Formation indicate that the deposition and emplacement Rooiberg Group was in a subaerial environment in an intra-cratonic setting.

The tuffaceous material may have been ejected from the volcano contemporaneously with magma during this violent eruption episode, rapidly cooling on the surface. Both

porphyritic and glassy textures suggest that the Schrikkloof Formation was emplaced in a subaerial environment (Figure 6.2) above the Transvaal Supergroup. The intrusive emplacement of the Lebowa Granite Suite and Rustenburg Layered Suite relative to the Rooiberg Group and Transvaal Supergroup is shown in Figure 6.2.

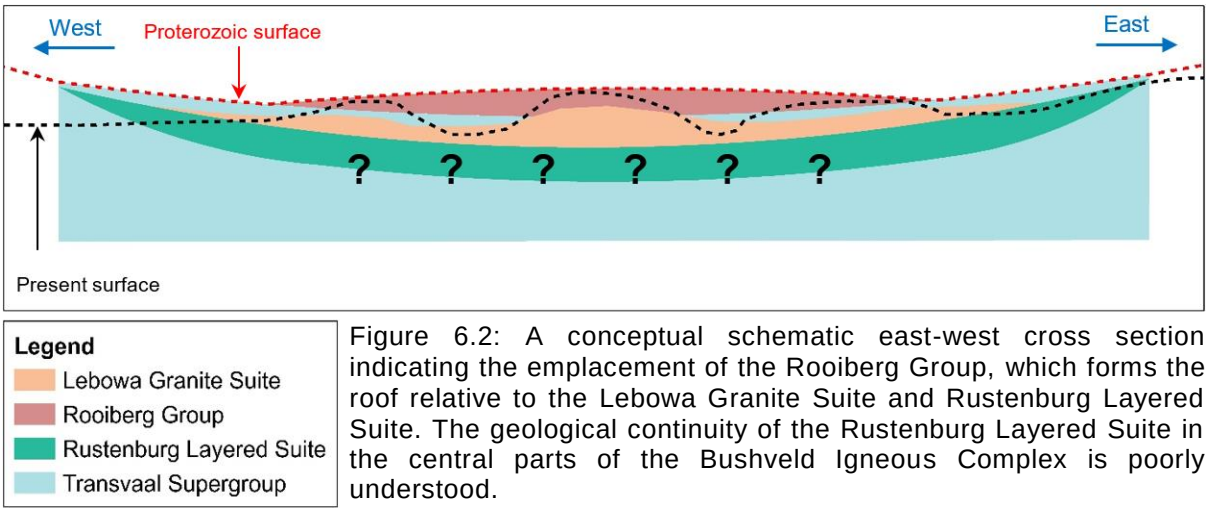

Figure 6.2: A conceptual schematic east-west cross section indicating the emplacement of the Rooiberg Group, which forms the roof relative to the Lebowa Granite Suite and Rustenburg Layered Suite. The geological continuity of the Rustenburg Layered Suite in the central parts of the Bushveld Igneous Complex is poorly understood.

The schematic emplacement model indicates that the Rooiberg Group was predominantly erupted and deposited in terrains underlain by the Lebowa Granite Suite, Rustenburg Layered Suite and Transvaal Supergroup (Figure 6.2); there are no remnants of the Rooiberg Group preserved beyond the aforementioned geological units.

In addition to close spatial correlation, the Rooiberg Group, Rustenburg Layered Suite, Lebowa Granite Suite and Rashoop Granophyre Suite have synchronous ages (Coertze et al., 1978; Walraven and Hattingh, 1993; Walraven, 1997; Zeh et al., 2015) and similar isotopic signatures (Buchanan et al., 2002; Buchanan et al., 2004; Fourie and Harris, 2011), suggesting that these units are probably derived from the same parental magma source.

The whole rock geochemistry (particularly K and Zr) and cumulate mineral assemblages of the Rustenburg Layered Suite indicate that a fractionated melt (with a felsic composition) may have escaped from the magma chamber (Cawthorn and Walraven, 1998; VanTongeren et al., 2010). This fractionated felsic magma was possibly discharged from the magma chamber, partially melting the continental crust and erupting on surface to form the Rooiberg Group and/or Rashoop Granophyre Suite (VanTongeren et al., 2010).

6.3 Role and composition of hydrothermal fluids

6.3.1 Mineralogy and Lithogeochemistry

The geochemical classification (Figure 5.5) and the SEM-EDX analysis (Figure 5.1 – 5.4) indicate that the host of these hydrothermal breccias is rhyolitic to rhyodacitic in composition. The host rock is predominantly composed of primary fine grained microgranular quartz (SiO_2) and elongate sericitised K-feldspar phenocrysts with simple twinning (Figure 4.12); the presence of sericite supports the addition of water to the system after crystallisation. The hydrolysis alteration of K-feldspar to form sericite is summarised by the equation 6.1 below:

$$\underset{\textit{(K-feldspar)}}{3KAlSi_3O_{8\,(s)}} + 2H^+ \longrightarrow \underset{\textit{(Sericite)}}{KAl_3Si_3O_{10}(OH)_{2\,(s)}} + \underset{\textit{(Quartz)}}{6SiO_{2\,(s)}} + 2K^+ \qquad \textbf{[6.1]}$$

This sericitisation alteration process indicates that secondary quartz is formed as a bi-product, and that excess potassium is perhaps flushed out from the system. The groundmass of the sericitised K-feldspar phenocrysts is compositionally similar to the tuffaceous glassy rocks, and both groundmass (Figure 4.11) tuffaceous glassy rocks are cross cut by opaque hematite veins with alteration halos (Figure 4.13a and 4.14a). The SEM-EDX analysis of a hydrothermal breccia (Figure 5.1) indicates that the fluids

in the system are predominantly composed of hematite (Fe_2O_3) and the host rock is quartz-rich.

However, sulphur has been added to the system as anglesite has been documented ($PbSO_4$; Figure 5.1 – 5.4). The mineral commonly forms as result of oxidation of galena (PbS) deposits (Klein and Dutrow, 2007; Sergeev et al, 2017; Verhaert et al., 2017; Liu et al., 2022). Anglesite probably formed from galena reacting with sulphuric acid and the process can be summarised in the equation below:

$$\underset{\textit{(Galena)}}{PbS_{(s)}} + \underset{\textit{(Sulphuric acid)}}{H_2SO_{4\,(aq)}} \longrightarrow \underset{\textit{(Anglesite)}}{PbSO_{4\,(s)}} + H_2S_{(g)} \quad \textbf{[6.2]}$$

with hydrogen sulphide gas possibly escaped from the system through cracks and joints.

Furthermore, the SEM-EDX analysis of Sample 36 (Figure 5.3b) revealed the presence of monazite, a REE bearing mineral, associated with chlorite. This iron rich chlorite could have formed by alteration of biotite by water (fluid) according to the equation below:

$$\underset{\textit{(Biotite)}}{2KFe_3AlSi_3O_{10}(OH)_{2(s)}} + \underset{\textit{(Water)}}{2H_2O_{(aq)}} \longrightarrow K_2O + \underset{\textit{(Chlorite)}}{Fe_5Al_2Si_3O_{10}(OH)_{8(s)}} + \underset{\textit{(Quartz)}}{3SiO_{2(s)}} + FeO \quad \textbf{[6.3]}$$

Equation 6.3 indicates that biotite was likely altered to chlorite, quartz and minor wustite (FeO), and that potassium was remobilised and possibly depleted in the system. Biotite possibly crystallised as a primary igneous mineral and monazite could have formed as a secondary hydrothermal mineral in the system. Biotite was subsequently altered, but monazite was well preserved because of its resistance to

chemical alteration. There are thin chlorite veins (Figure 5.3b) associated with monazite which commonly has a grain size <250 µm) and anhedral shape.

6.3.2 Elemental Gains and Losses

The isocon analysis as well as box and whisker plots indicate that there is significant gain of Pb-Zn relative to the average crust. A Pb-bearing mineral (anglesite) was detected using SEM-EDX analysis, whereas no Zn-bearing minerals have been identified; however, the whole rock geochemistry indicated relatively high concentrations of Zn. It is possible that Zn has been oxidised and is hosted within anglesite or veins; hence it is difficult to located and analyse using the SEM-EDX technique.

The gains of Pb-Zn are documented in hydrothermal breccias and highly hematitised tuffs, as suggested by the mineralogy of veins as well as whole rock geochemistry. Hematitised tuffs tends to have a relatively high concentration of Pb-Zn compared to hydrothermal breccias, possibly because Fe-rich fluids had a long resident time within tuffs. This suggests that tuffs were a trap for fluids, although some fluids may have escaped in the system. The isocon analysis as well as box and whisker plots indicate that Pb-Zn and/or REE-bearing minerals are potentially hosted within hematitised tuffs of the Schrikkloof Formation.

The pathways of Fe-rich fluids can be found in rhyolites, however, tuffs appear to be a trap for these hydrothermal fluids. The source of these fluids is possibly from a differentiated granites of the Lebowa Granite Suite; the nature and origin of hydrothermal fluids commonly control mineralisation of base metals. The absence of Sn minerals in the study area might suggest that the hydrothermal fluids were not

derived from the Sn-rich zone of the Lebowa Granite Suite. The mineralisation model of these fluids is discussed below in section 6.4.

6.4 Mineralisation model

Field observations (chapter 4) indicate that hydrothermal breccias formed after the emplacement of the Rooiberg Group and before the deposition of the Waterberg Group. This suggests that the source of fluids comes from a differentiated felsic magma younger than the Rooiberg Group but older than the Waterberg Group. The most differentiated granites of the Lebowa Granite Suites are perhaps the source of fluids or Rooiberg Group itself maybe the source of fluids (Figure 6.3).

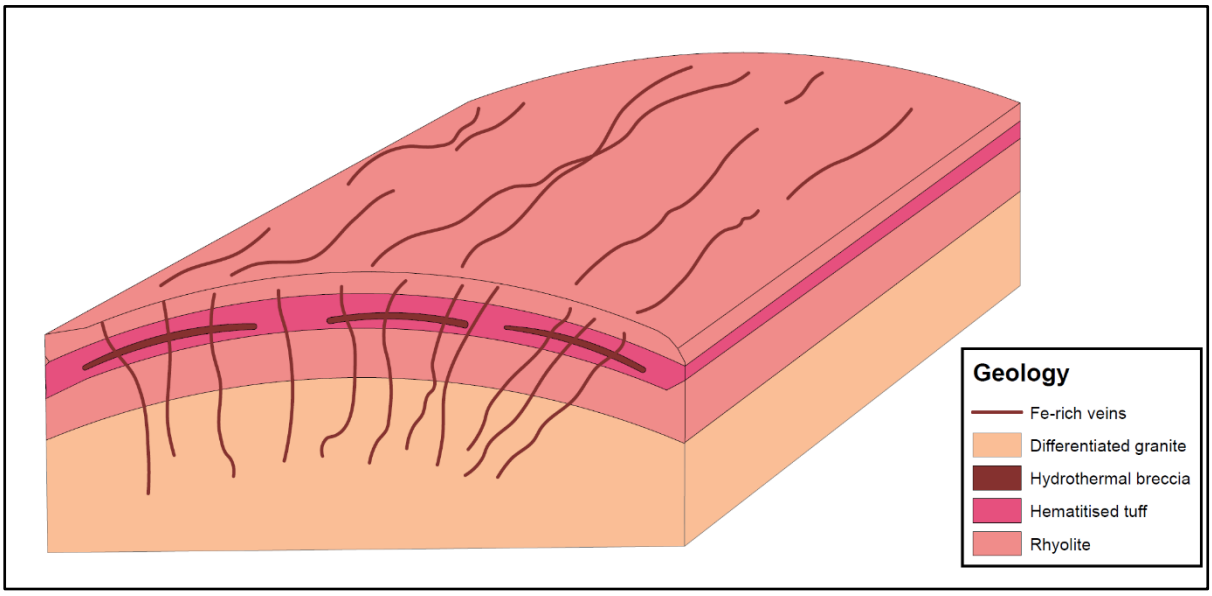

Figure 6.3: A conceptual geological model of how hydrothermal breccia and the associated veins formed. Tuffs appear to have a high concentrations of base metals and LREE, as such, mineralisation is anticipated to occur in this geological unit.

These fluids were possibly transported through structures, fractures and joints. Furthermore, hydrothermal brecciation possibly occurred when the fluid pressure exceeded the lithostatic pressure.

The tuffs appear to represent possible traps for these fluids as they are more porous and allow a longer fluids resident time compared to rhyolites; a longer fluid resident time can favour mineralisation. The trap sites of these fluids is anticipated to be disseminated as hydrofracturing often leads to “randomly” spaced hydrothermal systems associated with the differentiated granite (Figure 6.3). A discontinuous and disseminated brecciated mineralisation is to be expected from this hydrothermal system.

7 Conclusions

Based on field observations, petrography, SEM-EDX analysis and whole rock geochemistry, the following conclusions can be inferred:

- The Rooiberg Group magma was derived from partial melting of the continental crust by a melt related to the Bushveld Igneous Complex. The Schrikkloof Formation of the Rooiberg Group was emplaced in an intra-cratonic tectonic setting and deposited in a subaerial environment during explosive eruption events. The rocks formed in this environment are particularly rhyodacitic to rhyolitic in composition.
- Hydrothermal breccias are younger than the Schrikkloof Formation but older than the Waterberg Group and the source of these fluids is possibly provided by the differentiated granites of the Lebowa Granite Suite or the Rooiberg Group itself.
- The fluids pathways are characterised by hematite veins and hydrothermal breccias, hosted predominantly within tuffs. These fluids may have been propagated through hydrofracturing of the country rock. The composition of the host rock is quartz and K-feldspar rich, with minor sericite.
- Hematitised tuffs may have acted as possible trap as they are enriched in Pb-Zn and LREE compared to hydrothermal breccias and rhyolites. The detected ore minerals associated with hydrothermal breccias and hematitised tuffs are anglesite and monazite; the former commonly forms around oxidised ore deposits.

- The hydrothermal breccias are composed of hematite veins, as well as quartz and K-feldspar clasts. They are associated with Pb-Zn and LREE (monazite)

mineralisation. It is possible that this alteration is associated with a concealed Pb ore deposits, or it might an occurrence. This is suggested by the elevated Pb-Zn concentrations and the presents of anglesite in the upper Schrikkloof Formation.

8 References

Barker, O.B., Brandl, G., Callaghan, C. C., Eriksson, P.G., van der Neut, M., 2006. The Southpansberg and Waterberg Groups and the Blouberg Formation. *In*: Johnson, M.R., Anhaeusser, C.R. and Thomas, R.J. (Eds), *The Geology of South Africa*. Geological Society of South Africa, Johannesburg/Council for Geoscience, Pretoria, 301-318.

Buchanan P.C., Reimold, W.U., 1998. Studies of the Rooiberg Group, Bushveld Complex, South Africa: no evidence for an impact origin. *Earth and Planetary Science Letters*, **155**, 149-165.

Buchanan, P.C., Reimold, W.U., Koeberl, C., 1999. Petrogenesis of the Dullstroom Formation, Bushveld Magmatic Province, South Africa. *Contributions to Mineralogy and Petrology*, **137**, 133-146.

Buchanan, P.C., Reimold, W.U., Koeberl, C., Kruger, F.J., 2002. Geochemistry of intermediate to siliceous volcanic rocks of the Rooiberg group, Bushveld Magmatic Province, South Africa. *Contributions to Mineralogy and Petrology*, **144**, 131-143.

Buchanan, P.C., Reimold, W.U., Koeberl, C., Kruger, F.J., 2004. Rb-Sr and Sm-Nd isotopic compositions of the Rooiberg Group, South Africa: early Bushveld-related volcanism. *Lithos*, **29**, 373-388.

Buchanan, P.C., 2006. The Rooiberg Group. *In*: Johnson, M.R., Anhaeusser, C.R. and Thomas, R.J. (Eds), *The Geology of South Africa*. Geological Society of South Africa, Johannesburg/Council for Geoscience, Pretoria, 283-289.

Callaghan, C.C., Eriksson, P.G., Snyman, C.P., 1991. The sedimentology of the Waterberg Group in the Transvaal, South Africa: an overview. *Journal of African Earth Sciences*, **13**, 121-139.

Callaghan, C.C., 1993. The geology of the Waterberg Group in the southern portion of the Waterberg basin. *South Africa Geological Survey Bulletin*, **104**, 83 pp.

Cawthorn R.G., Walraven F., (1998) Emplacement and crystallization time for the Bushveld Complex. *Journal of Petrology*, **39 (9)**, 1669-1687.

Cawthorn, R.G., Eales, H.V., Walraven, F., Uken, R., Watkeys, M.K., 2006. The Bushveld Complex. *In*: Johnson, M.R., Anhaeusser, C.R., Thomas, R.J. (Eds), *The Geology of South Africa*. Geological Society of South Africa, Johannesburg/Council for Geoscience, Pretoria, 261-281.

Clarke, B., Uken, R., Reinhardt, J., 2009. Structural and compositional constraints on the emplacement of the Bushveld Complex, South Africa. *Lithos*, **111**, 21-26.

Coertze, F.J., Burger, A.J., Walraven, F., Marlow, A.G., MacCaskie, D.R., 1978. Field relations and age determinations in the Bushveld Complex. *Transactions of the Geological Society of South Africa*, **81**, 1-11.

Cohen, K.M., Finney, S.C., Gibbard, P.L., Fan, J. X., 2013; updated. The ICS International Chronostratigraphic Chart, Episodes **36**, 199-204.

Crocker I. T., Eales H. V., Ehlers D. I., 2001. Fluorite, Cassiterite and Sulphide Deposits Associated with the Acid Rocks of the Bushveld Complex. *Council for Geoscience*, *Memoir*, **90**, 151 pp.

Daly, R.A., Molengraaff, G.A.F., 1924. Structural Relations of the Bushveld Igneous Complex. *Transactions of the Geological Society of South Africa*, **32**, 1-35.

Fisher, R.V., 1966. Rocks composed of volcanic fragments and their classification. *Earth Science Reviews*, **1**, 287-298.

Fourie, P.J., 2000. The Vergenoeg fayalite iron oxide fluorite deposit, South Africa: some new aspects. *In*: Porter, T.M. (Ed.), Hydrothermal Iron Oxide Copper–Gold and Related Deposits a Global Perspective. Australian Mineral Foundation, Adelaide, pp. 309-320.

Fourie D., Harris C., 2011. O-isotope study of the Bushveld Complex granites and granophyres: constraints on source composition, and assimilation. *Journal of Petrology*, **52 (11)**, 2221-2242.

Goff, B.H., Weinberg, R., Groves, D.I., Veilreicher, N.M., Fourie, P.J., 2004. The giant Vergenoeg fluorite deposit in a magnetite–fluorite–fayalite REE pipe: a hydrothermally-altered carbonatite-related pegmatoid? *Mineralogy and Petrology*, **80**, 173-199.

Good, N., De Wit, M.J., 1997. The Thabazimbi-Murchison Lineament of the Kaapvaal Craton, South Africa: 2700 Ma of episodic deformation. *Journal of the Geological Society*, *London,* **154**, 93-97.

Grant, J.A., 1986. The Isocon diagram-A simple solution to Gresens' equation for metasomatic alteration. *Economic Geology*, **81**, 1976-1982.

Grant, J. A., 2005. Isocon analysis: A brief review of the method and applications. *Physics and Chemistry of the Earth*, **30**, 997-1004.

Graupner T., Mühlbach C., Schwarz-Schampera U., Henjes-Kunst F., Melcher F., Terblanche H., 2015. Mineralogy of high-field-strength elements (Y, Nb, REE) in the world-class Vergenoeg fluorite deposit, South Africa. *Ore Geology Reviews*, **64**, 583-601.

Gresens, P.L., 1967. Composition-volume relationships of metasomatism. *Chemical Geology*, **2**, 47-65.

Hall, A.L., 1932. The Bushveld Igneous Complex of the Central Transvaal. *Geological Survey of South Africa*, *Memoir*, **28**, 560 pp.

Hanson, R.E., Gose, W.A., Crowley, J.L., Ramezani, J., Bowring, S.A., Bullen, D.S., Hall, R.P., Pancake, J.A., Mukwakwami, J., 2004. Paleoproterozoic intraplate magmatism and basin development on the Kaapvaal Craton: Age, paleomagentism and geochemistry of 1.93 to 1.87 Ga post-Waterberg dolerites. *South African Journal of Geology*, **107**, 233-254.

Harmer, R.E., Farrow, D., 1995. An isotopic study on the volcanics of the Rooiberg Group: age implications and a potential exploration tool. *Mineralium Deposita*, **30**,188-195.

Hatton, C.J., 1995. Mantle plume origin for the Bushveld and Ventersdorp magmatic provinces. *Journal of African Earth Sciences*, **21 (3)**, 571-577

Hatton, C.J., Schweitzer, J.K., 1995. Evidence for synchronous extrusive and intrusive Bushveld magmatism. *Journal of African Earth Sciences*, **21 (4)**, 579-594.

Hou T., Charlier, B., Namur, O., Schütte, P., Schwarz-Schampera, U., Zhang, Z., Holtz, F., 2017. Experimental study of liquid immiscibility in the Kiruna-type

Vergenoeg iron–fluorine deposit, South Africa. *Geochimica et Cosmochimica Acta*, **203**, 303-322.

James, D.E., Fouch, M.J., VanDecar, J.C., van der Lee, S., Group, K.S., 2001. Tectospheric structure beneath southern Africa. *Geophysical Research Letters,* **28 (13)**, 2485-2488.

Jansen, H., 1982. The geology of the Waterberg basins in the Transvaal, Republic of South Africa. *Geological Survey of South Africa*, *Memoir*, **71**, 98pp.

Jébrak, M., 1997. Hydrothermal breccias in vein-type ore deposits; a review of mechanisms, morphology and size distribution. *Ore Geology Reviews*, **12**, 111-134.

Kinnaird, J.A., Kruger, F.J., Cawthorn, R.G., 2004. Rb–Sr and Nd–Sm isotopes in fluorite related to the granites of the Bushveld Complex. *South African Journal of Geology*, **107**, 413-430.

Klein, C., Dutrow, B., 2007. *The 23rd Edition of the Manual of Mineral Science*. John Wiley and Sons, Hoboken. 675pp.

Lenhardt, N., Eriksson, P.G., 2012. Volcanism of the Palaeoproterozoic Bushveld Large Igneous Province: the Rooiberg group, Kaapvaal Craton, South Africa. *Precambrian Research*. **214-215**, 82-94.

Lenhardt, N., Masango, S.M., Jolayemi, O.O., Lenhardt, S.Z, Peeters, G., Eriksson, P.G., 2017. The Palaeoproterozoic (~2.06 Ga) Rooiberg Group, South Africa: Dominated by extremely high-grade lava-like and rheomorphic ignimbrites?

New observations and lithofacies analysis. *Journal of African Earth Sciences*, **131**, 213-232.

Liu, X., Chen, F., Chang, H., Gao, J., Wu, P., Tan., J., 2022. The mineralization of Daxiao carbonate-hosted Pb-Zn deposit, northeast Yunnan province, SW China: Constraints from Rb-Sr isotopic dating and H–O–S-Pb isotopes. *Ore Geology Reviews*, **147**, 104956.

Martini, J.E.J., 1988. As-Zn mineralization associated with a Proterozoic geothermal system in the Rooiberg Group. *South African Journal of Geology*, **91 (3)**, 337-345.

Mathez, E.A., VanTongeren, J.A., Schweitzer, J., 2013. On the relationships between the Bushveld Complex and its felsic roof rocks, part 1: petrogenesis of Rooiberg and related felsites. *Contributions to Mineralogy and Petrology*, **166**, 435-449.

Mellor, E.T., 1905. Evidence of Contemporaneous Volcanic Action in the Lower Portion of the Waterberg Formation. *Transactions of the Geological Society of South Africa*, **8**, 38-41.

Pearce, J.A., Harris, N.B.W, Tindle, A.G., 1984. Trace element discrimination diagrams for the tectonic interpretation of granitic rocks. *Journal of Petrology*, **25 (4)**, 956-983.

Rajesh, H.M., Mokatse, T., Wan, Y., 2020. Complexity of characterizing mafic-ultramafic remnants of Archean layered complexes in high-grade terranes: the scenario from Motloutse complex, south-western Zimbabwe craton. *Lithos*, **105255,** 352-353.

Rhodes, R.C., 1975. New Evidence for Impact Origin of the Bushveld Complex, South Africa. *Geology*, **3**, 549-554.

Robb, L.J., Freeman, L.A., Armstrong, R.A., 2000. Nature and longevity of hydrothermal fluid flow and mineralisation in granites of the Bushveld Complex, South Africa. *Transactions of the Royal Society of Edinburgh: Earth Sciences*, **91**, 269-281.

Robb, L.J., 2005. *Introduction to ore forming processes*. Blackwell Publishing, Oxford. 373pp.

Rudnick, R.L., 1990. Restites, Eu anomalies, and the lower continental crust. Geochimica et Cosmochimica Acta, **56(3)**, 963-970.

Rudnick, R.L., Gao, S., 2003. Composition of the continental crust. Chapter 3, *In Treatise on Geochemistry*, 1-64.

Schweitzer, J. K., Hatton, C. J., 1995. Chemical Alteration within the volcanic roof rocks of the Bushveld Complex. *Economic Geology*, **90**, 2218-2231.

Schweitzer, J.K., Hatton, C.J. and de Waal, S.A., 1995a. Regional lithochemical stratigraphy of the Rooiberg Group, upper Transvaal Supergroup: a proposed new subdivision. *South African Journal of Geology*, **98**, 245-255.

Schweitzer, J. K., Hatton, C. J., de Waal, S. A., 1995b. Economic potential of the Rooiberg Group: volcanic rocks in the floor and roof of the Bushveld Complex. *Mineralium Deposita*, **30 (2)**, 168-177.

Schweitzer, J. K., Hatton, C. J., de Waal, S. A., 1997. Link between the granitic and volcanic rocks of the Bushveld Complex, South Africa. *Journal of African Earth Sciences*, **24 (1)**, 95-104.

Sergeev, N., Burlow, R., Tessalina, S., 2017. The Paroo Station Mine supergene lead deposits, Western Australia: Geological and geochemical constraints. *Ore Geology Reviews*, **80**, 564-593.

Sun, S.S., McDonough, W.F., 1989. Chemical and isotopic systematics of oceanic basalts; implications for mantle composition and processes. *Geological Society, London, Special Publications*, **42**, 313-345.

Twist, D., French, B.M., 1983. Voluminous acid volcanism in the Bushveld Complex: a review of the Rooiberg felsite. *Bulletin of Volcanology,* **46**, 225-242.

Twist, D., 1985. Geochemical evolution of the Rooiberg silicic lavas in the Loskop Dam area, South-eastern Bushveld. *Economic Geology*, **80**, 1153-1165.

VanTongeren, J.A., Mathez, E.A., Kelemen, P.B., 2010. A felsic end to Bushveld Differentiation. *Journal of Petrology*, **51 (9)**, 1891-1912.

VanTongeren, J.A., Mathez, E.A., 2013. Incoming magma composition and style of recharge below the pyroxenite marker, Eastern Bushveld Complex, South Africa. *Journal of Petrology*, **54**, 1585-1605.

VanTongeren, J.A., Mathez, E.A., 2015. On the relationships between the Bushveld Complex and its felsic roof rocks, part 2: the immediate roof. *Contributions to Mineralogy and Petrology*, **170**, 56.

VanTongeren, J.A., Zirakparvar, N.A., Mathez, E.A., 2016. Hf isotopic evidence for a cogenetic magma source for the Bushveld Complex and associated felsic magmas. *Lithos*, **248**, 469-477.

Verhaert, M., Bernard, A., Dekoninck, A., Lafforgue, L., Saddiqi, O., Yans, J., 2017. Mineralogical and geochemical characterization of supergene Cu–Pb–Zn–V ores in the Oriental High Atlas, Morocco. *Mineralium Deposita*, **52**,1049-1068.

Von Gruenewaldt, G., Harmer, R.E., 1992. Chapter 5 Tectonic Setting of Proterozoic Layered Intrusions with Special Reference to the Bushveld Complex. *Developments in Precambrian Geology*, **10**, 181-213.

Walraven, F., Hattingh, E., 1993. Geochronology of the Nebo granite, Bushveld Complex. *South African Journal of Geology*, **96**, 31-41.

Walraven, F., 1997. Geochronology of the Rooiberg Group, Transvaal Supergroup, South Africa. *Economic Geology Research Unit. University of Witwatersrand, Johannesburg, Information Circular*, **316**, 21pp.

Willemse, J., 1969. The Geology of the Bushveld Igneous Complex, the Largest Repository of Magmatic Ore Deposits in the World. *Economic Geology Monograph*, **4**, 1-22.

Winchester, J.A., Floyd, P.A., 1977. Geochemical discrimination of different magma series and their differentiation products using immobile elements. *Chemical Geology*, **20**, 325-343.

Winter, J.D., 2014. Principles of Igneous and Metamorphic Petrology. *Pearson New International Edition*, 739pp.

Zeh, A., Jaguin, J., Poujol, M., Boulvais, P., Hallot, E., Block, S., Paquette, J. L., 2013. Juvenile crust formation in the north eastern Kaapvaal Craton at 2.97 Ga-implications for Archean terrane accretion, and the source of the Pietersburg gold. *Precambrian Research*, **233**, 20-43.

Zeh, A., Ovtacharova, M., Wilson, A.H., Schaltegger, U., 2015. The Bushveld Complex was emplaced and cooled in less than one million years – results of zirconology, and geotectonic implications. *Earth and Planetary Science Letters*, **418**, 103-114.

Appendix 1: Rock types and coordinates

Table A1.1 below indicates the sample ID of the various rock types as well as their coordinates. The coordinates (Table A1.1) are in decimal degrees (DD) and were plotted on the "*WGS 1984*" spheroid of the "*Hartebeesthoek 1994*" coordinate system on ArcGIS 10.4.1.

Table A1.1: Rock types and coordinates of samples and their respective analysis.

Sample ID	Rock type	Longitude (DD)	Latitude (DD)	XRF	ICP-MS	Thin Section
Sample 07	Rhyolite	28.428414°	-24.607131°	1	1	1
Sample 12	Rhyolite	28.454617°	-24.617260°	1	1	1
Sample 13	Rhyolite	28.453811°	-24.617073°	1	1	
Sample 23	Rhyolite	28.444625°	-24.614350°	1	1	
Sample 25	Rhyolite	28.442427°	-24.611293°	1	1	1
Sample 26	Rhyolite	28.447418°	-24.607805°	1	1	1
Sample 31	Rhyolite	28.454906°	-24.620599°	1	1	1
Sample 44	Rhyolite	28.439198°	-24.610128°	1	1	
Sample 05	Tuff	28.430065°	-24.604107°	1	1	
Sample 11	Tuff	28.453015°	-24.620173°	1	1	
Sample 14	Tuff	28.452261°	-24.615519°	1	1	1
Sample 18	Tuff	28.449140°	-24.614588°	1	1	
Sample 27	Tuff	28.439404°	-24.608667°	1	1	
Sample 29	Tuff	28.439833°	-24.611246°	1	1	
Sample 32	Tuff	28.453749°	-24.617766°	1	1	
Sample 35	Tuff	28.463221°	-24.624133°	1	1	
Sample 36	Tuff	28.463520°	-24.623855°	1	1	1
Sample 43	Tuff	28.439203°	-24.610133°	1	1	
Sample 09	Hydrothermal Breccia	28.428671°	-24.606959°	1	1	1
Sample 15	Hydrothermal Breccia	28.452007°	-24.616103°	1	1	1
Sample 16	Hydrothermal Breccia	28.451043°	-24.615844°	1	1	
Sample 17	Hydrothermal Breccia	28.449965°	-24.615446°	1	1	
Sample 19	Hydrothermal Breccia	28.449039°	-24.614678°	1	1	1
Sample 20	Hydrothermal Breccia	28.448932°	-24.614265°	1	1	
Sample 21	Hydrothermal Breccia	28.449067°	-24.614153°	1	1	
Sample 24	Hydrothermal Breccia	28.443767°	-24.612492°	1	1	
Sample 30	Hydrothermal Breccia	28.454886°	-24.620564°	1	1	
Sample 45	Hydrothermal Breccia	28.449105°	-24.614420°	1	1	1
Sample 46	Hydrothermal Breccia	28.461773°	-24.625413°	1	1	
Sample 121	Hydrothermal Breccia	28.455069°	-24.616932°	1	1	
Sample 08	Vein	28.428651°	-24.606977°	1	1	1

Appendix 2: SEM-EDX Spectrum Atlas

This section depicts all spectrum for Figure 5.1 – 5.4. Each Figure is followed by spectrum analysis which indicates the minerals associated with each spot analysis.

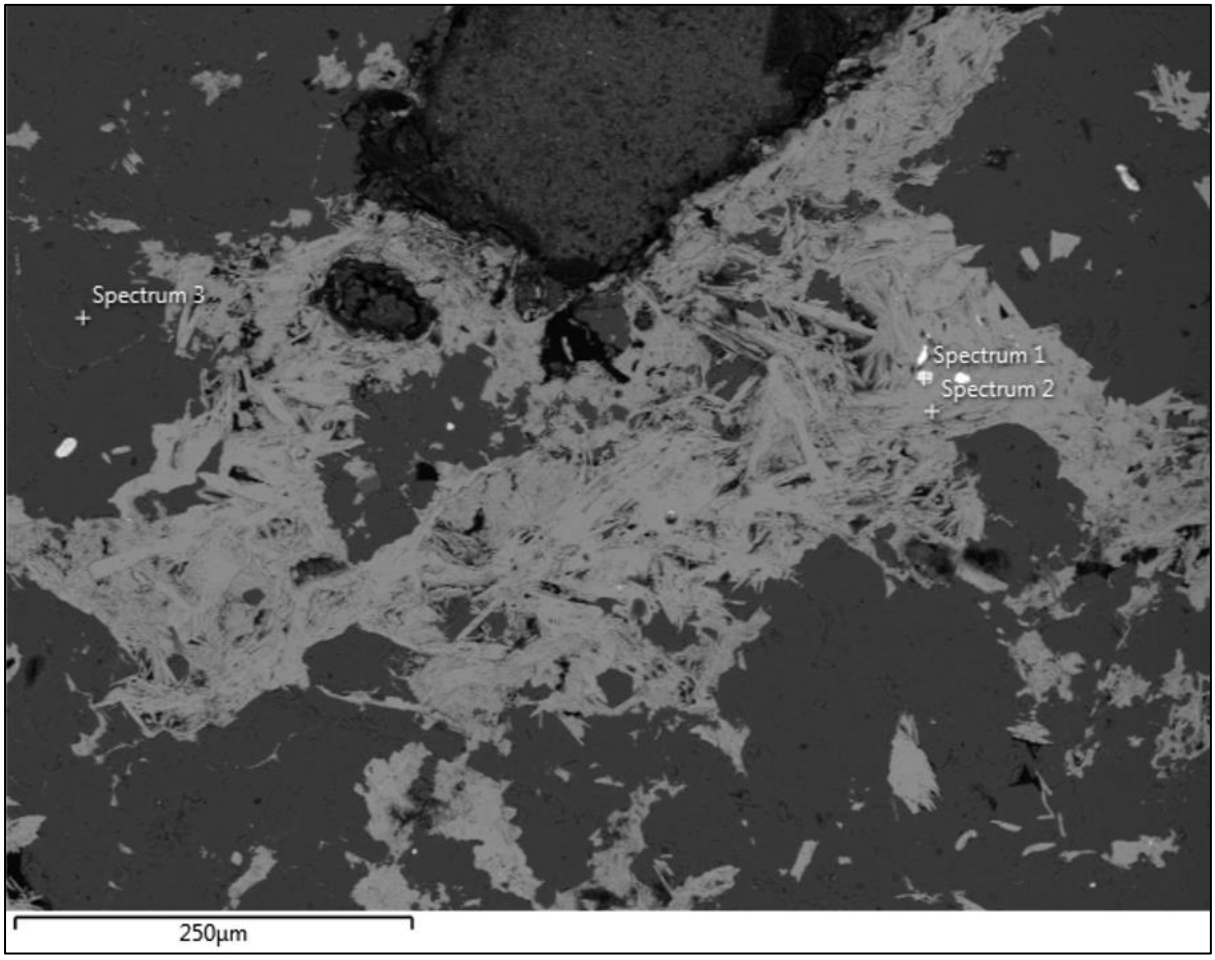

Figure A2.1: A BSE image of Sample 19, Figure 5.1a, showing the location of SEM-EDX analysis spectrums 1 – 3. The detailed spot analysis of each spectrum is indicated below on Figures A2.2 – A 2.4, respectively.

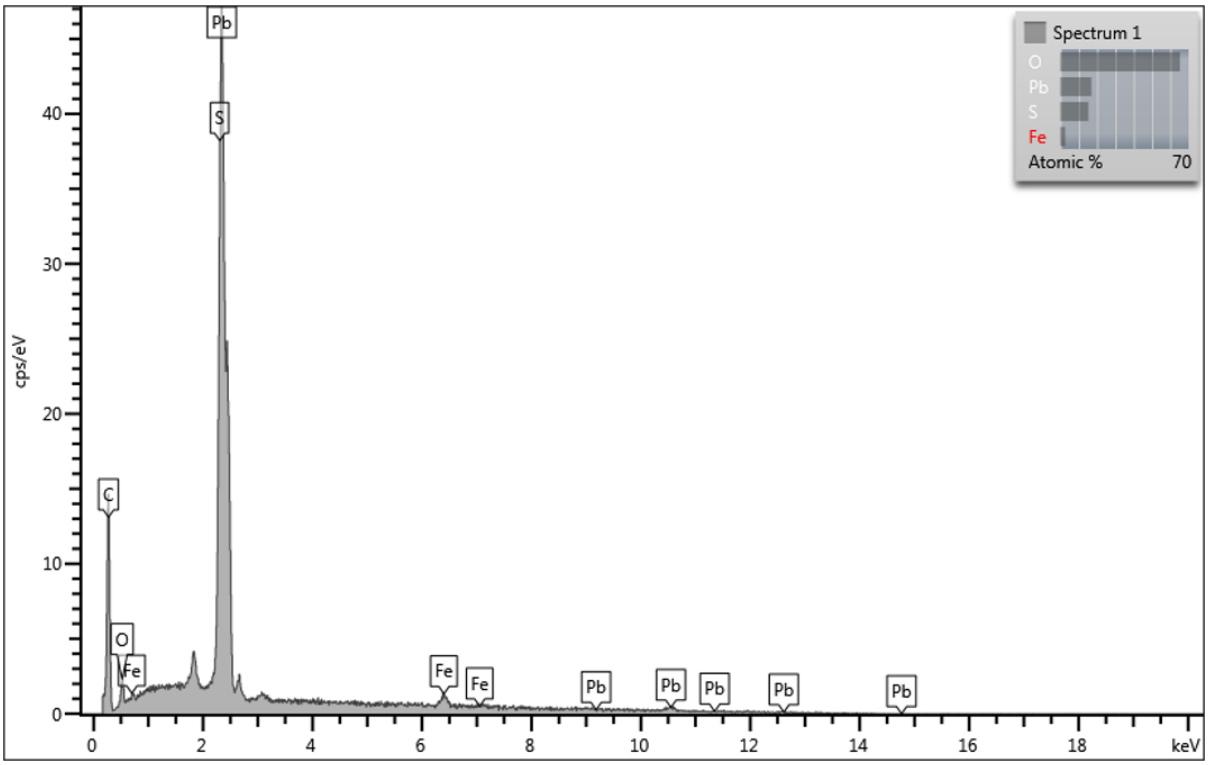

Figure A2.2: Spectrum 1; anglesite ($PbSO_4$) with minor Fe impurities.

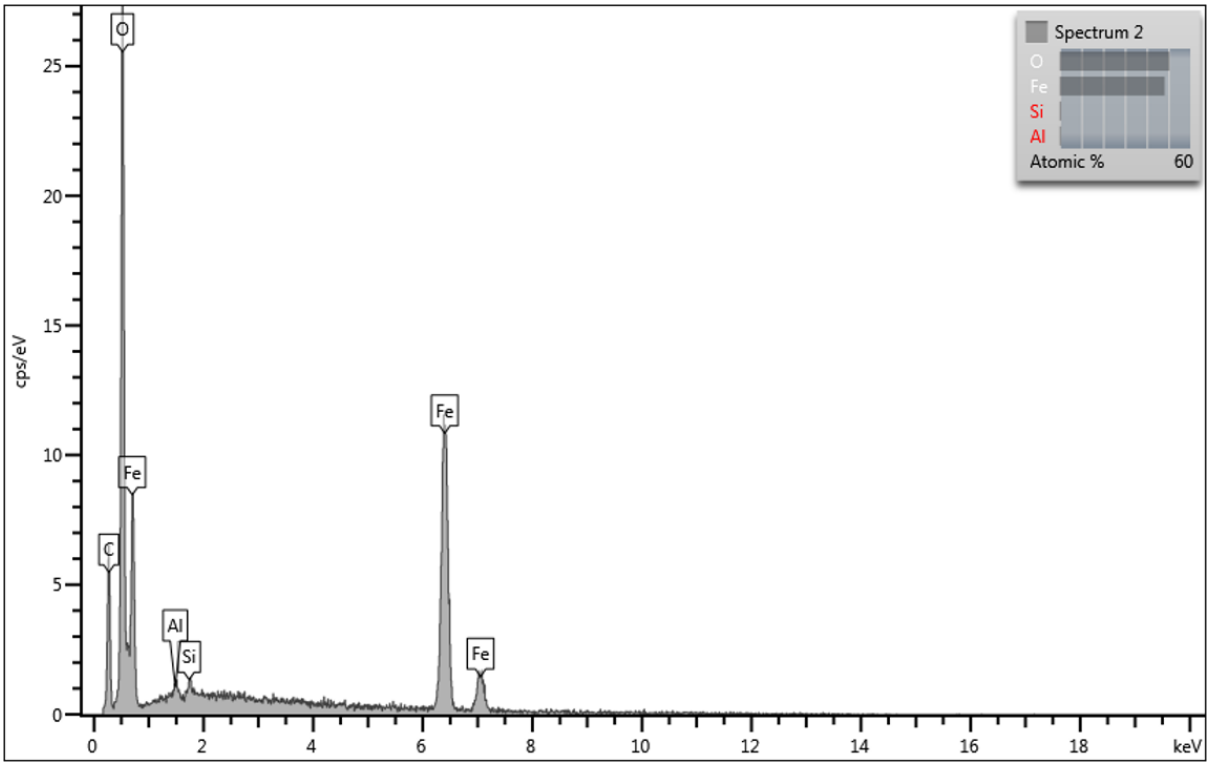

Figure A2.3: Spectrum 2; hematite (Fe_2O_3) with Si and Al impurities.

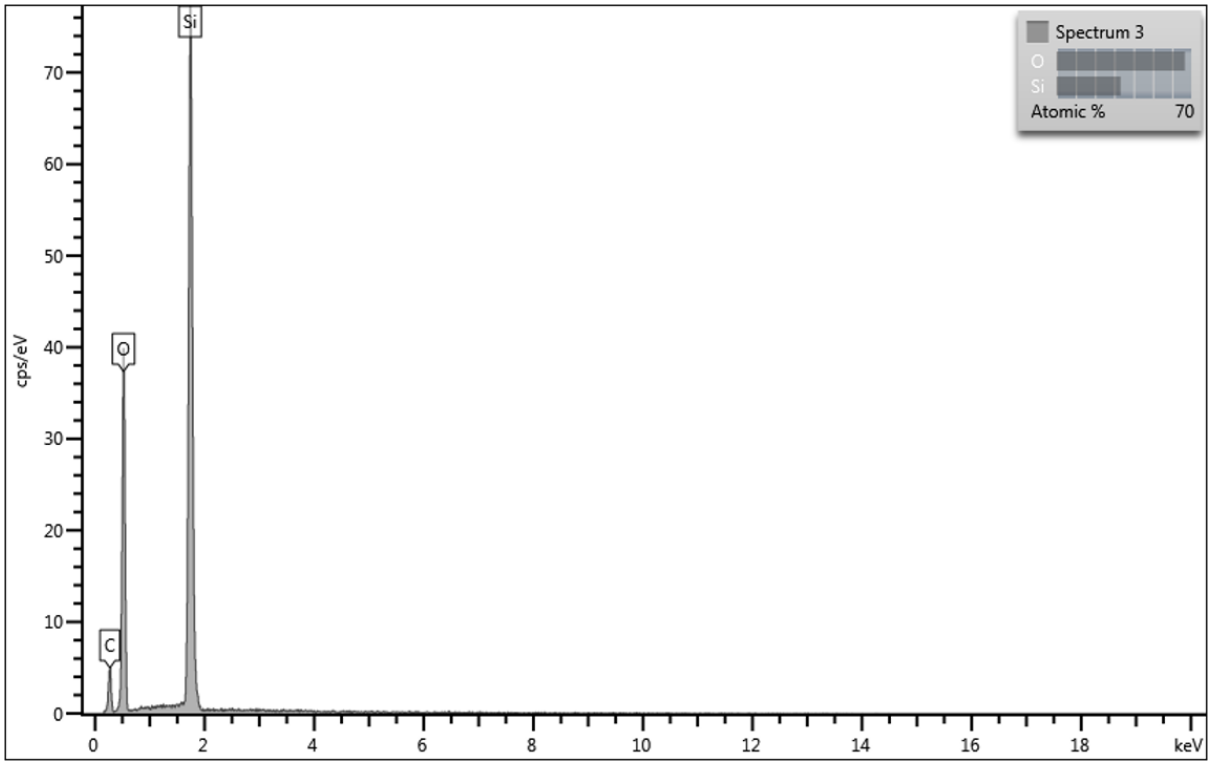

Figure A2.4: Spectrum 3; quartz (SiO_2).

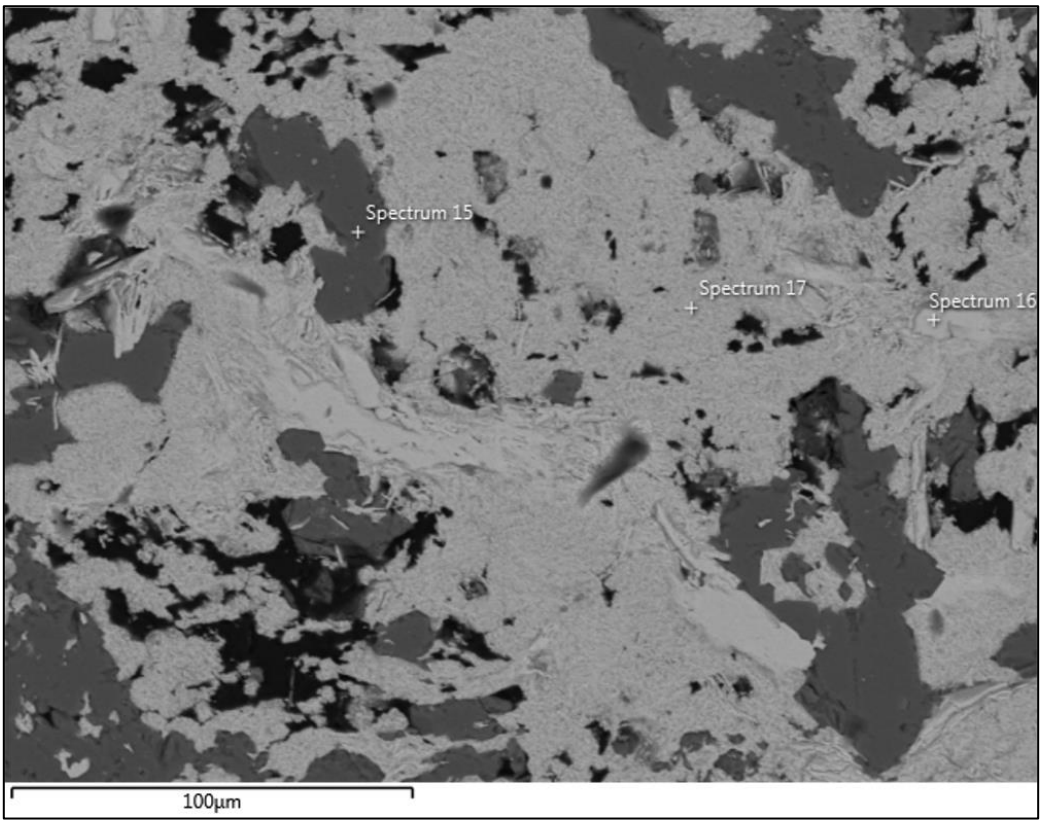

Figure A2.5: A second BSE image acquired from Sample 19, Figure 5.1b, showing the location of SEM-EDX analysis spectrums 15 – 17. The detailed spot analysis of each spectrum is indicated below on Figures A2.6 – A2.8.

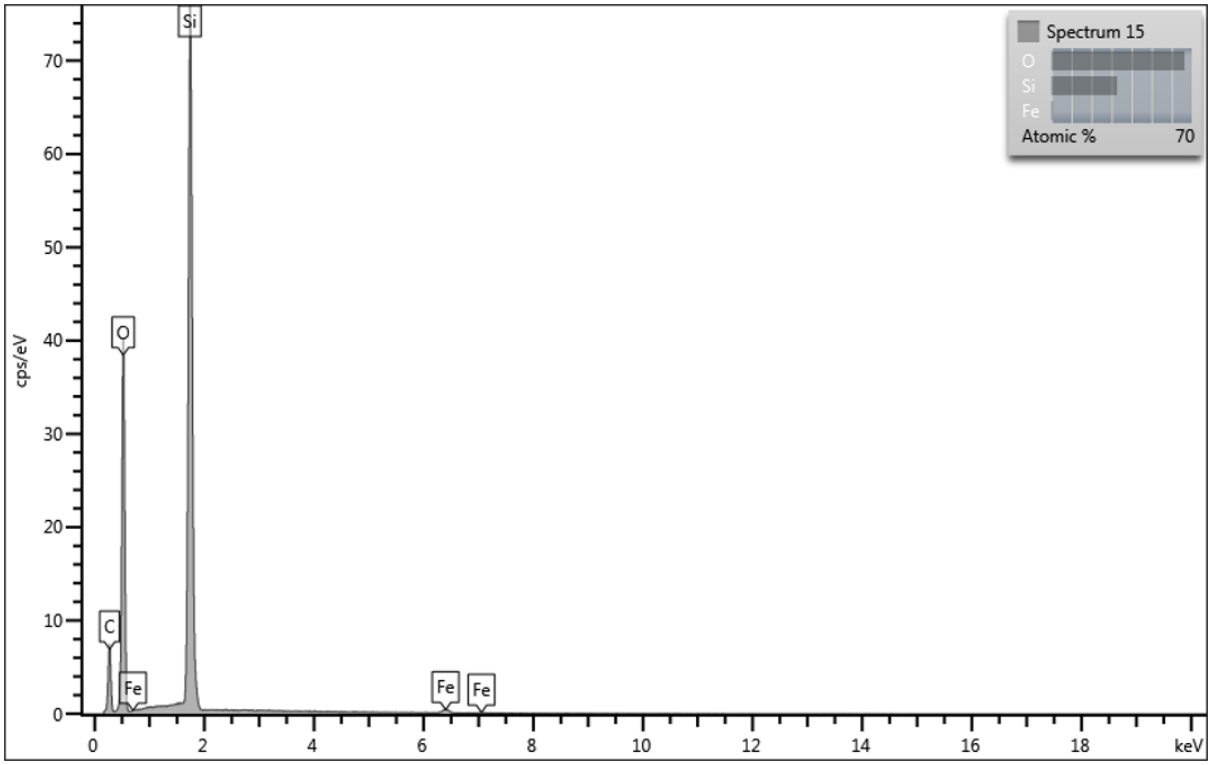

Figure A2.6: Spectrum 15; quartz (SiO_2) with Fe impurities.

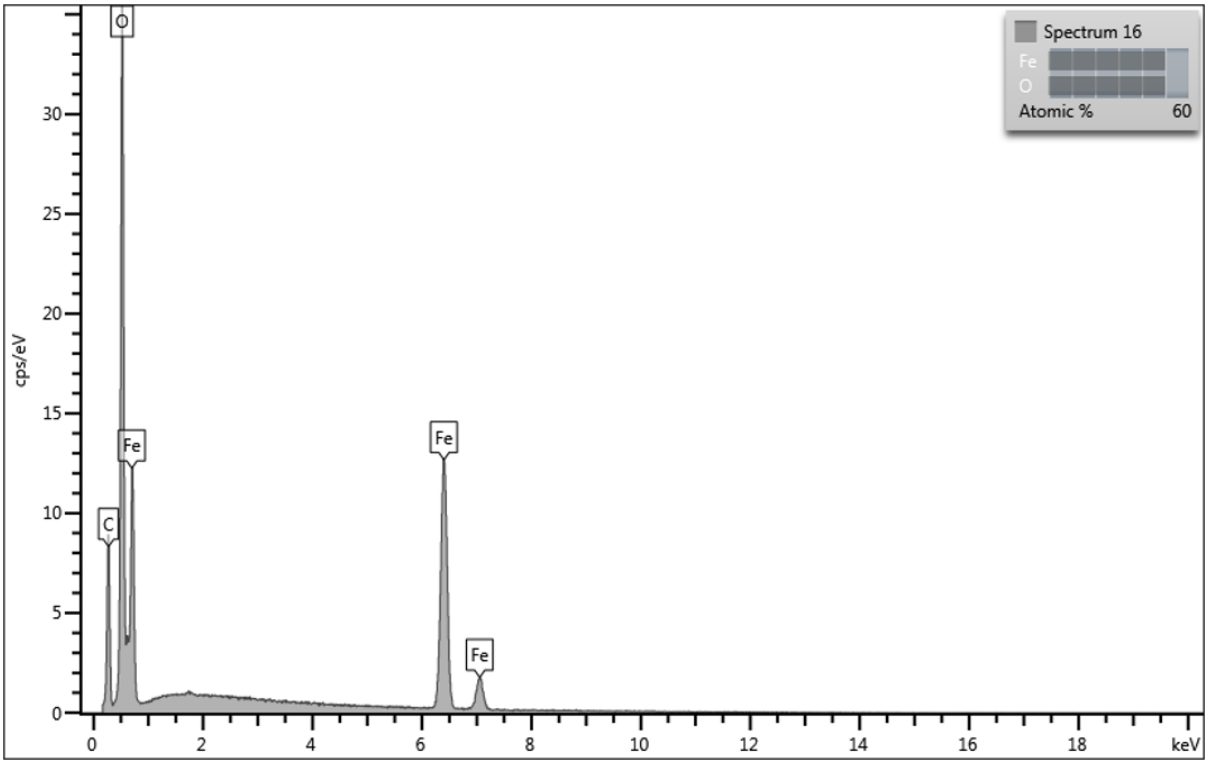

Figure A2.7: Spectrum 16; hematite (Fe_2O_3).

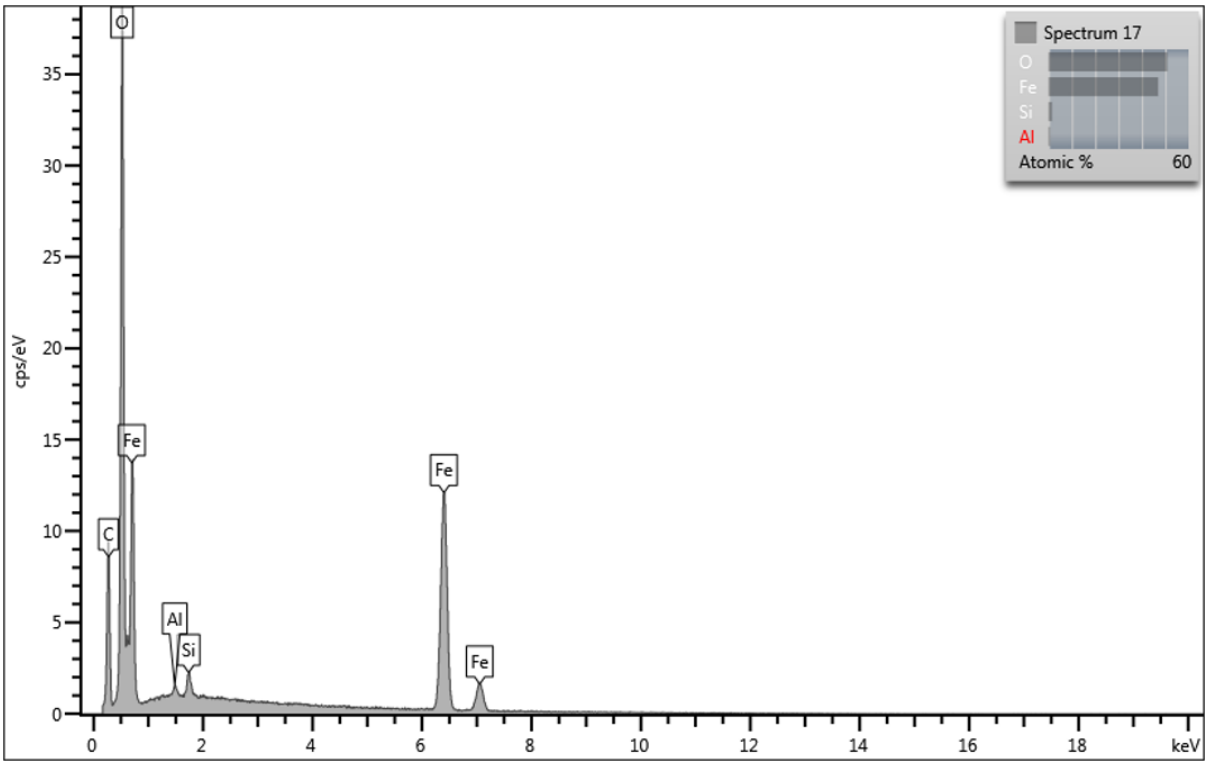

Figure A2.8: Spectrum 17; hematite (Fe_2O_3) with Si and Al impurities.

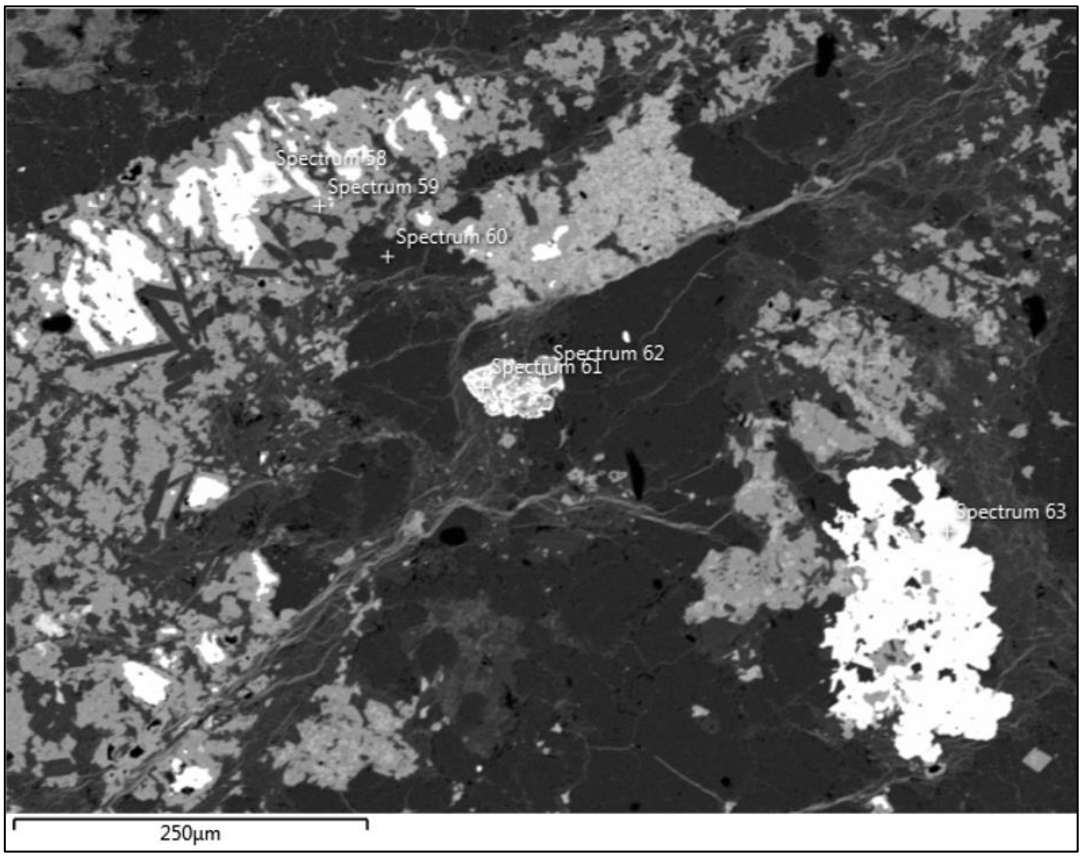

Figure A2.9: A BSE image of Sample 36, Figure 5.2, showing the location of SEM-EDX spectrums 58 – 63. The detailed spot analysis of each spectrum is indicated below on Figures A2.10 – A2.15.

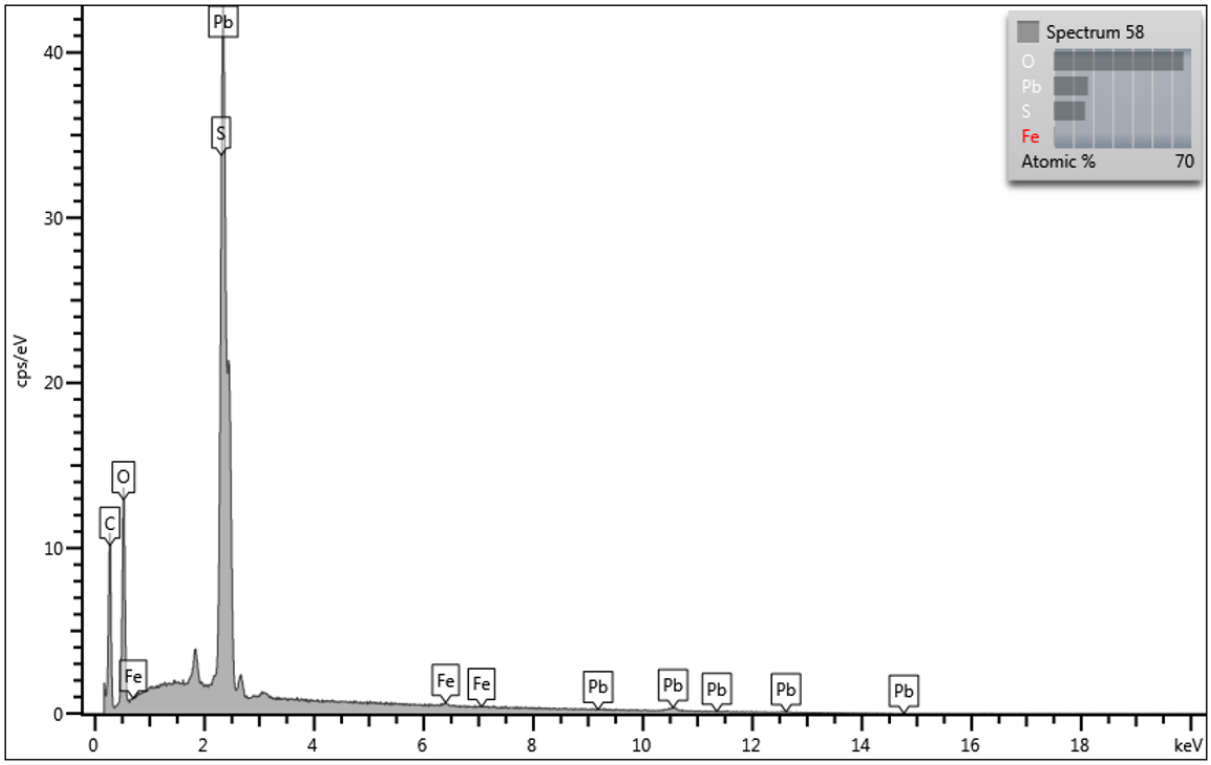

Figure A2.10: Spectrum 58; anglesite ($PbSO_4$) with Fe impurities.

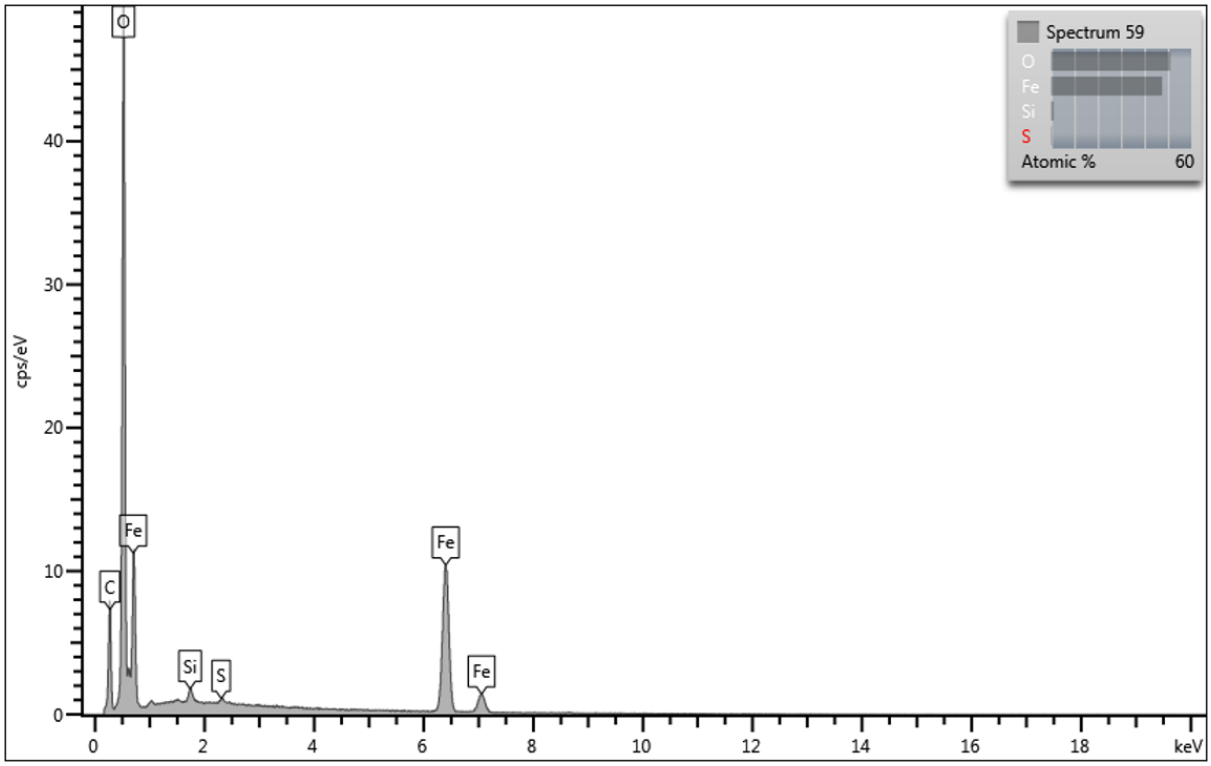

Figure A2.11: Spectrum 59; hematite (Fe_2O_3) with minor S (as well as Si impurities).

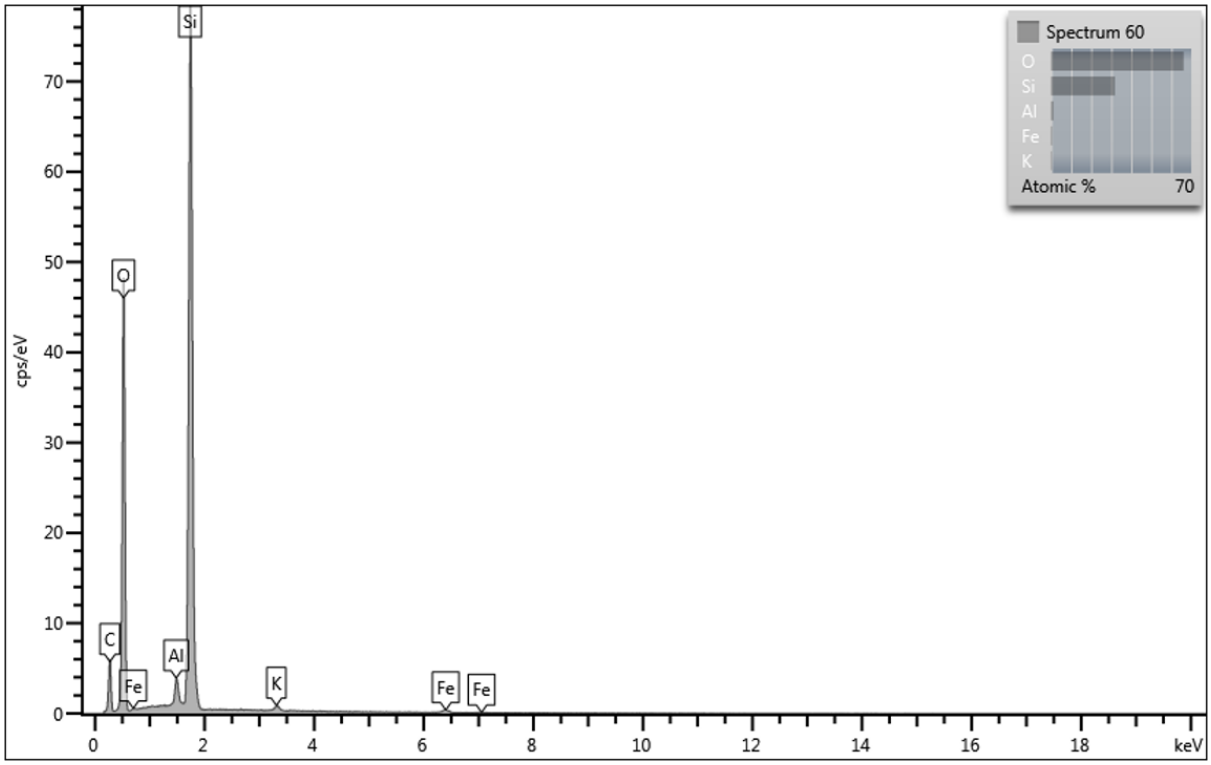

Figure A2.12: Spectrum 60; quartz (SiO_2) with Al, Fe and K impurities.

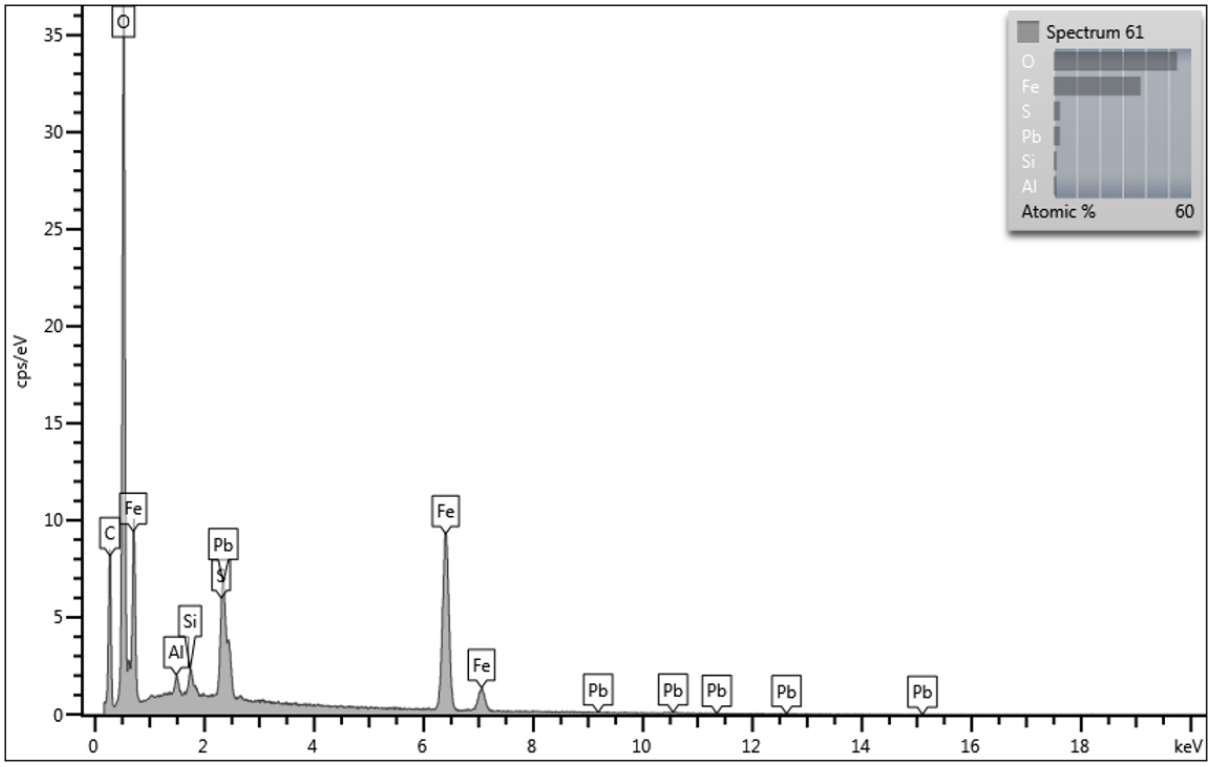

Figure A2.13: Spectrum 61; hematite (Fe_2O_3) with Si and Al impurities, furthermore, possibly has anglesite ($PbSO_4$) inclusions.

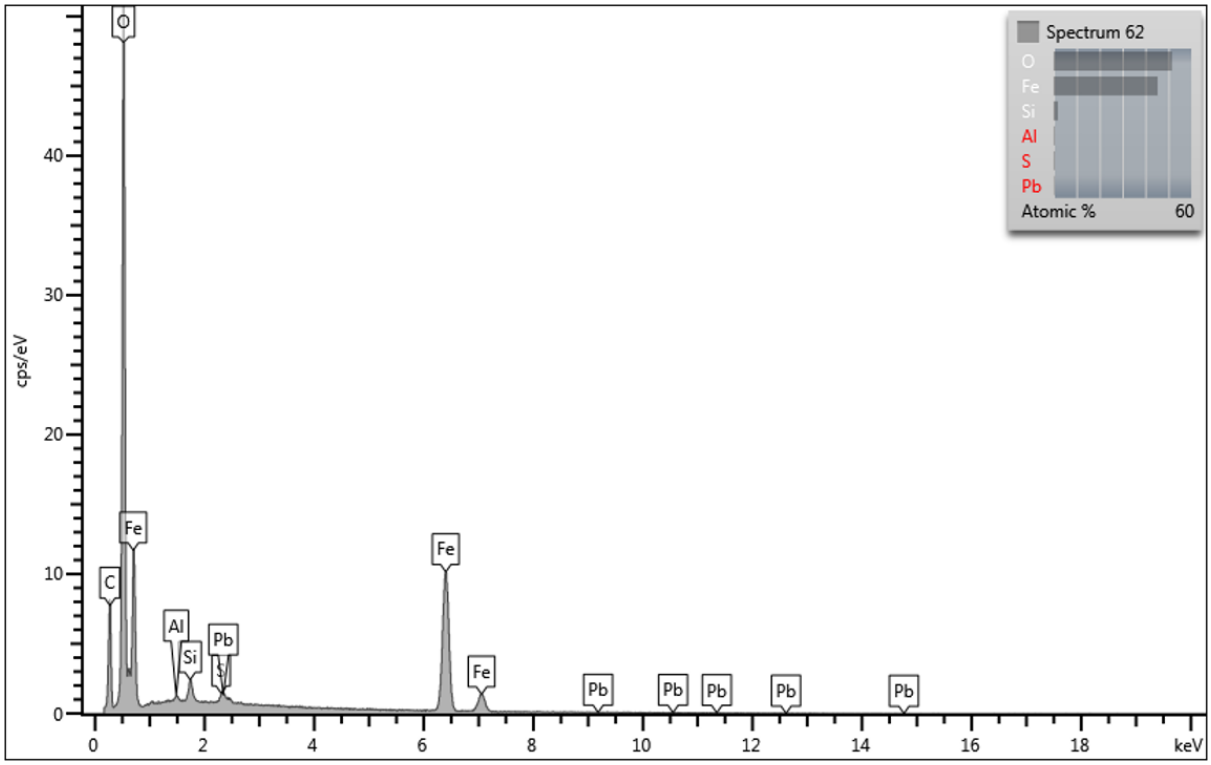

Figure A2.14: Spectrum 62; hematite (Fe_2O_3) with Si as well as Al impurities, furthermore, possible has anglesite ($PbSO_4$) inclusions.

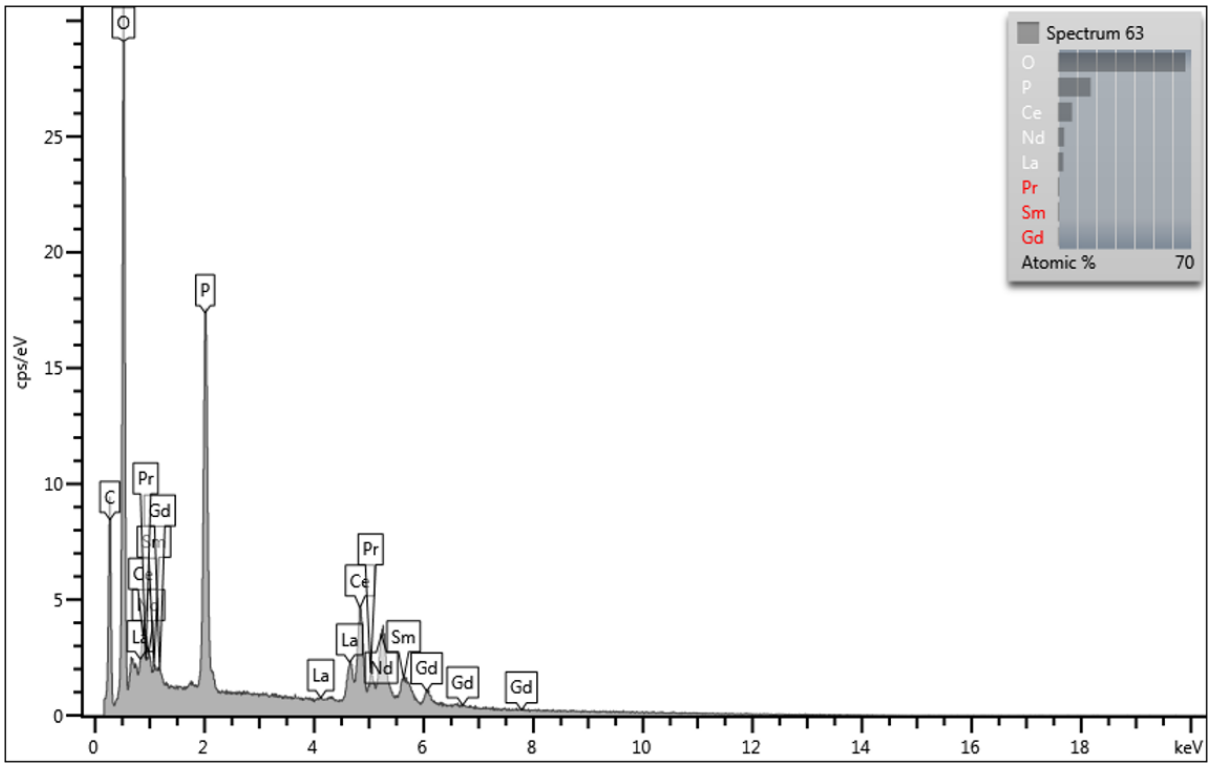

Figure A2.15: Spectrum 63; monazite ($(Ce,Nd,La)PO_4$).

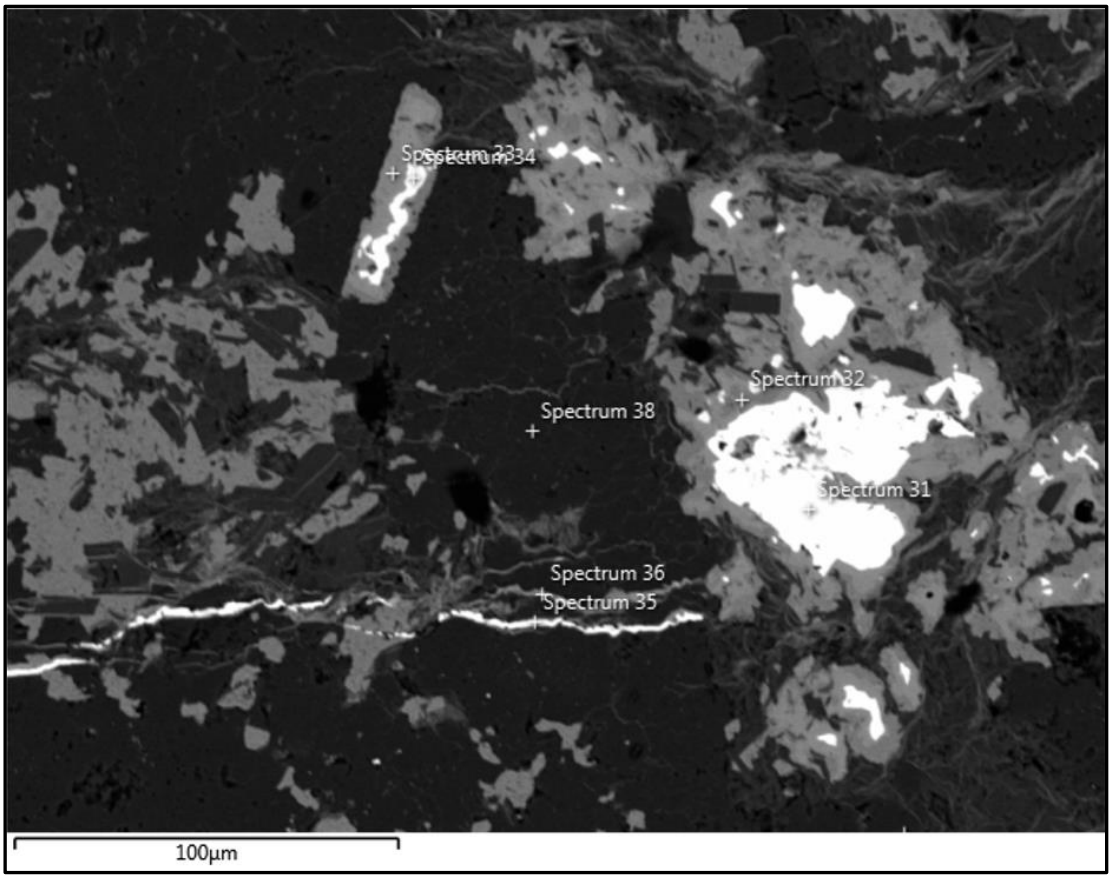

Figure A2.16: A second BSE image acquired from Sample 36, Figure 5.3a, showing the location of SEM-EDX spectrums 31 – 36 and 38. The detailed spot analysis of each spectrum is indicated on Figures A2.17 – A2.22 and A2.23, respectively.

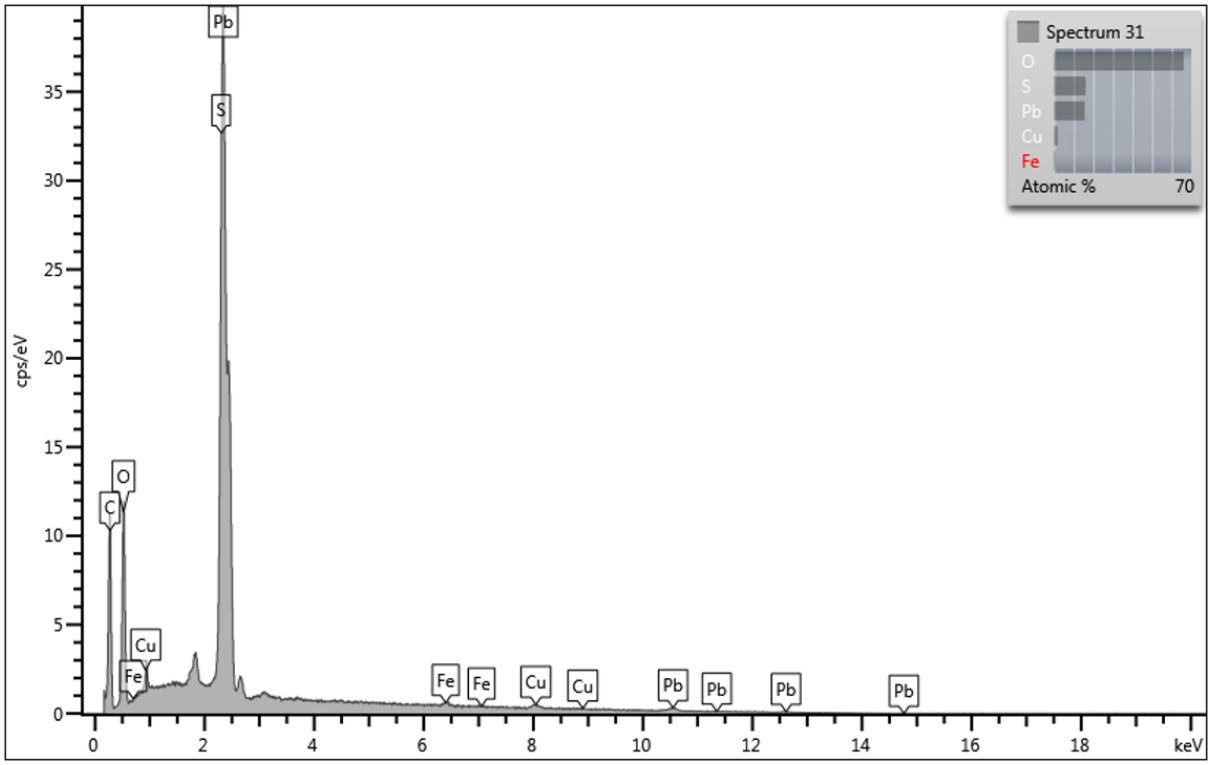

Figure A2.17: Spectrum 31; anglesite ($PbSO_4$) with minor Cu and Fe

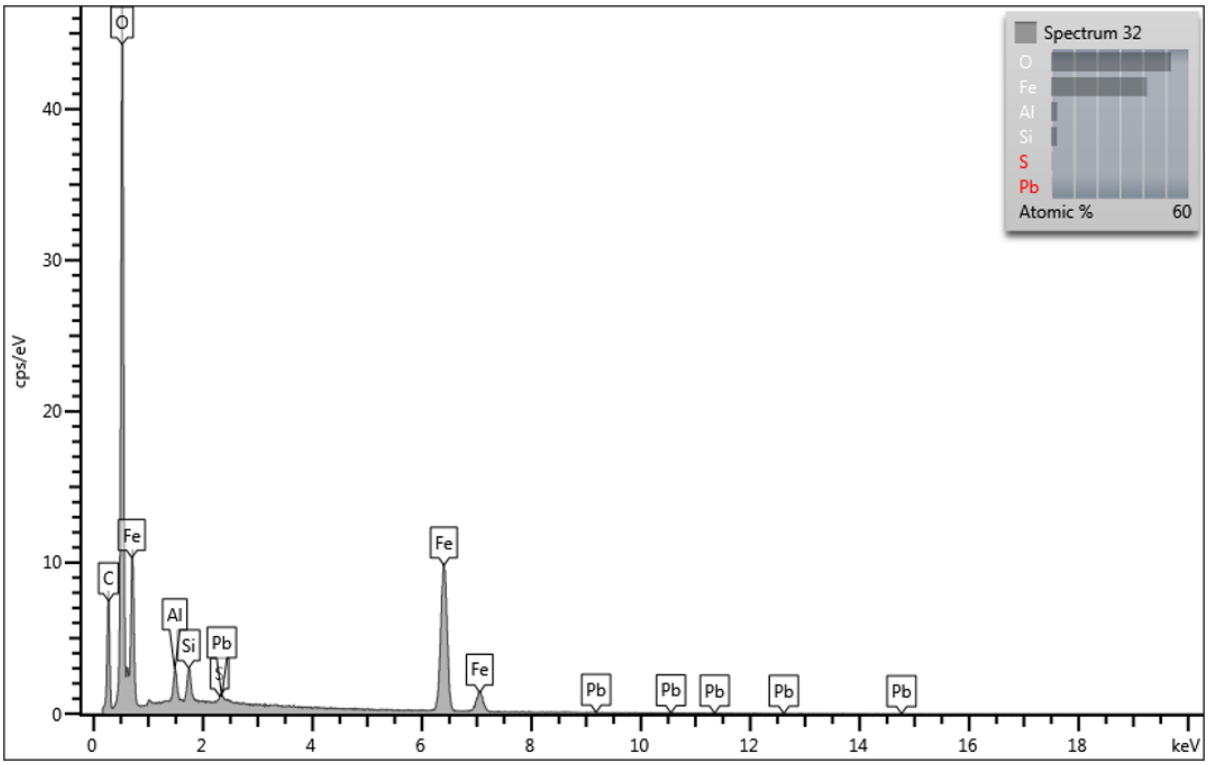

Figure A2.18: Spectrum 3; hematite (Fe_2O_3) with minor Al, Si, S and Pb impurities.

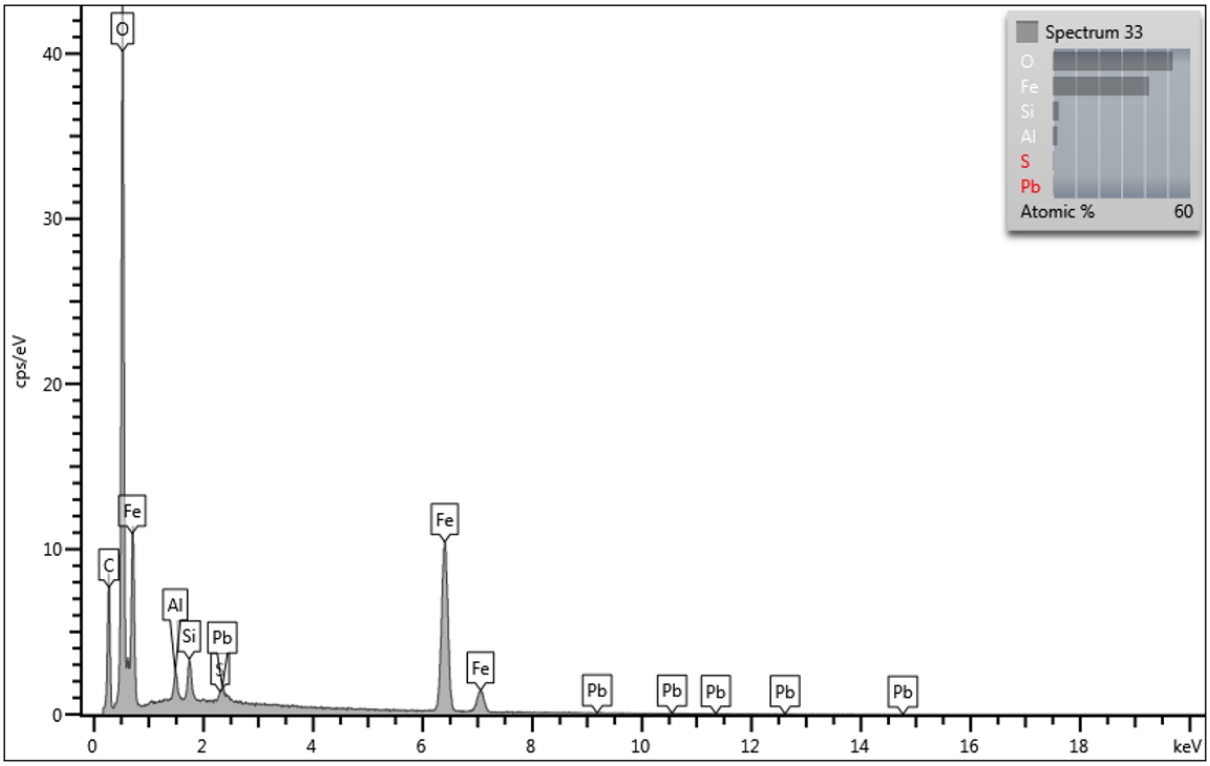

Figure A2.19: Spectrum 33; hematite (Fe_2O_3) with minor S as well as Si, Al and Pb impurities.

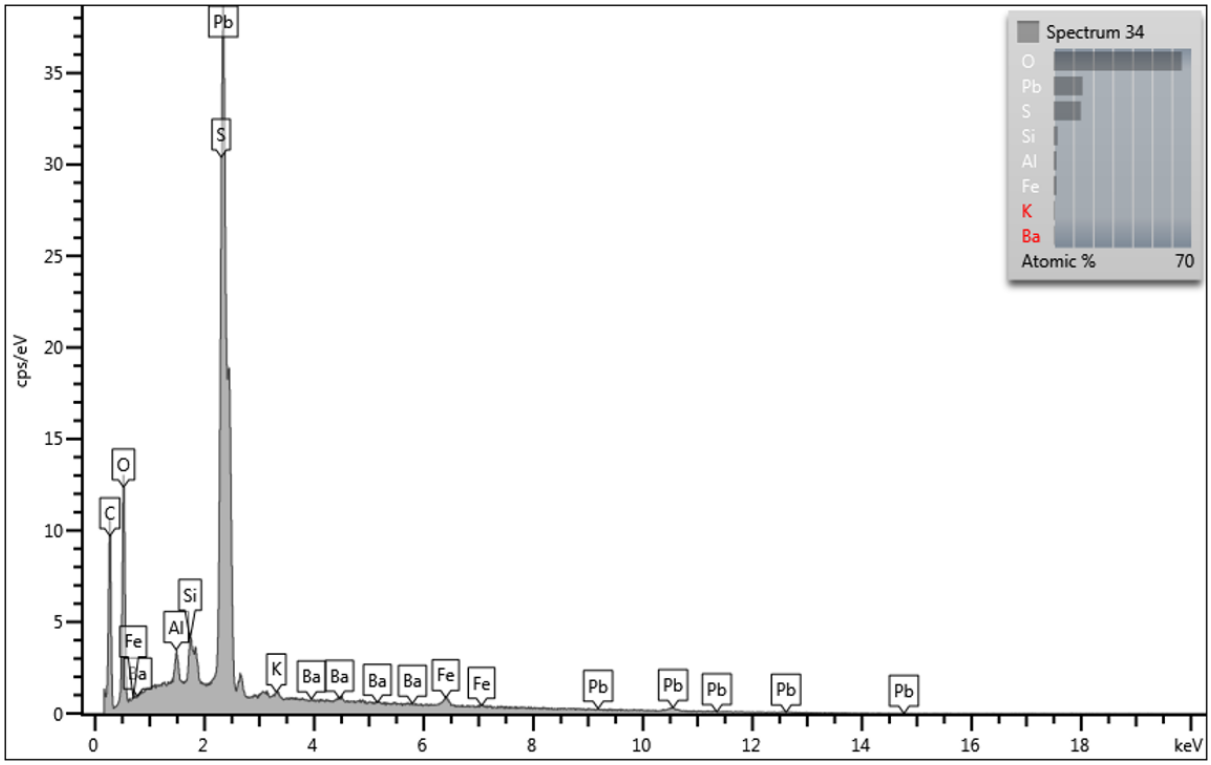

Figure A2.20: Spectrum 34; anglesite ($PbSO_4$) with Si, Al, Fe, K and Ba impurities.

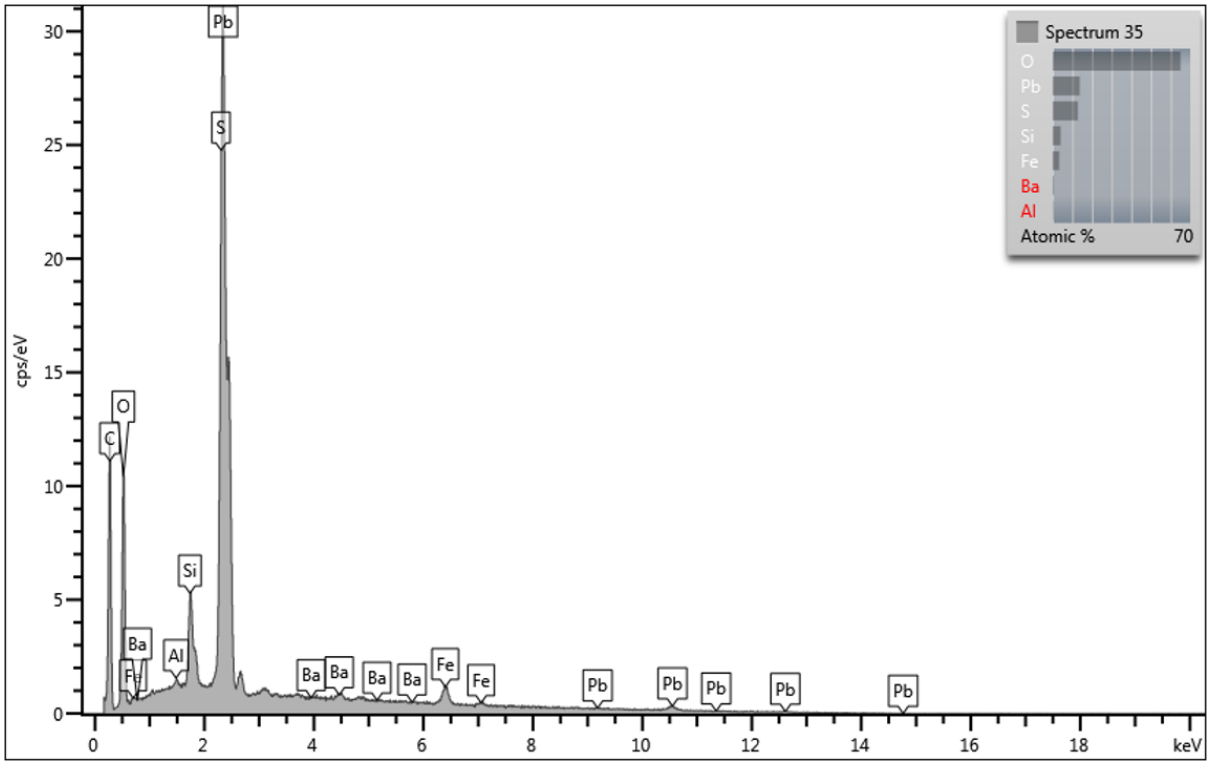

Figure A2.21: Spectrum 35; anglesite ($PbSO_4$) with Si, Fe, Ba and Al impurities.

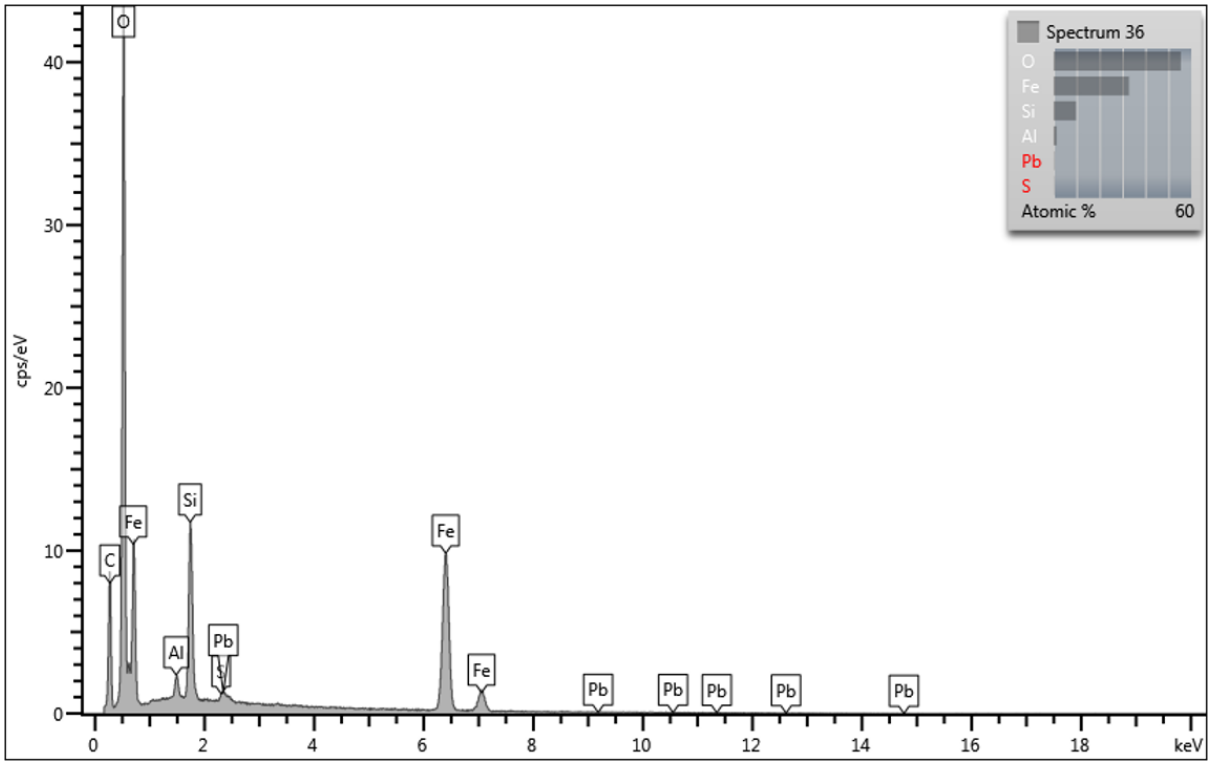

Figure A2.22: Spectrum 36; chlorite ($(Fe_5Al)(Si_3,Al)O_{10}(OH)_8$) with Pb and S impurities.

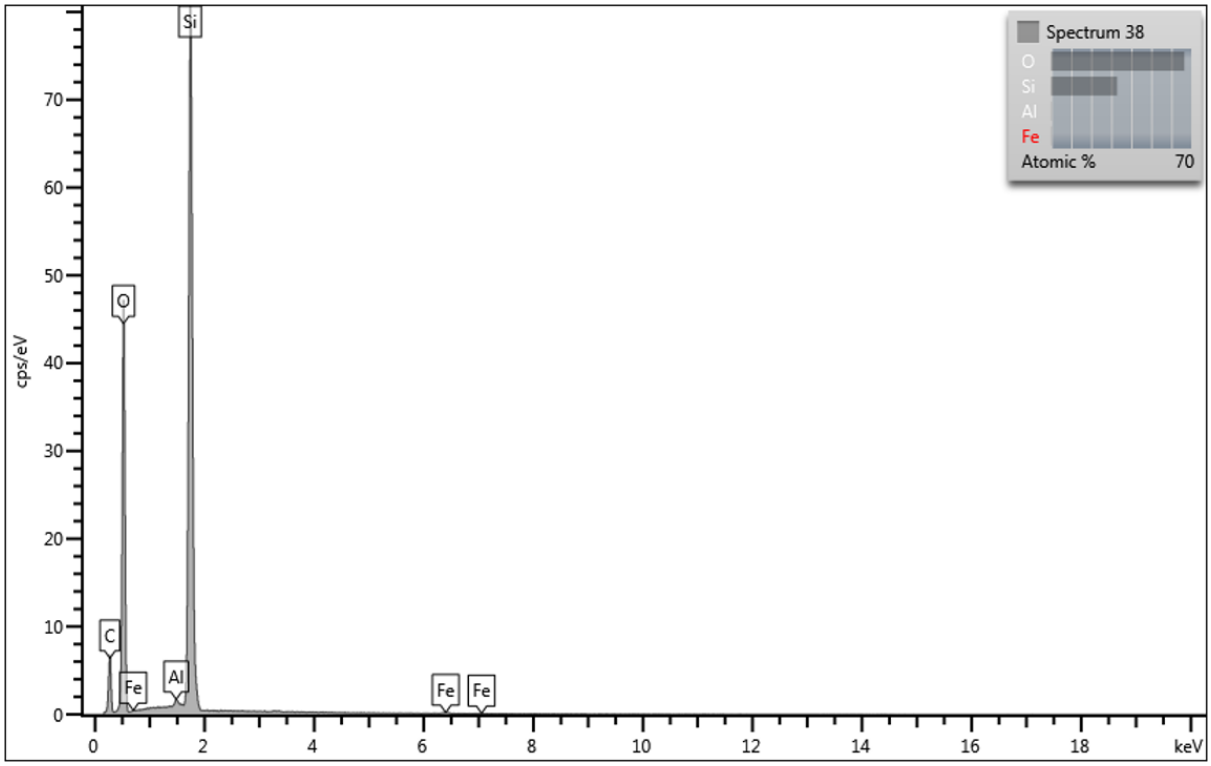

Figure A2.23: Spectrum 38; quartz (SiO_2) with minor Al and Fe impurities.

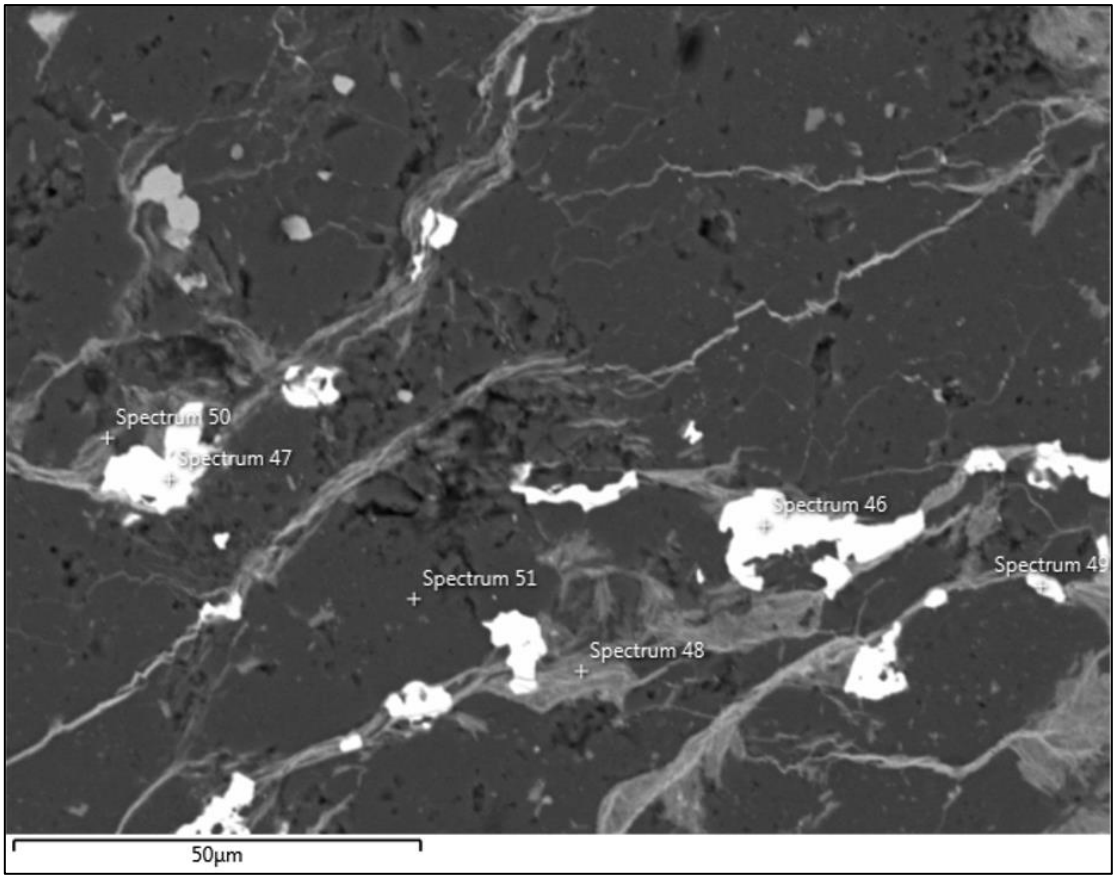

Figure A2.24: A third BSE image acquired from Sample 36, Figure 5.3b, showing the location of SEM-EDX spectrums 46 – 51. The detailed spot analysis of each spectrum is indicated below on Figure A2.25 – A2.30, respectively.

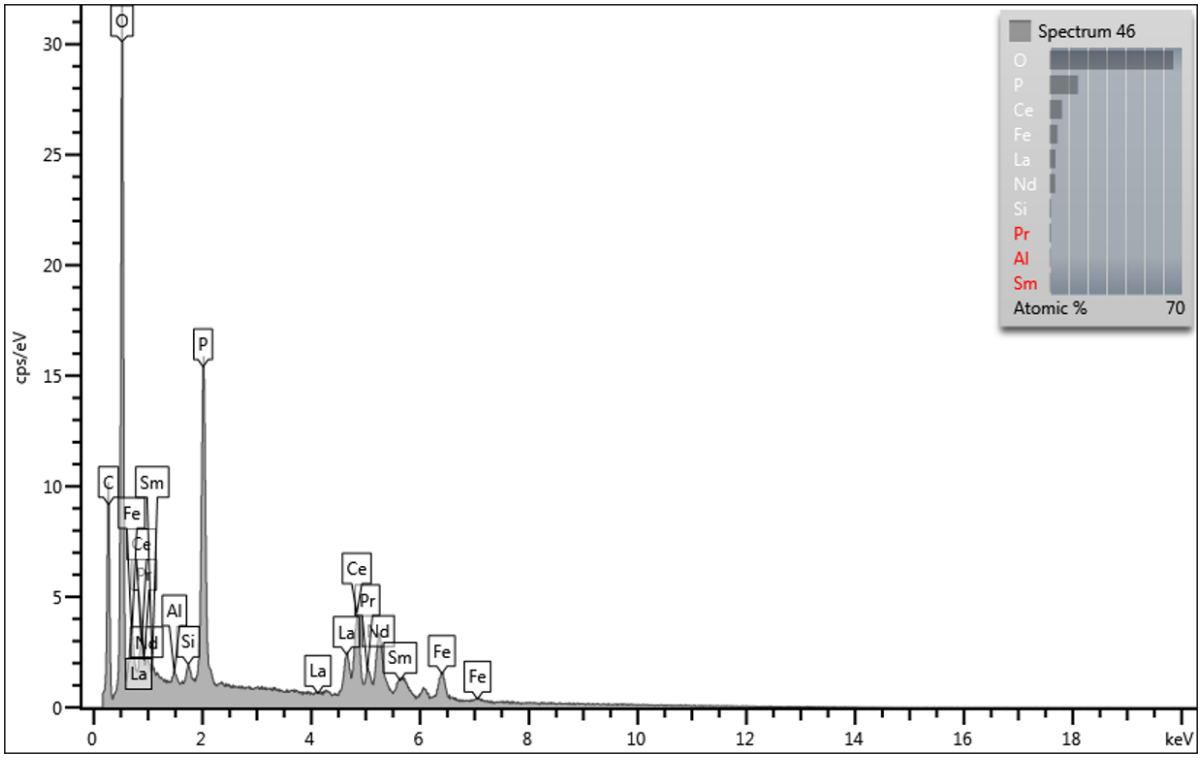

Figure A2.25: Spectrum 46; monazite ((Ce,La,Nd)PO_4) with Fe, Al and Si impurities.

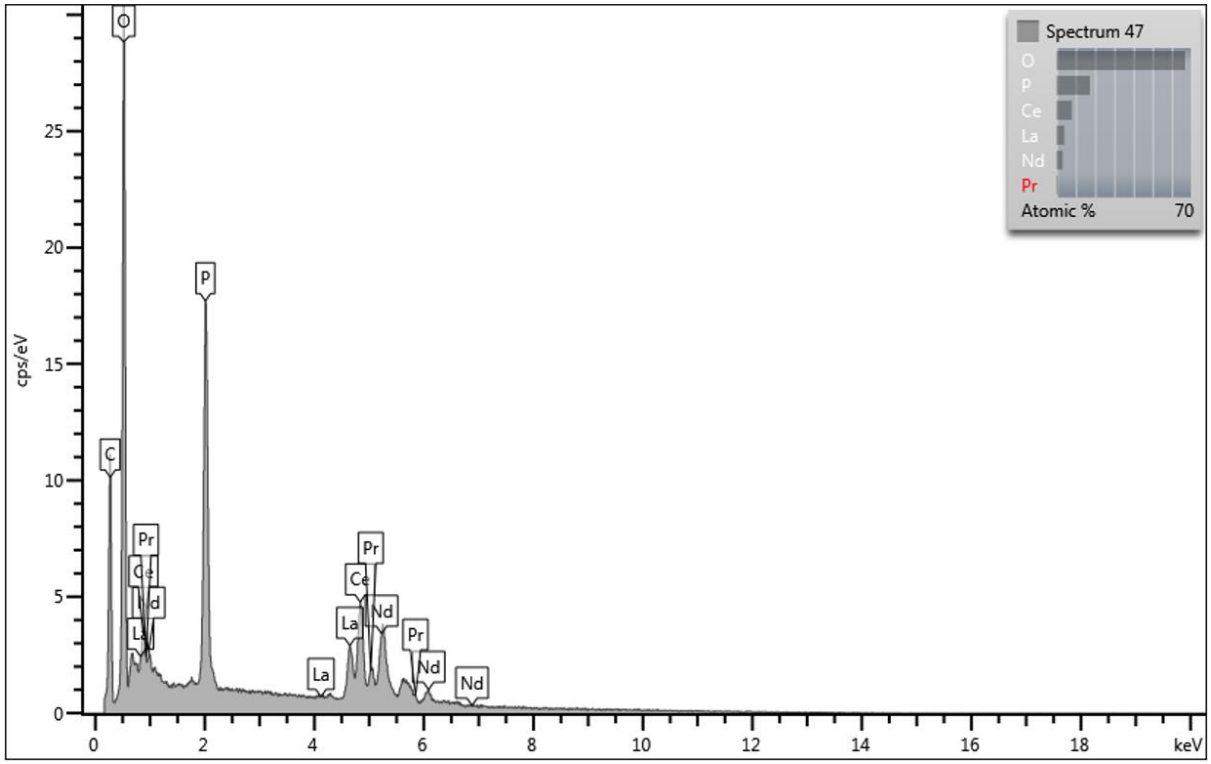

Figure A2.26: Spectrum 47; monazite ($(Ce,La,Nd)PO_4$).

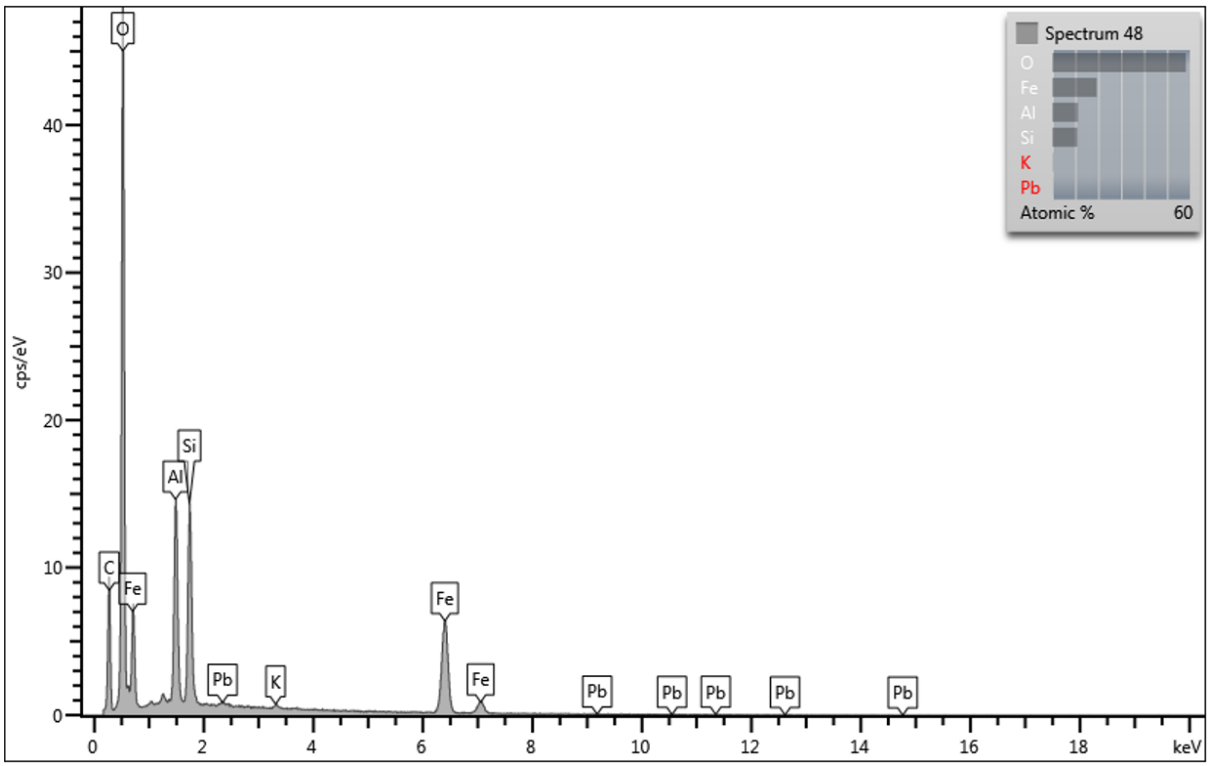

Figure A2.27: Spectrum 48; chlorite ($Fe_5Al_2Si_3O_{10}(OH)_8$) with K and Pb impurities.

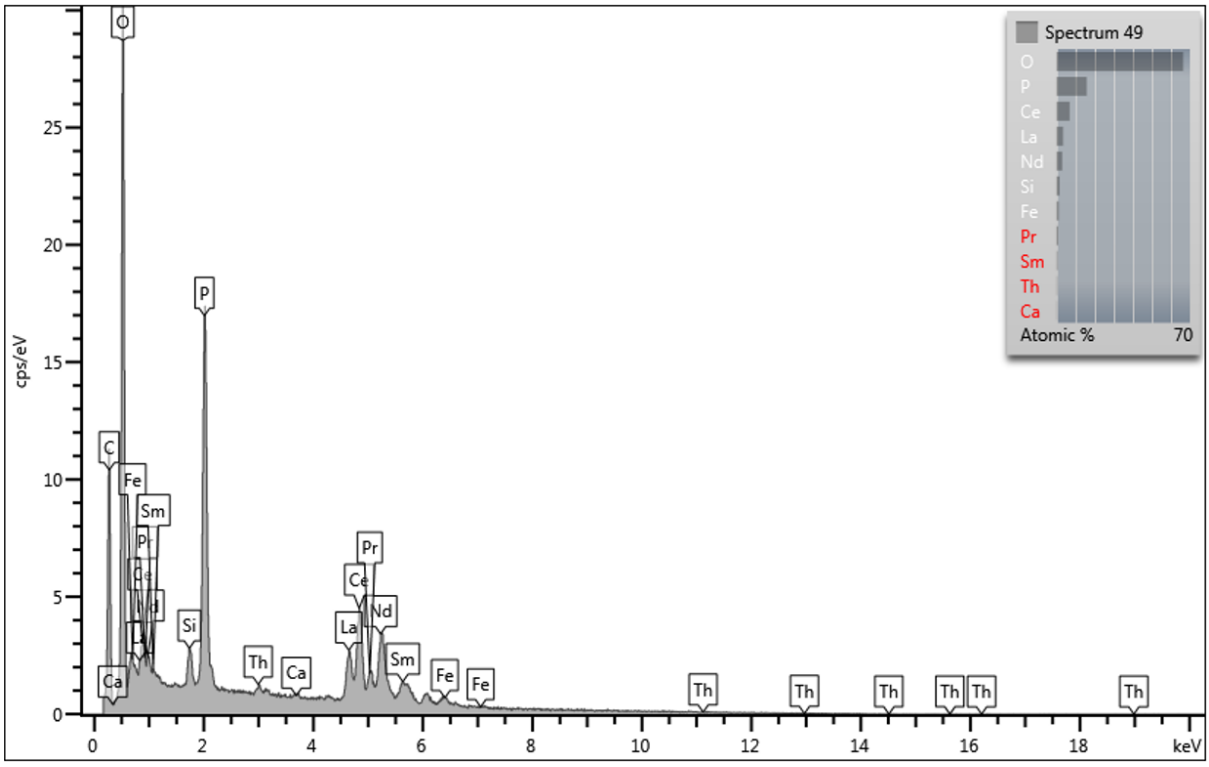

Figure A2.28: Spectrum 49; monazite ($(Ce,La,Nd)PO_4$) with Si, Fe, Th and Ca impurities.

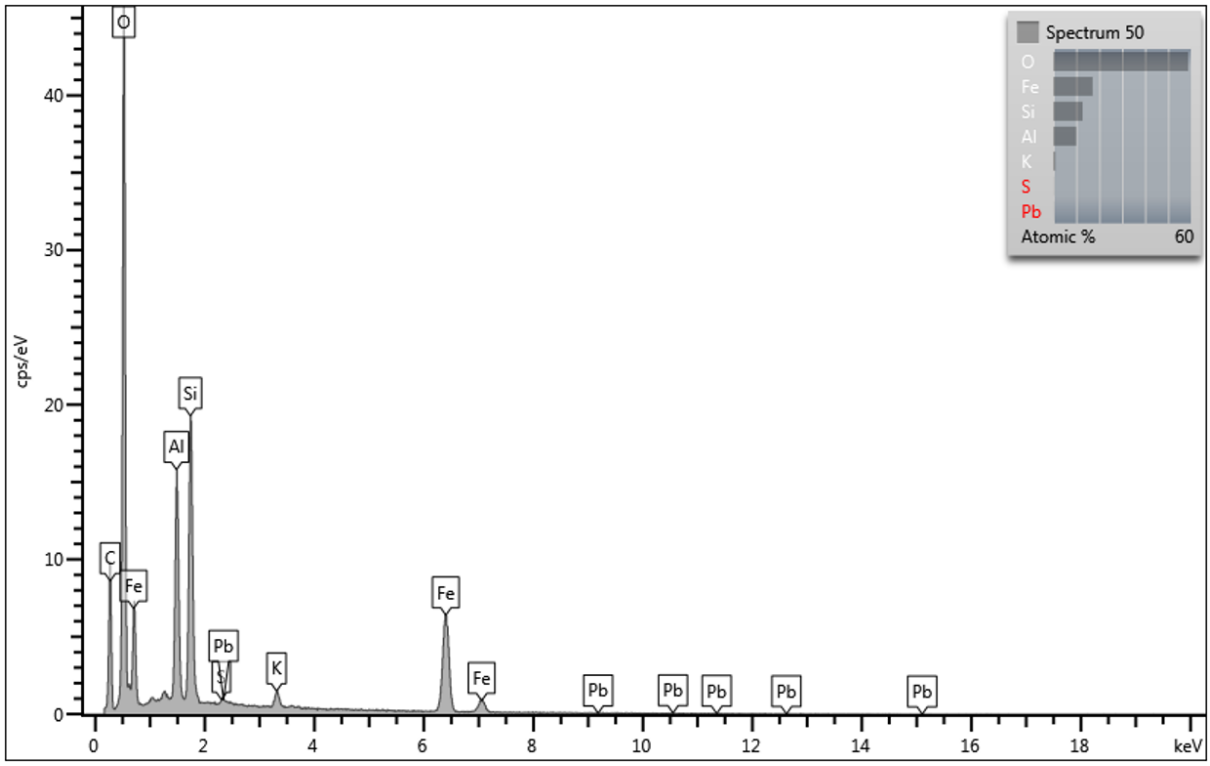

Figure A2.29: Spectrum 50; chlorite ($Fe_5Al_2Si_3O_{10}(OH)_8$) with minor K, S and Pb impurities.

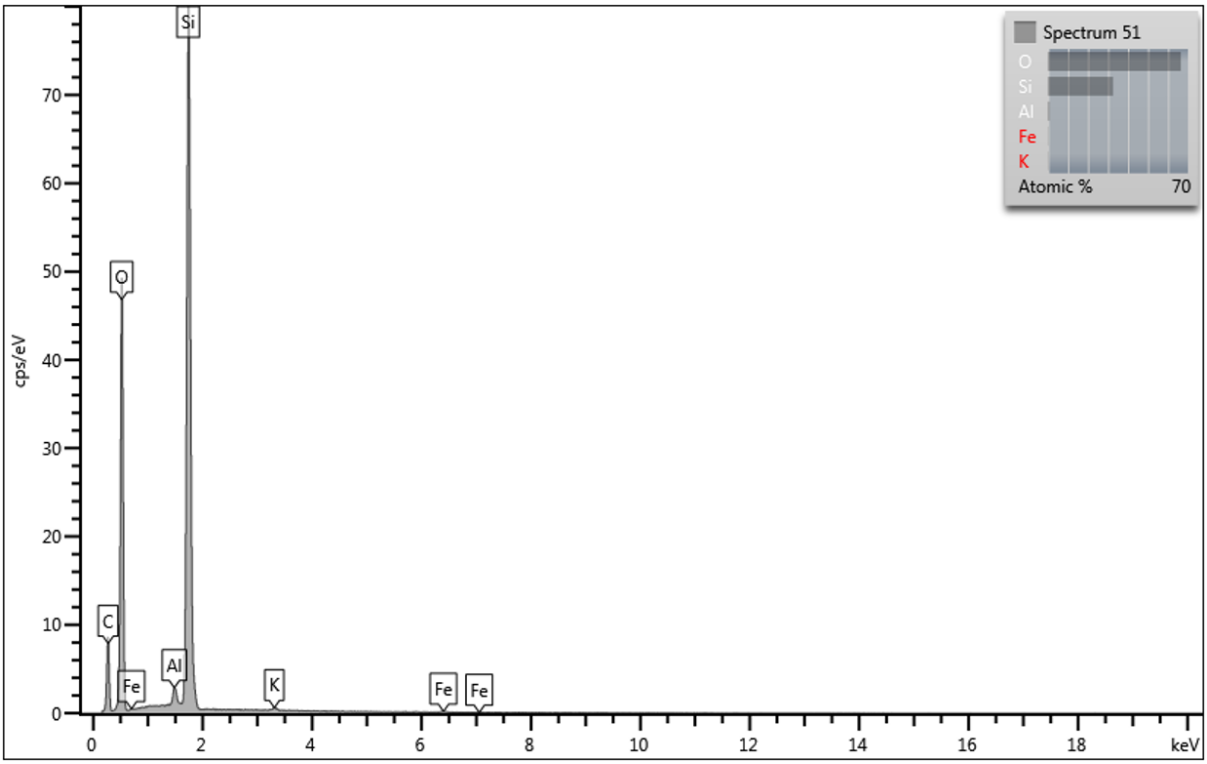

Figure A2.30: Spectrum 51; quartz (SiO_2) with Al, Fe and K impurities.

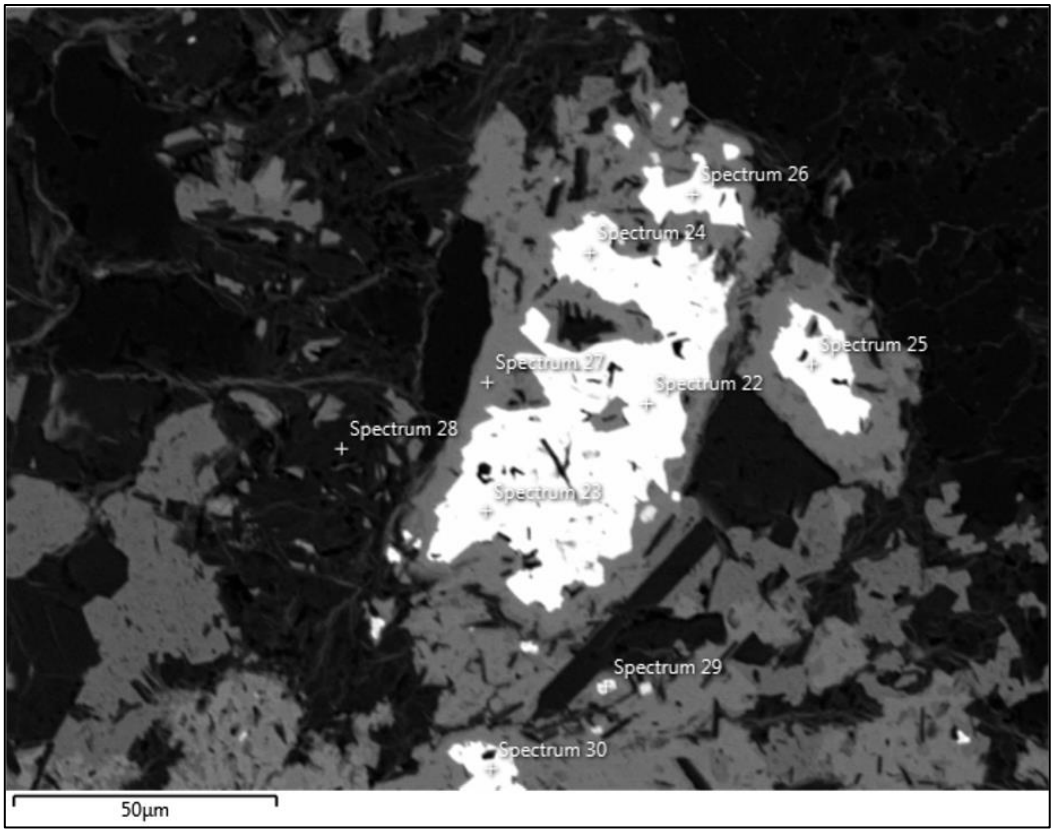

Figure A2.31: A fourth BSE image acquired from Sample 36, Figure 5.4, showing the location of SEM-EDX spectrums 22 – 30. The detailed spot analysis of each spectrum is indicated below on Figures A2.32 – A2.40, respectively.

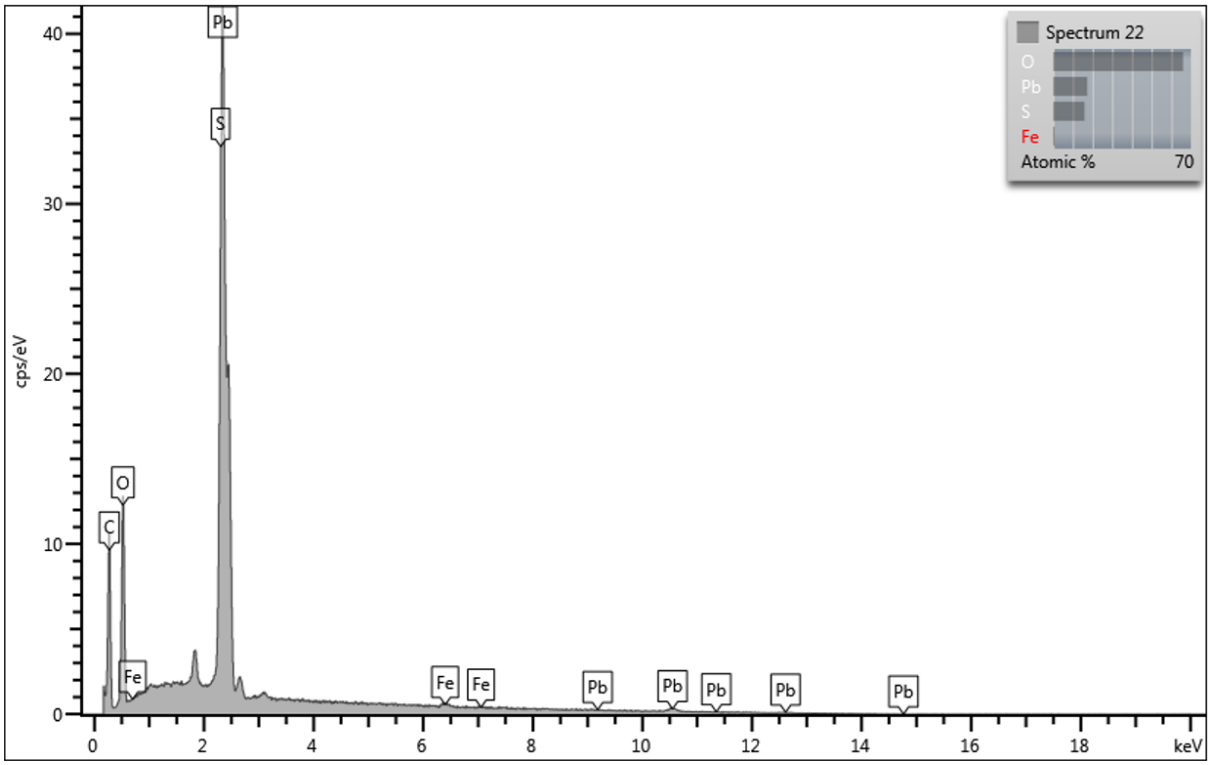

Figure A2.32: Spectrum 22; anglesite ($PbSO_4$) with Fe impurities.

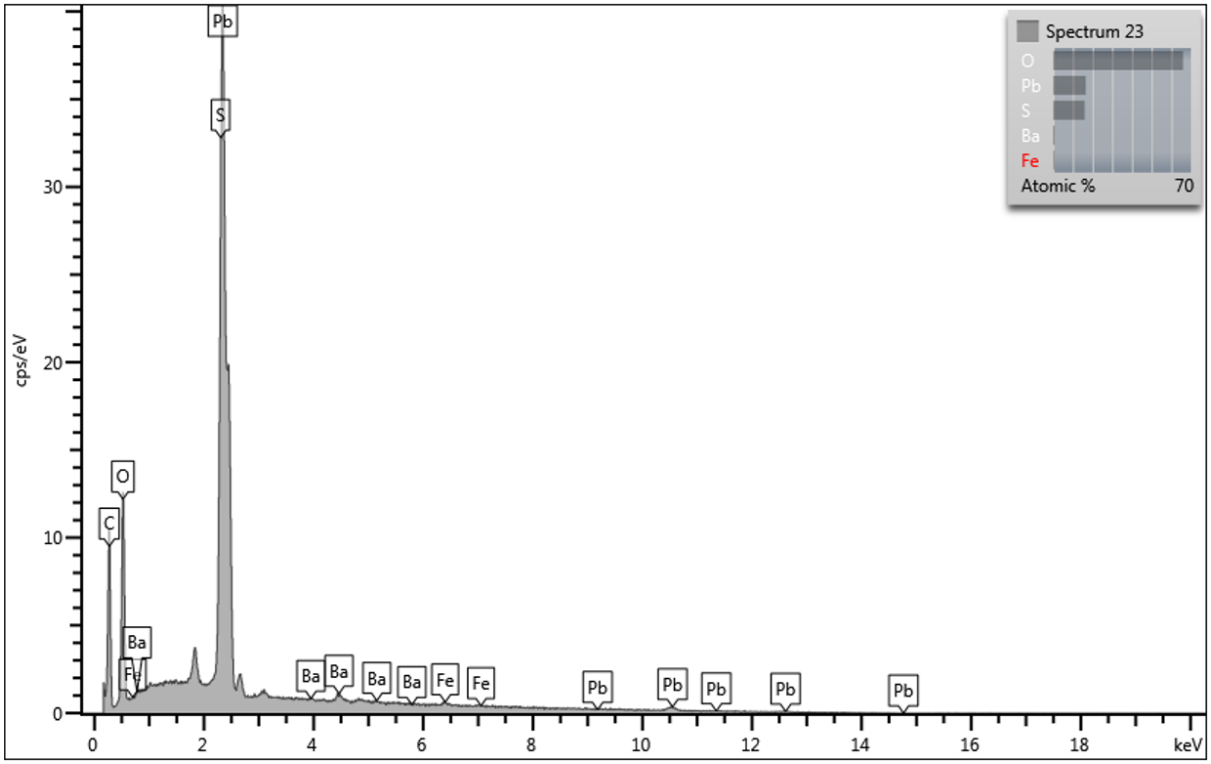

Figure A2.33: Spectrum 23; anglesite ($PbSO_4$) with Ba and Fe impurities.

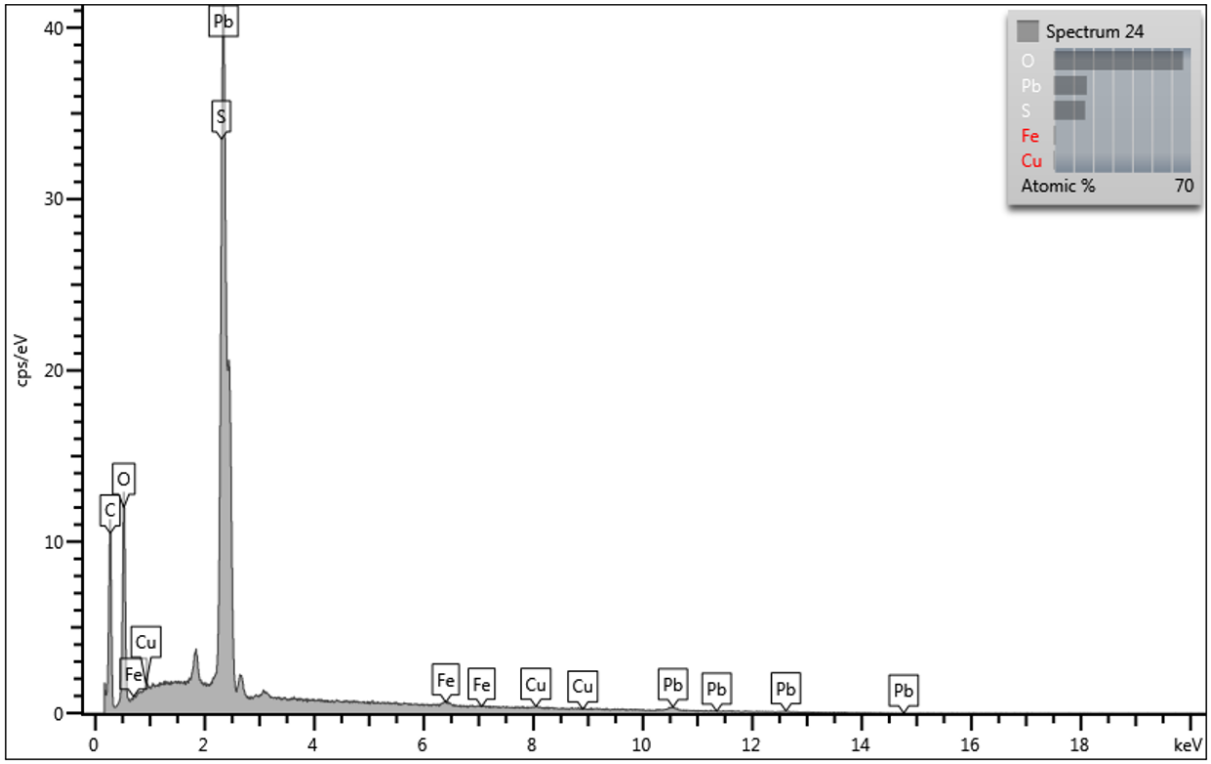

Figure A2.34: Spectrum 24; anglesite ($PbSO_4$) with Fe and Cu impurities.

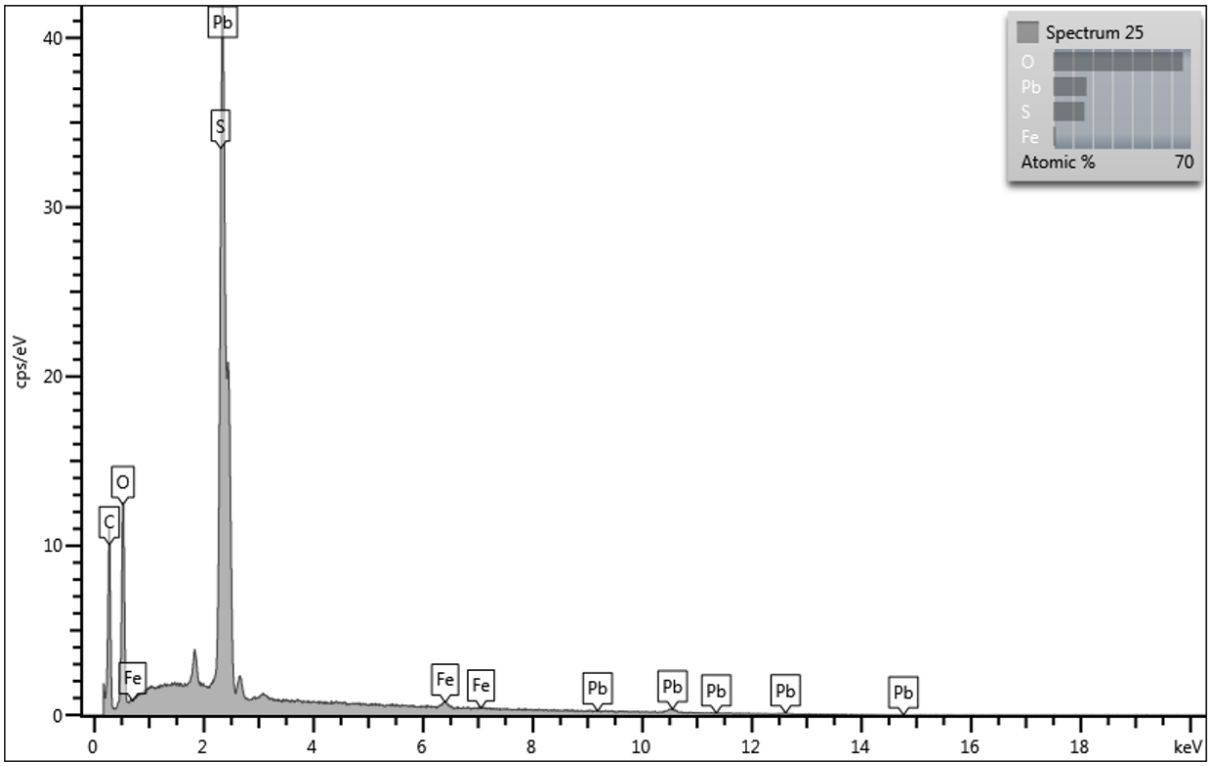

Figure A2.35: Spectrum 25; anglesite ($PbSO_4$) with Fe impurities.

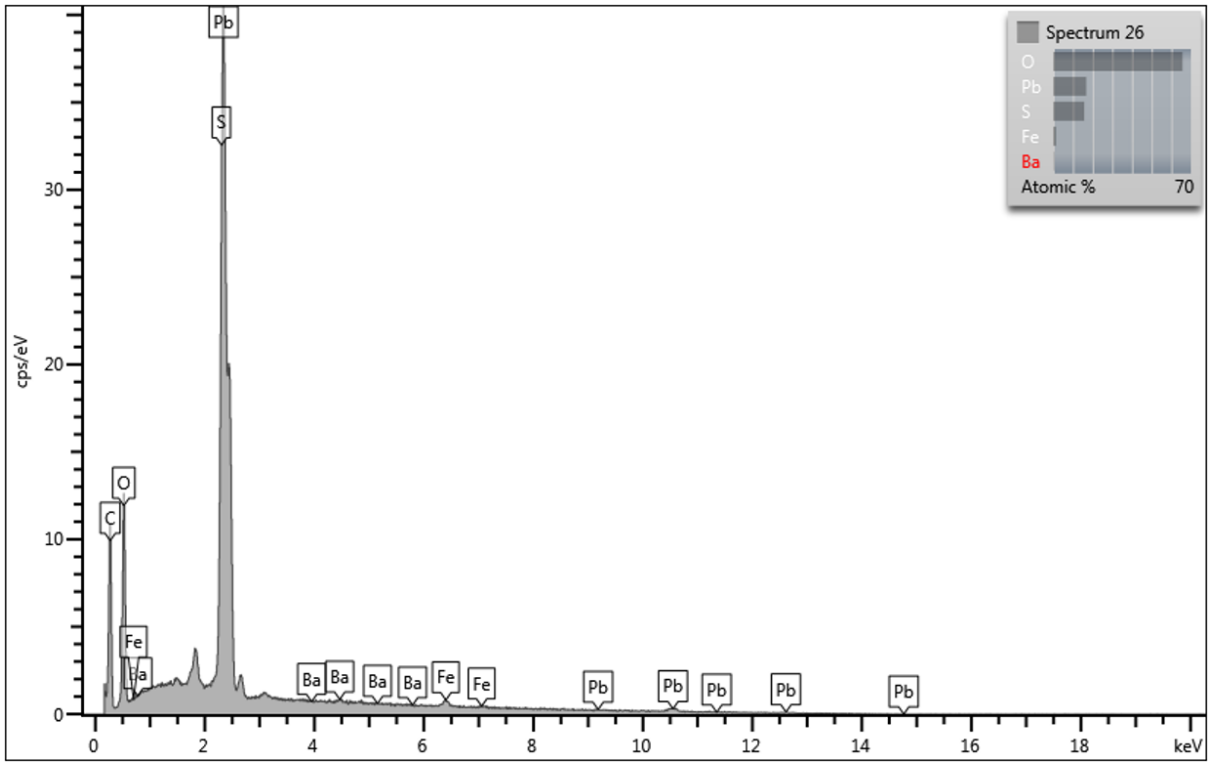

Figure A2.36: Spectrum 26; anglesite ($PbSO_4$) with Fe and Ba impurities.

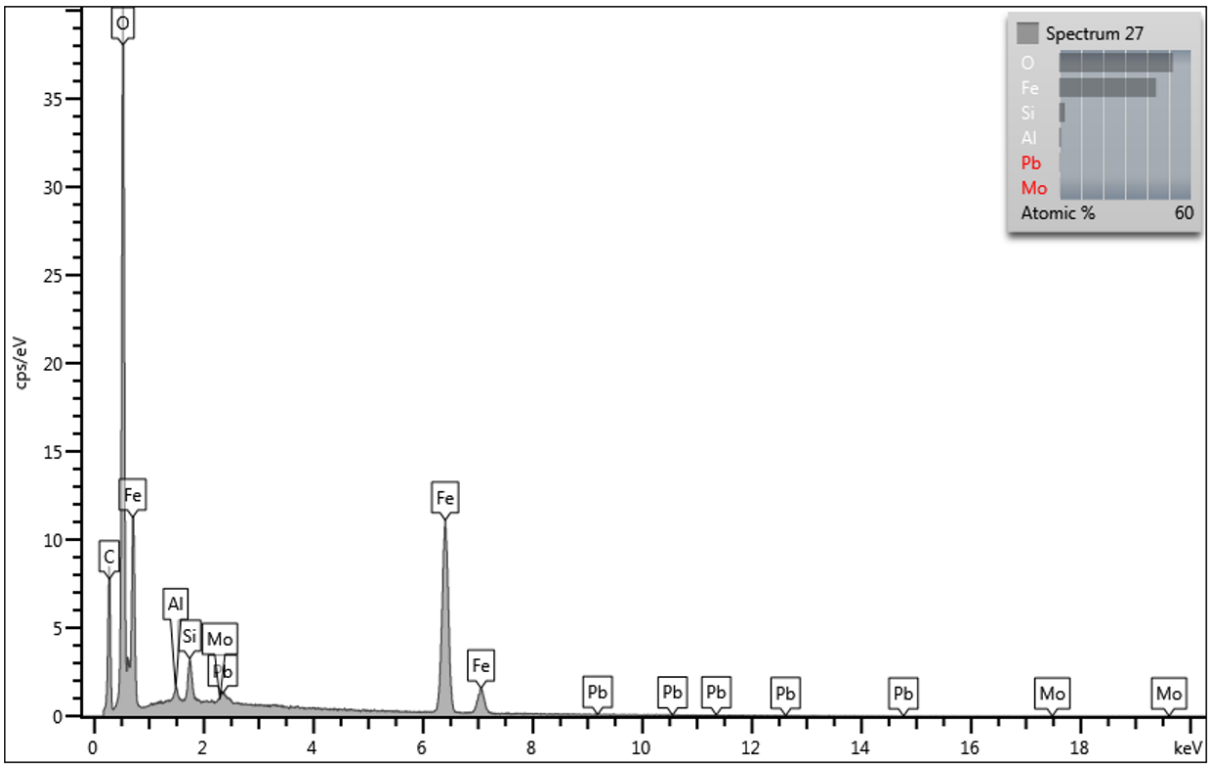

Figure A2.37: Spectrum 27; hematite (Fe_2O_3) with Si, Al, Pb and Mo impurities.

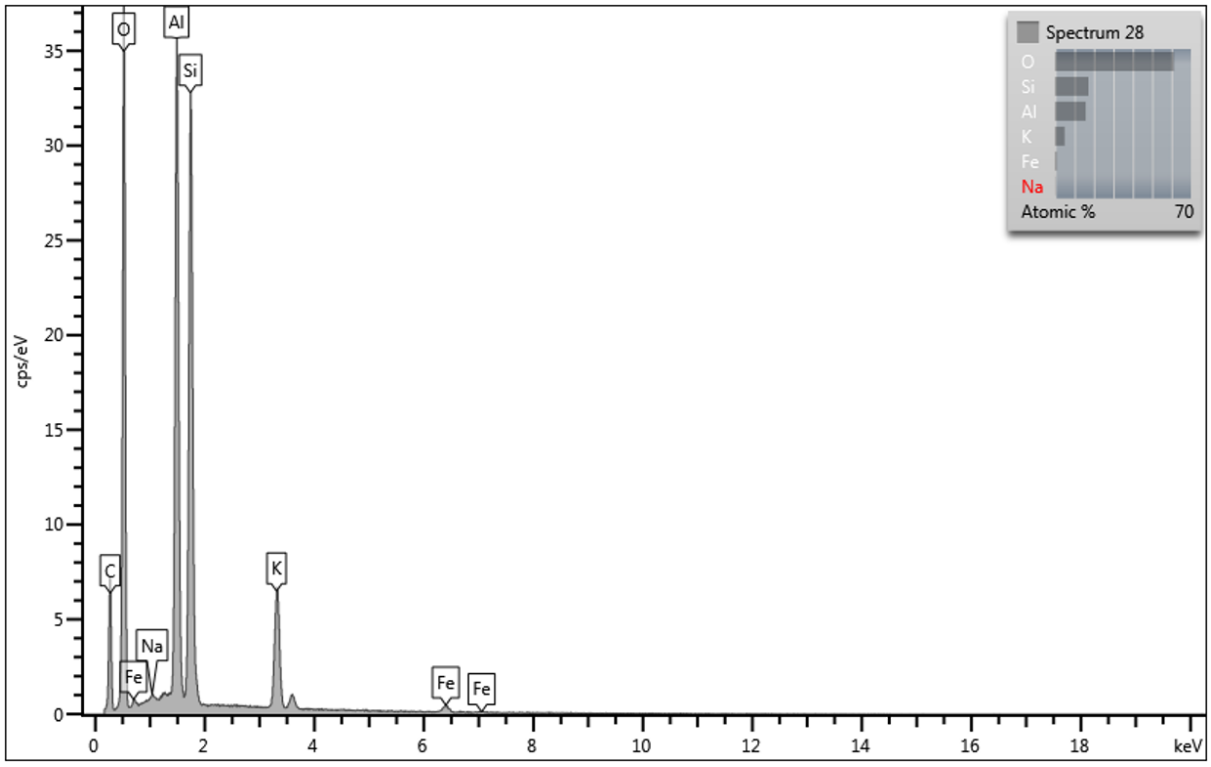

Figure A2.38: Spectrum 28; K-feldspar ($KAlSi_3O_8$) with minor Fe as well as Na.

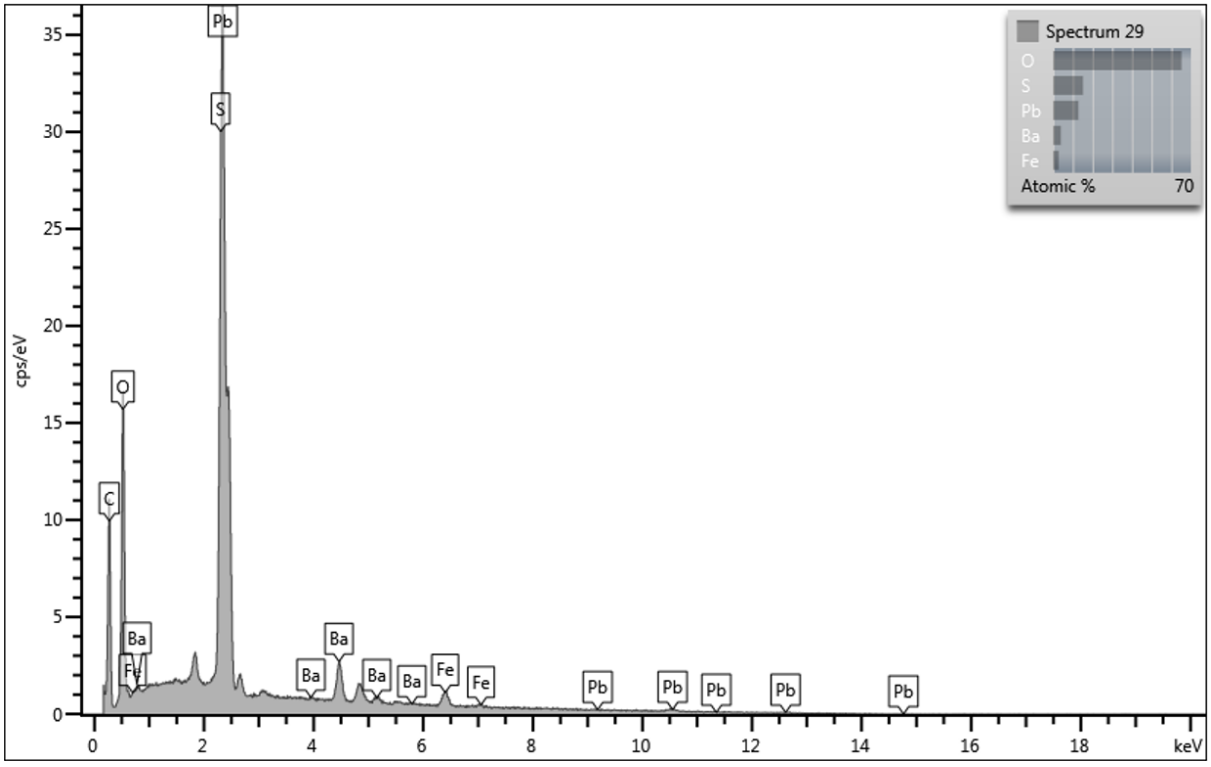

Figure A2.39: Spectrum 29; anglesite ($PbSO_4$) with Fe and Ba impurities.

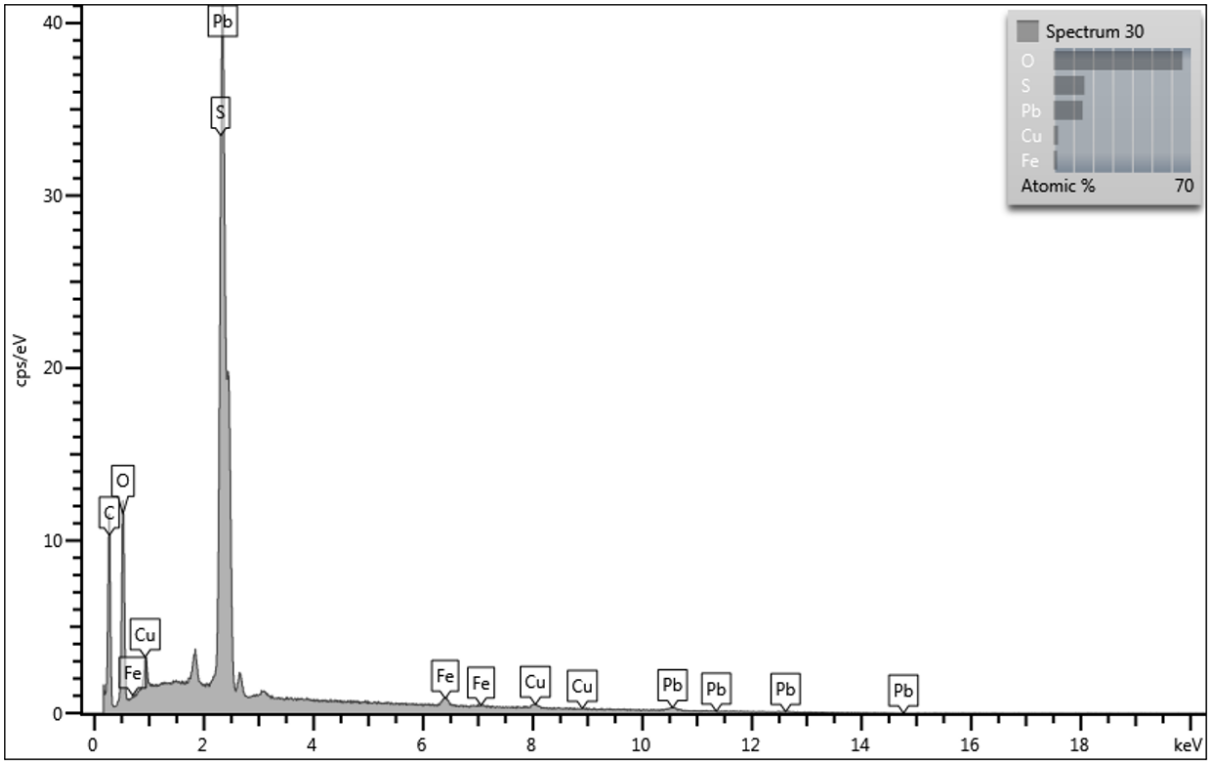

Figure A2.40: Spectrum 30; anglesite ($PbSO_4$) with Cu and Fe impurities.

Appendix 3: Whole rock geochemistry

Major elements were analysed using XRF, whereas trace elements were analysed with ICP-MS (also referred to as 4A/MS) and ICP-OES (referred to as 4A/OE). Fe_2O_3 (t) is the total Fe content in the rock. X = below the detection limit.

Table A3.1: Geochemical results of 8 rhyolites.

Elements	Method	Units	Detection limit	Rhyolites							
				Sample 07	Sample 12	Sample 13	Sample 23	Sample 25	Sample 26	Sample 31	Sample 44
SiO_2	*XRF*	*wt.%*		79.94	87.39	75.78	82.24	75.97	72.25	76.98	78.26
TiO_2	*XRF*	*wt.%*		0.26	0.17	0.33	0.25	0.35	0.36	0.32	0.36
Al_2O_3	*XRF*	*wt.%*		11.00	6.11	11.01	8.65	11.38	11.93	10.1	11.58
Fe_2O_3 (t)	*XRF*	*wt.%*		3.40	2.66	5.72	4.55	6.31	6.70	6.18	4.18
MnO	*XRF*	*wt.%*		0.016	0.013	0.031	0.290	0.025	0.096	0.882	0.014
MgO	*XRF*	*wt.%*		0.03	0.01	0.05	0.01	0.10	0.19	0.04	0.04
CaO	*XRF*	*wt.%*		0.03	0.02	0.02	0.01	0.03	0.05	0.08	0.04
Na_2O	*XRF*	*wt.%*		0.17	0.13	0.08	0.04	0.10	0.10	0.03	0.15
K_2O	*XRF*	*wt.%*		3.15	2.09	5.08	2.50	3.70	6.88	3.02	3.40
P_2O_5	*XRF*	*wt.%*		0.056	0.046	0.056	0.065	0.093	0.073	0.084	0.107
Cr_2O_3	*XRF*	*wt.%*		0.006	0.003	0.002	0.006	0.004	0.005	0.006	0.007
Total				99.58	99.76	99.82	99.89	99.77	99.76	99.852	99.75
LOI				1.52	1.13	1.66	1.30	1.71	1.13	2.13	1.61
H_2O^-				0.36	0.38	0.35	0.23	0.31	0.22	0.4	0.29
Ag	*4A/MS*	*ppm*	*0.05*	0.13	0.8	0.17	0.17	0.68	0.08	0.08	0.35
As	*4A/MS*	*ppm*	*0.5*	8.2	13.3	3.4	6.6	3.1	10.9	1.8	9.8
Ba	*4A/MS*	*ppm*	*0.1*	395.4	472.2	1258.7	299.1	522.4	1644.5	188.5	561.9
Be	*4A/MS*	*ppm*	*0.05*	2.29	1.24	2.05	1.56	3.2	1.96	3.12	2.57
Bi	*4A/MS*	*ppm*	*0.01*	0.07	0.85	0.07	0.1	0.07	0.26	0.11	0.43
Ce	*4A/MS*	*ppm*	*0.01*	161.42	87.91	153.39	101.5	146.9	151.2	133.19	130.84
Co	*4A/MS*	*ppm*	*0.1*	1.3	0.5	1.5	1.7	5.7	3.1	1.9	1.7
Cr	*4A/OE*	*ppm*	*1*	4	4	4	4	4	4	8	4
Cs	*4A/MS*	*ppm*	*0.05*	4.82	1.39	2.52	3.46	8.68	1.79	5.6	3.08
Cu	*4A/OE*	*ppm*	*0.5*	3.4	23.5	4	2.7	70.5	33.1	7	9.3
Dy	*4A/MS*	*ppm*	*0.01*	8.46	7.01	10.64	8.58	10.11	12.34	10.36	11.52
Er	*4A/MS*	*ppm*	*0.01*	5.62	4.48	6.8	5.41	6.41	7.34	6.52	7.43
Eu	*4A/MS*	*ppm*	*0.01*	1.92	1.32	2.28	1.91	2.09	2.5	2.09	2.14
Ga	*4A/MS*	*ppm*	*0.05*	17.97	7.77	20.59	15.03	19.65	21.5	18.06	22.87
Gd	*4A/MS*	*ppm*	*0.01*	9.24	6.59	10.91	9.23	9.96	11.6	9.7	10.57
Ge	*4A/MS*	*ppm*	*0.05*	1.3	1.64	1.21	0.71	1.1	0.78	1	0.84
Hf	*4A/MS*	*ppm*	*0.05*	10.6	6.62	10.46	8.55	10.59	12.16	10.02	12.27
Ho	*4A/MS*	*ppm*	*0.01*	1.72	1.46	2.18	1.74	2.11	2.48	2.11	2.39
In	*4A/MS*	*ppm*	*0.01*	0.05	0.14	0.09	0.3	0.13	0.1	0.13	0.17
La	*4A/MS*	*ppm*	*0.01*	84.95	45.1	80.96	53.35	80.63	80.96	70.24	73.58

Li	*4A/MS*	*ppm*	*0.1*	2.1	8.9	10.3	3	1.6	22.4	3.1	1.4
Lu	*4A/MS*	*ppm*	*0.01*	0.78	0.55	0.91	0.8	0.95	1.07	0.91	1.07
Mo	*4A/MS*	*ppm*	*0.1*	0.3	2.2	2.3	0.3	0.7	1.7	2	0.3
Nb	*4A/MS*	*ppm*	*0.05*	18.17	11.96	19.8	13.62	13.55	20.41	12.74	16.7
Nd	*4A/MS*	*ppm*	*0.01*	64.33	35.67	62.28	50.15	64.02	65.39	57.02	54.47
Ni	*4A/OE*	*ppm*	*0.5*	2	1.5	1	1.1	5.6	1.2	1.9	1.2
Pb	*4A/MS*	*ppm*	*0.5*	35.6	420.1	64.2	37	360.6	30.2	9.7	575.8
Pr	*4A/MS*	*ppm*	*0.01*	17.49	9.72	16.99	12.77	17.14	17.05	14.96	14.16
Rb	*4A/MS*	*ppm*	*0.05*	236.05	145.56	301.15	182.09	312.16	368.79	222.6	272.57
Sb	*4A/MS*	*ppm*	*0.05*	13.42	3.27	2.87	12.94	6.82	1.55	3.17	18.61
Sc	*4A/MS*	*ppm*	*0.1*	3.5	2.4	6.4	5.4	8.4	8.4	6.5	6.9
Se	*4A/MS*	*ppm*	*0.5*	1.2	1	1.4	1.1	1.1	1.4	1.2	1.2
Sm	*4A/MS*	*ppm*	*0.01*	12.48	7.35	12.58	9.89	11.48	12.45	10.54	11.28
Sn	*4A/MS*	*ppm*	*0.1*	3.6	1.7	3.7	2.9	3.5	3.9	3.7	4.3
Sr	*4A/MS*	*ppm*	*0.05*	6.63	7.71	12.63	12.11	7.23	62.88	6.58	30.53
Ta	*4A/MS*	*ppm*	*0.01*	1.29	0.79	1.29	1	1.01	1.46	0.94	1.26
Tb	*4A/MS*	*ppm*	*0.01*	1.45	1.11	1.76	1.43	1.57	1.92	1.64	1.74
Th	*4A/MS*	*ppm*	*0.01*	22.9	14.96	21.73	15.17	19.47	21.76	18.31	21.86
Tl	*4A/MS*	*ppm*	*0.02*	2.47	1.49	3.59	2.69	3.73	5.08	2.07	3.14
Tm	*4A/MS*	*ppm*	*0.01*	0.83	0.62	1	0.77	0.96	1.09	0.94	1.08
U	*4A/MS*	*ppm*	*0.01*	4.41	10.11	5.31	4.45	5.64	5.57	4.72	5.09
V	*4A/OE*	*ppm*	*1*	8	18	2	3	30	2	2	4
W	*4A/MS*	*ppm*	*0.1*	22.2	2.2	3.2	17.5	9.7	7.4	1.4	3.3
Y	*4A/MS*	*ppm*	*0.05*	43.01	38.73	58.44	43.48	50.47	63.86	55.76	59.97
Yb	*4A/MS*	*ppm*	*0.01*	5.24	3.9	6.22	5.13	6.41	7.33	6.36	7.19
Zn	*4A/OE*	*ppm*	*1*	65	121	304	175	129	233	100	125
Zr	*4A/MS*	*ppm*	*0.1*	420.5	261.4	411.4	330.5	404.6	464.8	390.2	461.2

Table A3.2: A total of 10 tuff samples were collected and analysed. Geochemical results of 5 tuff samples. The geochemical results of the other 5 samples are reported in Table A3.3 below.

Elements	Method	Unit	Detection limit	Tuff				
				Sample 05	Sample 11	Sample 14	Sample 18	Sample 27
SiO_2	*XRF*	*wt.%*		72.05	79.23	72.40	86.96	55.97
TiO_2	*XRF*	*wt.%*		0.35	0.41	0.44	0.23	0.23
Al_2O_3	*XRF*	*wt.%*		14.75	12.51	13.25	6.83	7.96
Fe_2O_3 (t)	*XRF*	*wt.%*		6.13	1.74	7.51	2.43	17.72
MnO	*XRF*	*wt.%*		0.006	0.103	0.009	0.004	10.10
MgO	*XRF*	*wt.%*		0.08	0.07	0.21	0.05	0.02
CaO	*XRF*	*wt.%*		0.04	0.03	0.01	0.02	0.02
Na_2O	*XRF*	*wt.%*		0.14	0.10	0.15	0.07	0.05
K_2O	*XRF*	*wt.%*		4.30	3.50	3.94	2.13	2.35
P_2O_5	*XRF*	*wt.%*		0.043	0.103	0.106	0.094	0.239
Cr_2O_3	*XRF*	*wt.%*		0.008	0.006	0.009	0.006	0.005
Total	*XRF*	*wt.%*		99.80	99.71	99.96	99.84	99.78
LOI				1.90	1.91	1.93	1.02	5.12
H_2O^-				0.25	0.38	0.21	0.23	0.43
Ag	*4A/MS*	*ppm*	*0.05*	0.07	0.16	0.19	0.6	0.91
As	*4A/MS*	*ppm*	*0.5*	11.6	3.5	8.3	29.6	4.3
Ba	*4A/MS*	*ppm*	*0.1*	552.9	247.6	489.8	607.5	669.3
Be	*4A/MS*	*ppm*	*0.05*	1.85	2.49	3.86	1.4	2.61
Bi	*4A/MS*	*ppm*	*0.01*	0.38	0.11	1.41	0.71	0.18
Ce	*4A/MS*	*ppm*	*0.01*	135.67	187.12	168.42	134.79	79.46
Co	*4A/MS*	*ppm*	*0.1*	1.8	3	1	0.3	46.5
Cr	*4A/OE*	*ppm*	*1*	11	9	37	12	13
Cs	*4A/MS*	*ppm*	*0.05*	4.33	3.59	5.06	2.33	2.24
Cu	*4A/OE*	*ppm*	*0.5*	1	17.4	2.4	4.4	129.8
Dy	*4A/MS*	*ppm*	*0.01*	11.78	11.55	10.8	9.07	6.82
Er	*4A/MS*	*ppm*	*0.01*	8.65	7.25	6.83	4.43	4.49
Eu	*4A/MS*	*ppm*	*0.01*	1.61	3.04	1.84	2.87	0.92
Ga	*4A/MS*	*ppm*	*0.05*	24.94	23.32	21.82	12.93	14.92
Gd	*4A/MS*	*ppm*	*0.01*	8.81	12.98	9.47	11.99	4.9
Ge	*4A/MS*	*ppm*	*0.05*	1.71	1.38	1.5	1.24	0.47
Hf	*4A/MS*	*ppm*	*0.05*	13.58	11.13	10.98	6.17	7.54
Ho	*4A/MS*	*ppm*	*0.01*	2.7	2.37	2.21	1.61	1.44
In	*4A/MS*	*ppm*	*0.01*	0.04	0.1	0.75	0.18	0.15
La	*4A/MS*	*ppm*	*0.01*	75.88	100.73	90.9	66.46	25.12
Li	*4A/MS*	*ppm*	*0.1*	1.8	2.5	5.6	1.1	2
Lu	*4A/MS*	*ppm*	*0.01*	1.2	0.97	0.92	0.54	0.63
Mo	*4A/MS*	*ppm*	*0.1*	0.4	1.4	0.6	2.7	1.6
Nb	*4A/MS*	*ppm*	0.05	21.48	21.11	25.03	9.63	10.73
Nd	*4A/MS*	*ppm*	0.01	45.8	85.21	63.17	79.3	21.42
Ni	*4A/OE*	*ppm*	*0.5*	16.9	4.8	4.2	0.6	5.6
Pb	*4A/MS*	*ppm*	*0.5*	12.1	532.4	770.3	54.7	443.6
Pr	*4A/MS*	*ppm*	*0.01*	13.91	22.29	18.3	17.91	5.68
Rb	*4A/MS*	*ppm*	*0.05*	294.19	244.45	300.69	142.95	150.37
Sb	*4A/MS*	*ppm*	*0.05*	17.93	6.33	9.12	22.77	3.4

Sc	*4A/MS*	*ppm*	*0.1*	6.5	8.8	10.2	5.3	4.8
Se	*4A/MS*	*ppm*	*0.5*	0.8	1.5	1.1	1.4	0.8
Sm	*4A/MS*	*ppm*	*0.01*	8.8	16.89	11.64	16.94	4.28
Sn	*4A/MS*	*ppm*	*0.1*	5	4.1	6.4	3.5	2.5
Sr	*4A/MS*	*ppm*	*0.05*	14.66	14.52	23.34	31.33	13.02
Ta	*4A/MS*	*ppm*	*0.01*	1.46	1.42	1.11	0.62	0.7
Tb	*4A/MS*	*ppm*	*0.01*	1.68	2	1.68	1.73	0.97
Th	*4A/MS*	*ppm*	*0.01*	29.71	23.6	32.61	11.09	13.82
Tl	*4A/MS*	*ppm*	*0.02*	2.52	3.05	2.79	1.38	2.12
Tm	*4A/MS*	*ppm*	*0.01*	1.28	1.07	0.99	0.6	0.61
U	*4A/MS*	*ppm*	*0.01*	7.34	8.39	6.67	4.83	3.68
V	*4A/OE*	*ppm*	*1*	2	6	31	15	X
W	*4A/MS*	*ppm*	*0.1*	3.5	2.8	23.5	3.7	1.6
Y	*4A/MS*	*ppm*	*0.05*	67.28	58.15	55.98	37.13	37.44
Yb	*4A/MS*	*ppm*	*0.01*	8.27	6.72	6.25	3.63	4.31
Zn	*4A/OE*	*ppm*	*1*	12	79	30	14	475
Zr	*4A/MS*	*ppm*	*0.1*	530.5	441.2	431.5	235.9	294.4

Table A3.3: The geochemical results of the other 5 tuff samples.

Element	Method	Unit	Detection limit	Tuff				
				Sample 29	Sample 32	Sample 35	Sample 36	Sample 43
SiO_2	*XRF*	*wt.%*		64.02	81.32	70.5	72.79	79.03
TiO_2	*XRF*	*wt.%*		0.23	0.33	0.31	0.32	0.30
Al_2O_3	*XRF*	*wt.%*		6.57	11.01	10.18	10.73	10.34
Fe_2O_3 (t)	*XRF*	*wt.%*		11.69	2.03	13.98	10.76	4.20
MnO	*XRF*	*wt.%*		11.35	0.009	0.029	0.032	1.07
MgO	*XRF*	*wt.%*		0.005	0.02	0.005	0.005	0.02
CaO	*XRF*	*wt.%*		0.03	0.03	0.02	0.02	0.01
Na_2O	*XRF*	*wt.%*		0.04	0.11	0.12	0.05	0.14
K_2O	*XRF*	*wt.%*		2.21	3.18	2.82	2.13	2.97
P_2O_5	*XRF*	*wt.%*		0.154	0.054	0.196	0.118	0.049
Cr_2O_3	*XRF*	*wt.%*		0.002	0.003	0.006	0.004	0.006
Total				99.816	99.786	99.801	99.734	99.76
LOI				3.52	1.69	1.64	2.78	1.62
H_2O^-				0.32	0.36	0.5	0.57	0.3
Ag	*4A/MS*	*ppm*	0.05	0.44	0.14	0.28	0.66	0.51
As	*4A/MS*	*ppm*	0.5	20.3	2.9	12.5	7.3	10.3
Ba	*4A/MS*	*ppm*	0.1	513.5	305.1	454.9	154.4	568.9
Be	*4A/MS*	*ppm*	0.05	2.72	2.04	2.89	2.3	2.64
Bi	*4A/MS*	*ppm*	0.01	0.86	0.85	0.06	0.08	0.32
Ce	*4A/MS*	*ppm*	0.01	97.36	135.18	128.45	169.38	122.81
Co	*4A/MS*	*ppm*	0.1	19	0.7	2	2.1	11.1
Cr	*4A/OE*	*ppm*	1	15	3	12	4	9
Cs	*4A/MS*	*ppm*	0.05	2.14	2.69	7.36	3.12	2.26
Cu	*4A/OE*	*ppm*	0.5	38.2	2.9	16.1	12.4	20.4
Dy	*4A/MS*	*ppm*	0.01	8.71	10.7	10.23	11.85	9.6
Er	*4A/MS*	*ppm*	0.01	4.94	6.72	6.49	7.3	6.04
Eu	*4A/MS*	*ppm*	0.01	1.98	2.07	1.92	2.66	1.73
Ga	*4A/MS*	*ppm*	0.05	14.27	20.1	18.1	19.74	19.23
Gd	*4A/MS*	*ppm*	0.01	9.72	10.13	9.11	12.18	8.76
Ge	*4A/MS*	*ppm*	0.05	0.49	1.59	0.75	1.16	0.89
Hf	*4A/MS*	*ppm*	0.05	7.61	11.1	10.57	10.94	9.63
Ho	*4A/MS*	*ppm*	0.01	1.76	2.17	2.13	2.4	1.95
In	*4A/MS*	*ppm*	0.01	0.43	0.09	0.09	0.1	0.15
La	*4A/MS*	*ppm*	0.01	51.19	72.64	66.58	89.55	65.13
Li	*4A/MS*	*ppm*	0.1	1.6	2.4	1.3	10.4	2.5
Lu	*4A/MS*	*ppm*	0.01	0.71	0.98	0.94	1	0.85
Mo	*4A/MS*	*ppm*	0.1	1.1	3.2	0.8	1.6	3.1
Nb	*4A/MS*	*ppm*	0.05	11.89	18.54	17.07	13.03	14.43
Nd	*4A/MS*	*ppm*	0.01	42.09	57.46	53.5	74.57	50.77
Ni	*4A/OE*	*ppm*	0.5	X	1.2	3.4	2.1	2.5
Pb	*4A/MS*	*ppm*	0.5	290	37.8	425.4	1665.8	306.1
Pr	*4A/MS*	*ppm*	0.01	11.02	15.41	14.15	19.44	13.62

Rb	*4A/MS*	*ppm*	0.05	141.06	225.39	222.64	154.73	226.08
Sb	*4A/MS*	*ppm*	0.05	11.31	2.16	27.12	7.33	7.78
Sc	*4A/MS*	*ppm*	0.1	6.1	6.7	6.3	6	6.9
Se	*4A/MS*	*ppm*	0.5	1	1.2	1.1	1.4	1
Sm	*4A/MS*	*ppm*	0.01	9.62	10.9	10.52	14.15	8.77
Sn	*4A/MS*	*ppm*	0.1	2.2	4.2	3.2	3.1	3.7
Sr	*4A/MS*	*ppm*	0.05	20.02	9.65	50.31	10.62	10.71
Ta	*4A/MS*	*ppm*	0.01	0.86	1.3	1.21	0.99	1.06
Tb	*4A/MS*	*ppm*	0.01	1.42	1.67	1.55	1.94	1.39
Th	*4A/MS*	*ppm*	0.01	13.96	20.56	19.17	19.64	17.39
Tl	*4A/MS*	*ppm*	0.02	1.98	1.96	2.74	1.82	3.57
Tm	*4A/MS*	*ppm*	0.01	0.69	0.94	0.93	1.01	0.88
U	*4A/MS*	*ppm*	0.01	4.64	5.03	7.13	5.51	3.97
V	*4A/OE*	*ppm*	1	6	2	55	1	5
W	*4A/MS*	*ppm*	0.1	12.3	2.3	81.8	1.2	5.3
Y	*4A/MS*	*ppm*	0.05	43.38	56.56	55.95	62.18	50.99
Yb	*4A/MS*	*ppm*	0.01	4.89	6.72	6.31	6.86	5.64
Zn	*4A/OE*	*ppm*	1	550	37	116	313	317
Zr	*4A/MS*	*ppm*	0.1	293.7	427.5	417.4	410.7	377.9

Table A3.4: A total of 12 brecciated rocks were collected and analysed. Geochemical results of 7 brecciated rocks are reported in this table; the geochemical results of the other 5 brecciated rocks are reported in Table A3.5.

Element	Method	Units	Detection limit	Hydrothermal breccia						
				Sample 09	Sample 15	Sample 16	Sample 17	Sample 19	Sample 20	Sample 21
SiO_2	*XRF*	*wt.%*		73.34	80.54	75.39	83.80	82.99	82.60	83.10
TiO_2	*XRF*	*wt.%*		0.19	0.31	0.25	0.19	0.27	0.42	0.44
Al_2O_3	*XRF*	*wt.%*		8.03	10.04	10.01	6.92	4.89	6.79	8.16
Fe_2O_3 (t)	*XRF*	*wt.%*		14.51	2.76	8.84	5.75	9.23	6.44	3.75
MnO	*XRF*	*wt.%*		0.013	0.007	0.011	0.012	0.006	0.010	0.005
MgO	*XRF*	*wt.%*		0.01	0.10	0.03	0.01	0.02	0.10	0.14
CaO	*XRF*	*wt.%*		0.03	0.02	0.04	0.03	0.02	0.02	0.02
Na_2O	*XRF*	*wt.%*		0.09	0.07	0.08	0.09	0.04	0.07	0.10
K_2O	*XRF*	*wt.%*		2.27	2.81	3.16	2.00	1.53	2.20	2.63
P_2O_5	*XRF*	*wt.%*		0.167	0.059	0.053	0.052	0.056	0.083	0.054
Cr_2O_3	*XRF*	*wt.%*		0.015	0.007	0.006	0.004	0.015	0.007	0.013
Total				99.81	98.52	99.34	99.87	99.81	99.77	99.72
LOI				1.15	1.80	1.47	1.02	0.74	1.03	1.31
H_2O^-				0.29	0.24	0.31	0.26	0.22	0.25	0.25
Ag	*4A/MS*	*ppm*	*0.05*	0.16	0.26	0.34	0.11	0.35	0.09	0.08
As	*4A/MS*	*ppm*	*0.5*	17.2	5.4	4.2	4.3	4	3.1	2.2
Ba	*4A/MS*	*ppm*	*0.1*	485.2	326.2	372.5	318.1	634.7	598.7	587.9
Be	*4A/MS*	*ppm*	*0.05*	2.5	2.2	1.81	2.66	1.52	1.62	1.45
Bi	*4A/MS*	*ppm*	*0.01*	0.03	2.42	0.19	0.13	1.02	0.25	0.28
Ce	*4A/MS*	*ppm*	*0.01*	116.77	105.81	138.56	106.73	96.57	104.21	100.35
Co	*4A/MS*	*ppm*	*0.1*	1.3	0.7	0.9	1	1	2	2.1
Cr	*4A/OE*	*ppm*	*1*	7	19	6	5	54	31	45
Cs	*4A/MS*	*ppm*	*0.05*	3	2.86	3.5	2.97	2.97	3.38	3.71
Cu	*4A/OE*	*ppm*	*0.5*	8.7	1.8	3.7	5.5	3.7	2.3	2
Dy	*4A/MS*	*ppm*	*0.01*	14.66	8.16	8.54	7.75	2.77	6.1	5.35
Er	*4A/MS*	*ppm*	*0.01*	8.52	5.33	5.52	5.12	1.68	3.15	3.12
Eu	*4A/MS*	*ppm*	*0.01*	2.35	1.44	2.12	1.49	0.88	1.73	1.55
Ga	*4A/MS*	*ppm*	*0.05*	13.31	17.73	16.91	12.22	10.96	14.08	15.08
Gd	*4A/MS*	*ppm*	*0.01*	12.85	7.3	9.14	6.84	3.24	7.94	6.36
Ge	*4A/MS*	*ppm*	*0.05*	0.57	1.41	0.75	0.74	1.07	1.46	1.24
Hf	*4A/MS*	*ppm*	*0.05*	7.66	8.64	9.46	7.21	3.86	4.64	4.58
Ho	*4A/MS*	*ppm*	*0.01*	2.88	1.69	1.76	1.6	0.56	1.15	1.03
In	*4A/MS*	*ppm*	*0.01*	0.07	0.37	0.06	0.07	0.1	0.1	0.06
La	*4A/MS*	*ppm*	*0.01*	59.53	60.27	74.11	55.58	54.71	54.26	51.86
Li	*4A/MS*	*ppm*	*0.1*	1.2	3.8	2.3	2.8	2.1	1.7	1.2
Lu	*4A/MS*	*ppm*	*0.01*	1.01	0.73	0.75	0.7	0.23	0.36	0.43
Mo	*4A/MS*	*ppm*	*0.1*	1.5	0.8	0.5	6.3	0.5	0.3	0.1
Nb	*4A/MS*	*ppm*	*0.05*	13.64	17.18	17.29	13.37	6.15	10.2	10.16
Nd	*4A/MS*	*ppm*	*0.01*	53.47	37.84	57.93	42.77	31.63	46.29	41.75
Ni	*4A/OE*	*ppm*	*0.5*	8	4.2	1.5	2.8	5.5	6.5	8.1
Pb	*4A/MS*	*ppm*	*0.5*	71.1	189.9	16.9	12.3	54.5	20.5	21.2
Pr	*4A/MS*	*ppm*	*0.01*	13.54	10.8	16.02	11.79	9.83	12.37	11.47

Rb	*4A/MS*	*ppm*	*0.05*	162.51	189.76	189.06	117.37	119.11	170.34	205.65
Sb	*4A/MS*	*ppm*	*0.05*	44.47	2.73	6.19	11.35	62.8	5.87	3.62
Sc	*4A/MS*	*ppm*	*0.1*	4.3	5.8	5.1	4.1	4.2	8	9.9
Se	*4A/MS*	*ppm*	*0.5*	1.3	1.1	1.1	0.9	X	0.9	0.8
Sm	*4A/MS*	*ppm*	*0.01*	12.2	7.8	11.54	8.57	4.8	9.27	8.03
Sn	*4A/MS*	*ppm*	*0.1*	2.6	4.7	3	2.5	4.4	2	3.6
Sr	*4A/MS*	*ppm*	*0.05*	38.94	9.37	9.11	13.51	19.73	34.48	20.04
Ta	*4A/MS*	*ppm*	*0.01*	0.9	1.02	1	0.88	0.42	0.6	0.68
Tb	*4A/MS*	*ppm*	*0.01*	2.2	1.31	1.47	1.2	0.5	1.12	0.91
Th	*4A/MS*	*ppm*	*0.01*	16.51	20.55	22.23	15.18	8.02	8.76	10.14
Tl	*4A/MS*	*ppm*	*0.02*	1.82	1.9	1.78	1.28	1.17	1.53	1.82
Tm	*4A/MS*	*ppm*	*0.01*	1.18	0.75	0.8	0.71	0.24	0.44	0.44
U	*4A/MS*	*ppm*	*0.01*	4.78	5.09	4.88	4.36	2.64	2.56	2.87
V	*4A/OE*	*ppm*	*1*	24	17	6	2	23	20	30
W	*4A/MS*	*ppm*	*0.1*	52.5	6.7	23.8	7.1	14.9	27.3	4.6
Y	*4A/MS*	*ppm*	*0.05*	82.58	45.03	47.85	42.42	14.41	26.97	25.18
Yb	*4A/MS*	*ppm*	*0.01*	7.17	4.75	4.93	4.62	1.53	2.57	2.8
Zn	*4A/OE*	*ppm*	*1*	37	30	26	20	27	28	32
Zr	*4A/MS*	*ppm*	*0.1*	299.6	332.2	370	278.9	148.9	175.7	168.3

Table A3.5: Geochemical results of the remaining 5 brecciated rocks and 1 rock sample of the vein. The vein has a very high Fe_2O_3 content of 87.40%, indicating that these veins are Fe-rich.

Element	Method	Units	Detection limit	Hydrothermal breccia					Vein
				Sample 24	Sample 30	Sample 45	Sample 46	Sample 121	Sample 08
SiO_2	*XRF*	*wt.%*		74.22	78.98	78.52	71.05	85.78	6.58
TiO_2	*XRF*	*wt.%*		0.36	0.31	0.42	0.26	0.18	0.01
Al_2O_3	*XRF*	*wt.%*		10.89	9.76	7.42	11.11	6.34	3.78
Fe_2O_3 (t)	*XRF*	*wt.%*		8.90	4.72	9.66	12.22	4.63	87.40
MnO	*XRF*	*wt.%*		0.020	0.765	0.011	0.074	0.094	0.015
MgO	*XRF*	*wt.%*		0.11	0.06	0.12	0.09	0.03	0.05
CaO	*XRF*	*wt.%*		0.03	0.11	0.02	0.03	0.02	0.16
Na_2O	*XRF*	*wt.%*		0.16	0.07	0.07	0.15	0.01	0.01
K_2O	*XRF*	*wt.%*		3.28	2.88	2.44	3.19	2.00	1.06
P_2O_5	*XRF*	*wt.%*		0.142	0.079	0.055	0.097	0.048	0.360
Cr_2O_3	*XRF*	*wt.%*		0.007	0.008	0.008	0.005	0.009	0.013
Total				99.86	99.802	99.73	99.99	99.97	100.06
LOI				1.74	2.06	0.99	1.71	0.84	0.64
H_2O^-				0.4	0.41	0.29	0.34	0.26	0.24
Ag	*4A/MS*	*ppm*	*0.05*	0.31	0.28	0.09	0.09	0.17	0.12
As	*4A/MS*	*ppm*	*0.5*	8.5	3.5	3.6	13.1	3.8	41.3
Ba	*4A/MS*	*ppm*	*0.1*	1008.5	174.2	430.4	684.1	323	396.3
Be	*4A/MS*	*ppm*	*0.05*	3.2	2.28	1.55	2.62	1.59	6.93
Bi	*4A/MS*	*ppm*	*0.01*	0.19	0.35	0.29	0.03	0.22	0.05
Ce	*4A/MS*	*ppm*	*0.01*	145	103.1	74.9	153.2	91.36	16.36
Co	*4A/MS*	*ppm*	*0.1*	2.9	3.5	2.4	4.3	1.1	1.7
Cr	*4A/OE*	*ppm*	*1*	5	3	24	8	9	5
Cs	*4A/MS*	*ppm*	*0.05*	8.53	4.81	3.51	4.21	1.72	2.33
Cu	*4A/OE*	*ppm*	*0.5*	5.6	6.5	2.2	8.5	9.1	8.8
Dy	*4A/MS*	*ppm*	*0.01*	10.55	7.96	5.69	9.76	6.93	2.24
Er	*4A/MS*	*ppm*	*0.01*	6.2	5.03	3.38	6.03	4.47	1
Eu	*4A/MS*	*ppm*	*0.01*	3.21	1.75	1.25	2.29	1.38	0.74
Ga	*4A/MS*	*ppm*	*0.05*	20.38	16.43	14.74	21.3	12.29	7.68
Gd	*4A/MS*	*ppm*	*0.01*	11.38	7.3	5.8	11.28	6.56	3.53
Ge	*4A/MS*	*ppm*	*0.05*	1.15	1.08	1.29	0.79	0.84	X
Hf	*4A/MS*	*ppm*	*0.05*	9.45	8.39	5.75	11.03	6.8	0.15
Ho	*4A/MS*	*ppm*	*0.01*	2	1.63	1.11	1.91	1.42	0.38
In	*4A/MS*	*ppm*	*0.01*	0.08	0.25	0.1	0.12	0.13	0.05
La	*4A/MS*	*ppm*	*0.01*	77.92	54.97	37.59	84.44	51.49	7.53
Li	*4A/MS*	*ppm*	*0.1*	2.4	5	1.9	2.3	4.4	1.8
Lu	*4A/MS*	*ppm*	*0.01*	0.89	0.74	0.46	0.93	0.64	0.08
Mo	*4A/MS*	*ppm*	*0.1*	0.4	1	0.3	0.3	0.4	1
Nb	*4A/MS*	*ppm*	*0.05*	15.6	12.31	9.75	17.49	10.99	2.99
Nd	*4A/MS*	*ppm*	*0.01*	63.06	43.63	32.04	64.38	39.01	9.8
Ni	*4A/OE*	*ppm*	*0.5*	4.9	3.1	5.2	7	1.6	3.5
Pb	*4A/MS*	*ppm*	*0.5*	172.3	229.2	20.8	39.4	30.9	113.6
Pr	*4A/MS*	*ppm*	*0.01*	16.66	11.66	8.7	17.47	10.63	2.25
Rb	*4A/MS*	*ppm*	*0.05*	318.63	219.3	181.47	242.68	180.93	85.44

Sb	*4A/MS*	*ppm*	*0.05*	27.19	2.94	6.26	33.4	2.52	112.88
Sc	*4A/MS*	*ppm*	*0.1*	11.1	6.5	9.1	5	3	0.9
Se	*4A/MS*	*ppm*	*0.5*	1.3	1	0.7	1.3	0.5	X
Sm	*4A/MS*	*ppm*	*0.01*	11.8	8.23	6.21	12.02	7.16	3.31
Sn	*4A/MS*	*ppm*	*0.1*	3	2.4	2.3	3.6	2.1	1.9
Sr	*4A/MS*	*ppm*	*0.05*	28.4	4.67	9.9	27.07	7.12	79.94
Ta	*4A/MS*	*ppm*	*0.01*	1.17	0.88	0.69	1.29	0.79	0.04
Tb	*4A/MS*	*ppm*	*0.01*	1.74	1.22	0.91	1.68	1.05	0.52
Th	*4A/MS*	*ppm*	*0.01*	17.04	15.53	9.29	20.85	13.61	2.18
Tl	*4A/MS*	*ppm*	*0.02*	3.89	2.02	1.63	2.34	1.53	0.92
Tm	*4A/MS*	*ppm*	*0.01*	0.88	0.77	0.46	0.87	0.66	0.12
U	*4A/MS*	*ppm*	*0.01*	4.33	4.06	2.74	4.61	4.05	3.1
V	*4A/OE*	*ppm*	*1*	7	5	22	4	3	18
W	*4A/MS*	*ppm*	*0.1*	52.5	1.3	26.4	16.9	9.4	286.3
Y	*4A/MS*	*ppm*	*0.05*	51.92	41.47	28.66	49.47	37.02	12.37
Yb	*4A/MS*	*ppm*	*0.01*	6.71	5.09	3.2	6.03	4.38	0.62
Zn	*4A/OE*	*ppm*	*1*	191	185	29	136	30	59
Zr	*4A/MS*	*ppm*	*0.1*	366.9	328.8	214	423.8	253.2	5.2